CONSTRUCTING REFERENCE DATASETS FOR EVALUATING AUTOMATED COMPENSATION ALGORITHMS IN MULTICOLOR FLOW CYTOMETRY

A Thesis Submitted to
the Graduate School of Engineering and Sciences of
İzmir Institute of Technology
in Partial Fulfillment of the Requirements for the Degree of

MASTER OF SCIENCE

in Electronics and Communication Engineering

by
Nurhan ARSLAN

November 2017
İZMİR

We approve the thesis of **Nurhan ARSLAN**

Examining Committee Members:

Prof. Dr. Bilge KARAÇALI
Department of Electrical and Electronics Engineering
İzmir Institute of Technology

Prof. Dr. Mehmet Salih DİNLEYİCİ
Department of Electrical and Electronics Engineering
İzmir Institute of Technology

Assoc. Prof. Devrim ÜNAY
Department of Biomedical Engineering
İzmir University of Economics

21 November 2017

Prof. Dr. Bilge KARAÇALI
Supervisor, Department of Electrical and Electronics Engineering
İzmir Institute of Technology

Prof. Dr. Enver TATLICIOĞLU
Head of the Department of
Electrical and Electronics Engineering

Prof. Dr. Aysun SOFUOĞLU
Dean of the Graduate School of
Engineering and Sciences

ACKNOWLEDGMENTS

I would like to say my deepest thanks to my supervisor Prof. Dr. Bilge Karaçalı for his support, guidance, encouragement and trust during my master study. He was always helpful and produced proper analytical solutions whenever I had a question about my research and also every question. He remains my best role model for a scientist, researcher, and mentor.

Many thanks for members of technical and scientific support of the Beckton Dickinson Company. I know that without them, I could not succeed to collect the technical data. I offer my most sincere thanks to Stijn Duytschaever, Stephane Bellet in the technical support of BD. I also thank Hakan Palabıyık, Mr. / Mrs. Ariane Aduriz Berasategi, Pieter Jan Meuwissen, Paola Bruno and Elio Schouppe in scientific support team of Beckton Dickinson Company.

I would like to say my sincere thanks to Dick Stewart for filter specifications from the Chroma Technology Corporation. Many thanks to Christian Dille and Norbert Klose for photomultiplier specifications and answers to scientific questions from Hamamatsu Photonics Company.

I would like to thank Prof. Dr. Salih Dinleyici for his contributions and interest in this thesis.

I will forever be thankful to Assistant Prof. Dr. Serap Şahin with my all heart. She has been helpful in providing advice many times throughout the entire process. She has always positive outlook and smiles despite the situations. She always gave her most precious advice to me as for making your research and study with love and full of concentration.

I would like to thank Assistant Prof. Dr. Selma Tekir for her support and kindness. I would also thanks for her delicious elegant coffee and wafers.

I would also like to thank my lab friends Başak Esin Köktürk Güzel, Tufan Bakırcıgil, Bilal Orkan Olcay and Serhat Çağdaş for their support and precious friendship.

I would also like to thank Çağın Ekici, Gizem Soylu, Göksenin Bozdağ, Oktay Karakuş and all of my friends for their friendship and all valuable sharing from Electrical and Electronics Engineering Department with whom I shared my working life during three years.

I would also like to share my deepest thanks with Burçin Papatya Kaya, Ceren Pişkinsüt, Naciye Yücel, Ufuk Yücel and Basri Mumcu. They have always been my most

valued friends.

I also must express my profound gratitude to my mother, my father, my brother and my grandfather for their unfailing support and endless encouragement during my whole life. Finally, I would like thank to my pet Lady for her unconditional love, limitless energy and happy smiles on my face.

ABSTRACT

CONSTRUCTING REFERENCE DATASETS FOR EVALUATING AUTOMATED COMPENSATION ALGORITHMS IN MULTICOLOR FLOW CYTOMETRY

In this thesis, we develop a numerical framework to simulate flow cytometry readings on BD FACSCanto flow cytometer by constructing cell profiles with specific target biomarker concentrations and modelling various physical phenomena involved in a flow cytometer. The principal aim of this thesis is to provide realistic datasets over which prospective automated compensation algorithms can be evaluated. In our study, we have first constructed model cell profiles based on human lymphocytes stained with fluorescent dyes. We secondly focused on determining the number of photons emitted from each fluorochrome-conjugated target proteins in a cell through fluorescence following excitation. We thirdly simulated the optic channel of BD FACSCanto flow cytometer and implemented a stochastic photon counting method to determine fluorescence intensity received in the different detectors. Then, we simulated a pre-amplifier circuit to calculate the detector responses as voltage pulses from each cell in response to received photons. Using the completed platform, we have generated a two-colour flow cytometry dataset including + +, + -, - +, and - - cell groups using FITC and PE fluorochromes. We demonstrated the usefulness of the generated reference datasets by applying two different linear compensation methods and comparing the resulting compensated datasets in both linear and logarithmic scales. These results suggest that the developed platform can be used to generate realistic multi-colour flow cytometry datasets that can be used to validate compensation algorithms.

ÖZET

ÇOKRENKLİ AKIŞ SİTOMETRİSİNDE OTOMATİK DENGELEME ALGORİTMALARININ DEĞERLENDİRİLMESİ İÇİN REFERANS VERİ KÜMELERİNİN OLUŞTRULMASI

Bu çalışmada, BD FACSCanto akış sitometrisinde okunan değerlerin simülasyonunu yapmak için, belli hedef biyoişaret konsantrasyonuna sahip hücre profilleri oluşturularak ve bir akış sitometrisinde yer alan fiziksel olaylar modellenerek, nümerik bir platform oluşturduk. Çalışmanın asıl amacı; prospektif otomatikleştirilmiş dengeleme algoritmalarının değerlendirilebileceği gerçekçi veri setlerinin sağlanabilmesidir. Çalışmamızda, ilk olarak flüoresan boyalarla boyanmış insan lenfositlerine dayanan, model hücre profillerini oluşturduk. İkinci olarak, bir hücredeki hedef proteinlerine bağlanmış her bir fluorokromun, uyarımından sonra fluoresans süresince yayılan foton sayısını belirlemeye odaklandık. Üçüncü olarak, BD FACSCanto akış sitometrisinin optik kanalının simülasyonunu yaptık ve farklı dedektörlere ulaşan ışınım yoğunluğunu belirlemek için bir stokastik foton sayma yöntemi uyguladık. Daha sonra, ulaşan fotonlara karşılık olarak, her bir hücrenin dedektör tepkilerini, voltaj sinyalleri olarak hesaplamak için bir ön amplifikatör devresini simüle ettik. Bu tamamlanmış platformu kullanarak, FITC ve PE fluorokromlarını kullanarak, + +, + -, - +, - - hücre gruplarını içeren, iki renkli akış sitometrisi veri setlerini oluşturduk. Üretilen veri setlerinin kullanılabilirliğini göstermek için iki farklı doğrusal dengeleme metodu uyguladık ve kompanse edilen veri setlerinin sonuçlarını hem doğrusal hem de logaritmik ölçekte karşılaştırdık. Elde edilen sonuçlar, geliştirilen platformu, dengeleme algoritmalarının doğrulanmasında kullanılmak üzere, gerçekçi çok-renkli akış sitometri veri setleri üretimi için önermektedir.

TABLE OF CONTENTS

LIST OF FIGURES x

LIST OF TABLES xiii

LIST OF SYMBOLS xiv

LIST OF ABBREVIATIONS xv

CHAPTER 1. INTRODUCTION 1

CHAPTER 2. BACKGROUND ON FLOW CYTOMETRY TECHNOLOGY 4

- 2.1. A History on Flow Cytometers 4
  - 2.1.1. Biomarker Staining Using Monoclonal Antibodies 9
- 2.2. Flow Cytometer Subsystems 11
  - 2.2.1. Fluidics 11
    - 2.2.1.1. Laminar Flow 13
    - 2.2.1.2. Flow Chamber 14
  - 2.2.2. Optical System 15
    - 2.2.2.1. Excitation Optics 15
    - 2.2.2.2. Collection Optics 17
  - 2.2.3. Electronics 21
- 2.3. Flow Cytometry Data Analysis 22
  - 2.3.1. Gating on Scatter Plots 23
  - 2.3.2. Light Scatter 23
    - 2.3.2.1. Forward Scattering 25
    - 2.3.2.2. Side Scattering 26
- 2.4. Fluorescence 26
- 2.5. Fluorescence Spillover 28
- 2.6. Compensation 29

CHAPTER 3. METHODS 31

- 3.1. BD FACSCanto Flow Cytometer 31

3.2. Modelling of BD FACSCanto Flow Cytometer 31
3.2.1. Excitation Optics and Laser Specifications 31
3.2.2. Optic Channel Specifications 33
3.3. Modelling Cells 34
3.4. Modelling Fluorescence Emission 36
3.4.1. Excitation Duration and Illuminated Volume 37
3.4.2. Energy Absorbance for a Single Fluorophore 39
3.4.3. Energy Absorbance for Multiple Fluorophores 42
3.4.4. Emission 43
3.4.5. Modelling The Optical Channel 43
3.5. Photon Distributions across Detectors 49
3.5.1. Photomultiplier Tube's Response at the Detectors 50
3.6. Pre-amplifier Circuit 52

CHAPTER 4. RESULTS 55
4.1. Construction of Model Cells Profiles 55
4.2. Results for a Single Cell with FITC-Conjugated Proteins 57
4.3. Results for a Single Cell with PE-Conjugated Proteins 67
4.3.1. Results for a Single Cell with Two Fluorochromes 71
4.4. Results for a Group of Cells 76
4.5. Compensation 79
4.5.1. Formulaic Linear Compensation 80
4.5.2. Manual Linear Compensation 84
4.5.3. Effects of Latent Fluorochrome Fraction 89

CHAPTER 5. DISCUSSION 92

CHAPTER 6. CONCLUSION 96

REFERENCES 97

APPENDICES

APPENDIX A. SPECIFICATIONS OF FILTERS IN THE OPTICAL CHANNEL . 101

APPENDIX B. SPECIFICATIONS OF PHOTOMULTIPLIER TUBES IN THE OPTICAL CHANNEL 106

LIST OF FIGURES

Figure **Page**

Figure 2.1. Schematic of the first working flow cytometer 5
Figure 2.2. The First Coulter Counter 6
Figure 2.3. Kamentsky's flow cytometer 7
Figure 2.4. Process of Monoclonal Antibody Production 10
Figure 2.5. Fluid flow in a flow cytometer 12
Figure 2.6. Turbulence affect according to shapes of sheath and core inlets at the flow chambers (Adapted From: (Shapiro, 2005)) 14
Figure 2.7. Schematic of a laser 16
Figure 2.8. Bandpass Filter 18
Figure 2.9. Longpass Filter 18
Figure 2.10. Schematic of a photomultiplier tube 20
Figure 2.11. Anatomy of a pulse 22
Figure 2.12. Gate Types 24
Figure 2.13. Forward scatter (FSC) and side scatter (SSC) 25
Figure 2.14. A Jablonski diagram 27
Figure 2.15. Emission spectra of different fluorochromes excited 488 nm laser with their corresponding bandpass filters 29
Figure 3.1. Light pathway in the BD FACSCanto flow cytometer 32
Figure 3.2. Octagon Detector Array 33
Figure 3.3. Size distribution of the cells with 0.95 confidence interval 35
Figure 3.4. Illustration of the illuminated region under the laser beam 37
Figure 3.5. Illuminated volume of cell according to cell position un 38
Figure 3.6. Schematic of full width at half maximum value 39
Figure 3.7. Laser illumination in the cross-section of the cell 41
Figure 3.8. Summary of energy absorbance equations for cells that are positive for only FITC, only PE and FITC and PE conjugated cells 44
Figure 3.9. Schematic overview of the octagon detector array 47
Figure 3.10. Probability interval of each detector at the octagon detector array 50
Figure 3.11. R928,R955 Photomultiplier Tube 51
Figure 3.12. Preamplifier Circuit 53
Figure 3.13. Pulse Measurement 54
Figure 4.1. Radii histogram for 1000 model cells 56

Figure 4.2. Histogram of FITC-conjugated protein numbers for 1000 model cells . 56
Figure 4.3. Histogram of PE-conjugated protein numbers for 1000 model cells 57
Figure 4.4. Laser path length entering the cell at point (x, y) in the cross section ... 58
Figure 4.5. Absorbed energy at point (x, y) from FITC- conjugated protein in the cell cross section 58
Figure 4.6. Emission Spectrum of FITC 59
Figure 4.7. Cumulative Distribution Function of FITC 59
Figure 4.8. Wavelength histogram of the emitted photons from a FITC-conjugated cell for 2643 photons 60
Figure 4.9. Probability curves of each detector at the octagon detector array 61
Figure 4.10. Wavelength histogram of the emitted photons by the FITC positive cell at different detectors and lost photons 62
Figure 4.11. The illuminated volume of the cell under the laser illumination 63
Figure 4.12. Time that the laser illuminates the cell 64
Figure 4.13. Surface graph of the reference voltage matrix 66
Figure 4.14. Detector responses obtained via bilinear interpolation 66
Figure 4.15. Absorbed energy at point (x, y) from PE-conjugated protein in the cell cross section 68
Figure 4.16. Emission Spectrum of PE 68
Figure 4.17. Cumulative Distribution Function of PE 69
Figure 4.18. Wavelength histogram of the emitted photons from a PE-conjugated cell for 38049 photons 69
Figure 4.19. Wavelength histogram of the emitted photons by the PE positive cell at different detectors and lost photons 70
Figure 4.20. Detector responses 72
Figure 4.21. Absorbed energy at a point (x, y) by FITC-conjugated protein in the cell cross section 73
Figure 4.22. Absorbed energy at a point (x, y) by PE-conjugated protein in the cell cross section 74
Figure 4.23. Wavelength histogram of the total emitted photons for a cell that is positive for FITC-conjugated target protein and also positive for a PE-conjugated target protein 75
Figure 4.24. Wavelength histogram of the emitted photons by the FITC and PE positive cell at different detectors and lost photons 76
Figure 4.25. Detector responses 77

Figure 4.26. The number of target proteins for + +, + -, + - and - - cell groups 78
Figure 4.27. The results of the detector responses for each of 4000 cells containing + +, + -, + - and - - cell groups in the linear scale 79
Figure 4.28. The results of the detector responses for 4000 cells in the log-scale 80
Figure 4.29. Diagram of two-signal spillover system 81
Figure 4.30. The results of the detector responses for each of 4000 cells after formulaic linear compensation in the linear scale 83
Figure 4.31. The results of the detector responses for each of 4000 cells after formulaic linear compensation in log-scale 83
Figure 4.32. The spillover coefficient A matching the medians of the corresponding cell groups for manual linear compensation 85
Figure 4.33. The spillover coefficient B matching the medians of the corresponding cell groups for manual linear compensation 85
Figure 4.34. The results of the detector responses for each of 4000 cells after manual linear compensation matching the means matching the medians in the linear scale 86
Figure 4.35. The results of the detector responses for each of 4000 cells after manual linear compensation matching the medians in log scale 87
Figure 4.36. The spillover coefficient A matching the means of the corresponding cell groups for manual linear compensation 88
Figure 4.37. The spillover coefficient B matching the means of the corresponding cell groups for manual linear compensation 88
Figure 4.38. The results of the detector responses for each of 4000 cells after manual linear compensation matching the means in linear scale 89
Figure 4.39. The results of the detector responses for each of 4000 cells after manual linear compensation matching the means in log scale 90
Figure 4.40. The results of compensation in linear and log scale for fluorochrome fraction equalling to 0.1 of FITC fluorescence emission 90
Figure 4.41. The results of compensation in linear and log scale for fluorochrome fraction equalling to 0.01 of FITC fluorescence emission 91
Figure 4.42. The results of compensation in linear and log scale for fluorochrome fraction equalling to 0.001 of FITC fluorescence emission 91

LIST OF TABLES

Table **Page**

Table 3.1. Filters and Dyes in the Octagon Detector Array 45
Table 4.1. FITC-conjugated cell 57
Table 4.2. Detector responses in terms of voltage height 64
Table 4.3. Reference voltage matrix in a table form 65
Table 4.4. PE-conjugated cell 67
Table 4.5. Detector responses in terms of voltage height 71
Table 4.6. FITC and PE conjugated cell 72
Table 4.7. Detector responses in terms of voltage height 77

LIST OF SYMBOLS

h	Planck's constant
R_e	Reynolds number
D	tube diameter
c	light velocity
V	mean velocity
ρ	density of fluid
η	dynamic viscosity of liquid
N_A	Avogadro number
q_e	quantum efficiency for PMT

LIST OF ABBREVIATIONS

FITC	Fluorescein Isothiocyanate
PE	Phycoerythrin
PDF	probability density function
CDF	cumulative distribution function
LP	longpass filter
BP	bandpass filter
FSC	forward scattering
SSC	side scattering
ADC	analog to digital converter
FWHM	full width at half maximum
PMT	photomultiplier tube
FACS	Fluorescence-Activated Cell Sorter
FCS	Flow Cytometry Standard
ISAC	International Society for Advancement of Cytometry

CHAPTER 1

INTRODUCTION

Flow cytometry is the most powerful and advanced technique that simultaneously measures and analyses multiple physical, chemical and biological properties of single cells or particles in heterogeneous cell systems. Flow technology has very rapid and extensive measurement and identification capacity in single cell level. Single cell measurements evaluate the intrinsic and extrinsic structure of individual cells, such as DNA and RNA amounts, internal complexity, size, membrane potential, granularity, enzyme activity and many others (Tuchin, 2011). All of these details about cell functionality helps shed light on many problems in life sciences. For instance, quantitative analysis of single cells plays a big role in disease diagnosis in many clinical types of research. Flow cytometry is especially used in medicine and biomedical research areas such as immunology, oncology, haematology, drug discovery, protein engineering, vaccine analysis and so on. In immunology, flow cytometry is generally used to perform measurements on the immune system to provide insight on the complexity of the system (Chattopadhyay et al., 2014).

Flow cytometry has three main subsystems, which are fluidics, optics and electronics systems. The three subsystems work together to simultaneously measure multiple physical characteristics of single cells as they pass through a laser beam in a fluid stream. Firstly, cells are stained with fluorescent dyes to evaluate target functionality in sample preparation process. Then the cell sample is put in the flow cytometer. The fluidics subsystem transports the cells in a stream to an interrogation point at which the laser beam intersects with stained cells. The optics subsystem incorporates excitation light sources and collection optics components to gathering light signals and then routing them to the appropriate detectors. The electronics subsystem converts firstly the light signal into an electrical signal, and then the electrical signal into digital data for further analysis in a computer.

In a multicolor flow cytometry experiment, multiple fluorescent dyes are used for detecting each cell subgroup of interest. The tail of a fluorescent dye's emission spectrum typically interferes optically with other emission spectra of fluorescent dyes in unwanted detectors. This means that the detectors have spectral overlaps which do not belong up to responsible fluorescent dye and this is unavoidable in the case of two or more fluorescent dyes in the multicolor flow cytometry experiment. As a result, spectral overlap causes unwanted correlations in the detected signals that adversely affect determining subpopulations and interpreting the data. Compensation is the process by which spillover between detectors is mathematically corrected (Roederer, 2001). However, compensation is a major challenge as it is expert and physician driven, nearly impossible for multicolor flow experiments, and after the compensation process, the data is non-reproducible.

In 1977, Loken, David Parks, et al. proposed discrimination of the spectral overlaps between fluorescein and rhodamine signals (Loken et al., 1977). They designed a compensation circuit using differential amplifiers, potentiometers, and cross-coupling connections to subtract unwanted contributions from rhodamine and fluorescein signals in real time. The system worked well for two and three colors. However, with more than three colours it was not possible to separate signals optically (Loken et al., 1977). C. Bruce Bagwell and Earl G. Adams proposed a theory for two signals compensation, then a generalized theory for multiple signals (Bagwell and Adams, 1993). They carried at hardware compensation and software compensation and discussed their results (Bagwell and Adams, 1993). Mario Roederer and his research group addressed spectral compensation using linear algebra as they rendered the data orthogonal for further analysis (Roederer, 2001). They constructed a mathematical model that involved photon intensities in measurement channels, spillover measurement error amounts as well as the characteristics of data storage. However, they found linear and nonlinear errors that were caused by photon counting statistics and log-scale binning errors. These errors were unavoidable and led to incorrect conclusions (Roederer, 2001). A growing body of literature on flow cytometry data analysis exists on manual compensation and automated gating. But, the manual compensation methods are insufficient for more than two fluorochromes in a flow cytometry experiment for accurate, exact analysis of the multicolor flow cytometry data. This extensively needs a standardization of the flow cytometry data prior to further the proper compensation. In addition, the true and proper compensation is critical for gating step to ensure again the accurate interpretation of the flow data such as identification of subgroups of cells in a heterogeneous cell population.

In this study, we develop a numerical platform that simulates flow cytometer readings from cells with specific target biomarker concentration, in an effort to provide ground-truth datasets for evaluating automated compensation algorithms. To this end, we used a stochastic model of the photon counting process and constructed a method to generate realistic multicolor flow cytometry datasets by modelling the fluorescence and detector physics in a flow cytometer. The configuration of the flow cytometer was based on BD FACSCanto (BD FACSCanto, 2006). This numeric model comprises a model of the excitation optics subsystem to find the number emitted photons from a cell with specific parameters, a separate model of the collection optics subsystem and a third model for the detector characteristics to calculate fluorescence amounts in each measurement channel.

This thesis is organized in four chapters with the Introduction in Chapter 1. Chapter 2 presents background on flow cytometers with a literature review, elaborating on how flow cytometry works, including the basics of flow cytometry data analysis and fluorescence spillover. Chapter 3 describes the technical background of BD FACSCanto Flow Cytometer and details the model of the cytometer, cells, fluorescence emission, and the optic channel. Chapter 4 shows the results for a single cell with one fluorochrome first, then with two fluorochromes, and finally results for a group of cells including positive-positive, positive-negative, negative-positive and negative-negative cell groups, along with scatter plots of detector responses before and after manual compensation. Chapter 5 consists of the discussion with a brief summary of the work and comments on how the platform can be used to evaluate prospective automated compensation algorithms.

CHAPTER 2

BACKGROUND ON FLOW CYTOMETRY TECHNOLOGY

Flow cytometry is composed of ‘flow’, ‘cyto’ and ‘metry’. ‘Flow’ implies fluid, ‘cyto’ means cell and ‘metry’ is measurement, and cytometry is a general term that means analysis of cells in a quantitative manner. Flow cytometry is a process that is performed on cells in liquid suspension. It is a most powerful technique to measure and distinguish simultaneously physical, biological and chemical properties of individual cells in a heterogeneous cell population. It is an application of multicolor technology and based on optical improvements, new fluorochromes developments and individual cell analysis technology and alternative to microscopic counts and other developments in medicine and biology (Tuchin, 2011). Flow cytometry allows analysing cell-by-cell a multitude of parameters very rapidly in mixed cell populations. One of the benefits of flow cytometry is that biological systems have very high complexity, and flow cytometry characterizes single cells according to their multiple structural properties in cell systems. Thus, flow cytometry can help understand the underlying cause of complexity of cell systems. Multicolor flow cytometry allows evaluating cell subgroups, complexities underlying cell structures and cell to cell interactions in heterogeneous cell systems. Functional properties of heterogeneous cell systems can be determined and identified by flow cytometers. Physicians and experts use this functionality of flow cytometers, and they can identify how diseases cause biological alterations in a cell system. Flow cytometry is used in many areas such as diagnosing cancer, immune system diseases, infections and so on.

2.1. A History on Flow Cytometers

Evolution of flow cytometers involves and follows many other technological developments. We explain improvements of the flow cytometer in a chronological order and also point to the other important technological developments related to flow cytometer subsystems. The earliest flow cytometer description appeared in 1934 and this description is generally accepted as the birth of flow cytometer (Moldavan, 1934). It introduced the concept of counting microscopic cells in a suspension. The experiment design contained a small photoelectric apparatus that was adjusted to the microscope ocular and it was sensitive to the microscopic scale. When a cell passed through the capillary glass tube, the photoelectric apparatus registered it automatically. The author then conceptualized that it caused a very small current, and described the amplification of the current and keeping it in record. The photoelectric apparatus was suggested to be highly sensitive as a photoelectric sensor to make extinction measurements. However, the author had never succeeded getting the device to work during the time of publication.

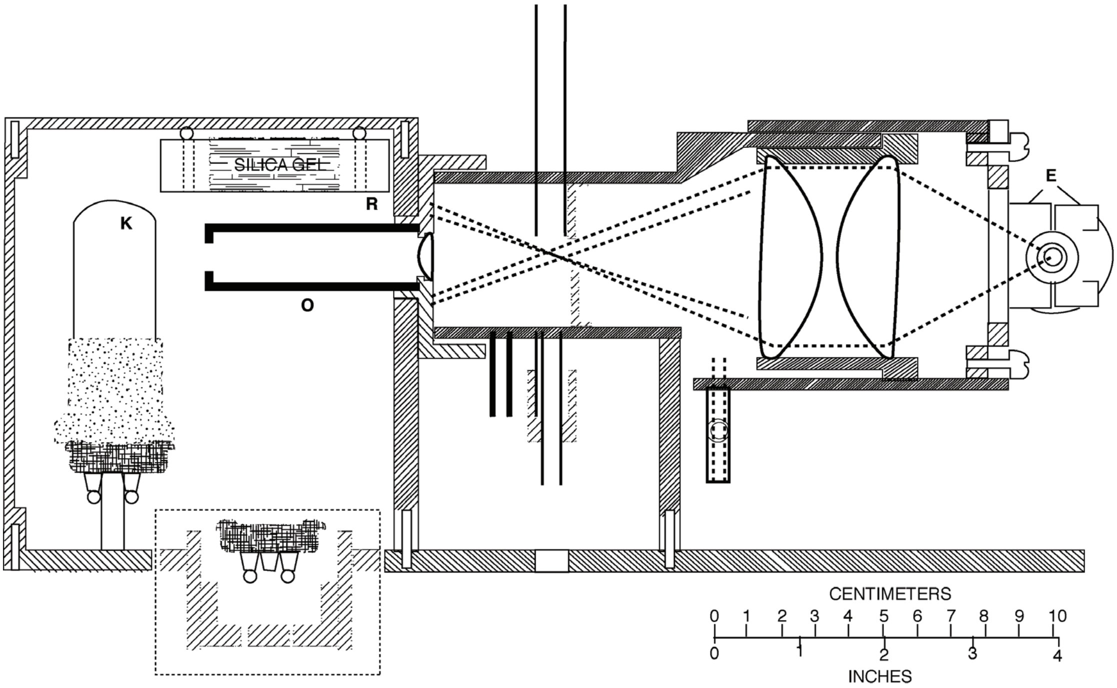

Figure 2.1. Schematic of the first working flow cytometer

Adapted From: (Gucker Jr et al., 1947)

The first working flow cytometer was designed in 1947 while making measurements of penetrating aerosol amounts in gas mask filters used in the Second World War (Gucker Jr et al., 1947), illustrated in Fig.2.1. A research group endeavoured to develop the first working flow cytometer with three different trials. Firstly, they designed an electronic photometer as a smoke penetrometer with the purpose of comparing the aerosols concentration to a limit value. They made a type of smoke test to measure penetration in the order of particles per minute, and if the measurement was beyond the limit value, they observed scattered light causing pulses. They then developed the instrument as it was counting particles individually and tested the gas mask filters rapidly and quantitatively in 1944. The group later developed a photoelectronic apparatus whose electrical background allowed counting an article down to 0.6 μm diameter per minute in 1945. Interestingly, they used a Ford automobile headlight bulb as a light source because it was the most powerful light source they could find at the time. The flow system was designed so that each cell passed through the light beam individually. A photomultiplier tube was used as a light detector at the apparatus, which was also a new technology at the time, seen at the left of Fig.2.1. Each particle was exposed to illumination for 3 msec. The scattered light then fell on the photosensitive cell labeled with K in Fig.2.1, producing an electrical pulse. The photosensitive cell used in the device was a thalofide cell, which was regarded as a new photo-electric cell with maximum sensitivity to light (Case, 1920). The observation point was the intersection of the cones at the center of Fig.2.1. The apparatus could detect a particle 0.6 μm in diameter with a probability of 0.6. The development was beyond just a very sensitive smoke penetrometer; today, it is regarded as the first photo-electric counter (Schmid, 2012). On the other hand, the first flow cytometer was rather primitive, because the electro-optical technology was not very well developed until 1950.

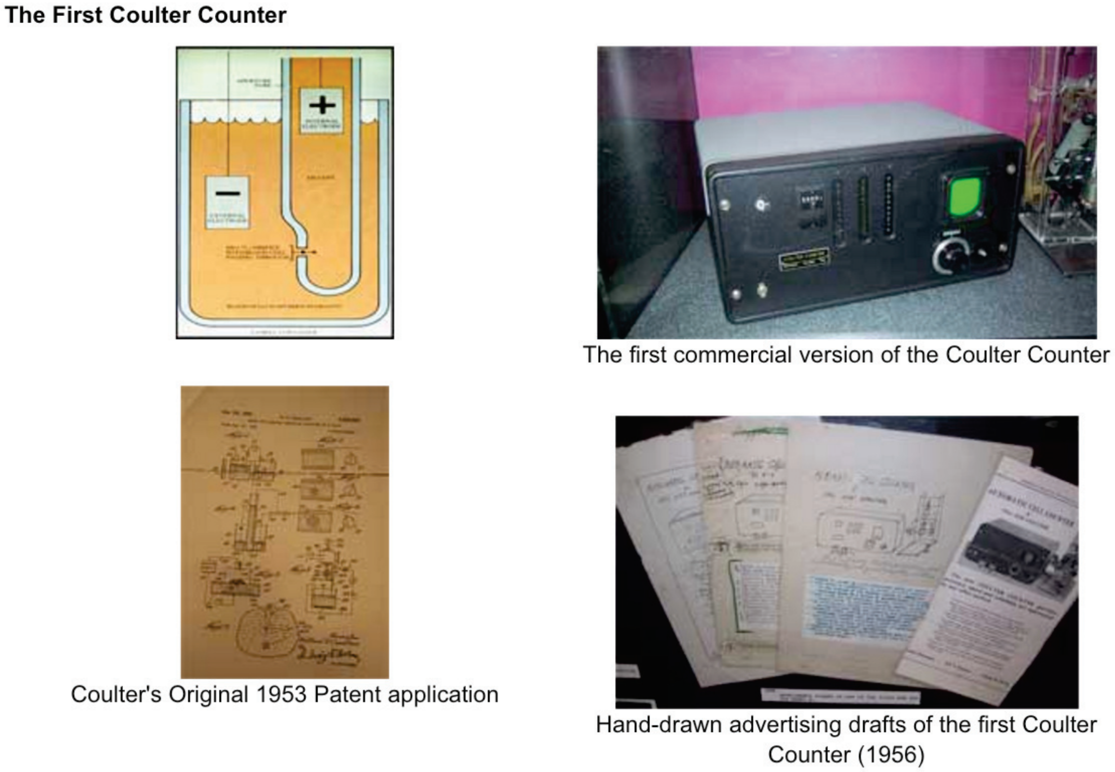

The First Coulter Counter

The first commercial version of the Coulter Counter

Coulter's Original 1953 Patent application

Hand-drawn advertising drafts of the first Coulter Counter (1956)

Figure 2.2. The First Coulter Counter

Available on: http://www.beckman.com/coulter-flow-cytometry/history

Two important developments occurred in the evolution of flow cytometers in 1953 (Schmid, 2012). First, P.J Crossland-Taylor developed a device to count red blood cells introducing hydrodynamic focusing for the first time. A flow chamber was designed to provide hydrodynamic focusing so that all cells were suspended in the fluid through a tube (Crosland-Taylor, 1953). The Crossland-Taylor model was, in fact, an adopted version of Gucker's photo-electric counter (Shapiro, 2005). Today, all flow cytometers use hydrodynamic focusing via sheath fluid. The second important improvement was the Coulter principle. Coulter's invention allowed detecting and counting particles suspended in a fluid or saline solution with an electrical conductivity greater than the cell (Coulter, 1953). The blood cells were suspended in the conductive saline solution, and when the blood cells passed through a small orifice, they created a resistance or an impedance within the orifice (Shapiro, 2005). He reported that bigger particles created greater voltage pulses. The relationship between the size of the cells and the voltage measurement was explained by the Coulter Principle. Different types of cells, such as human, sheep and mouse cells, were investigated and their size distributions and pulse characteristics were determined by the Coulter counter (Coulter, 1956). He took a patent for his invention and today, many haematology analysis devices use the Coulter counting (Henriquez et al., 2004).

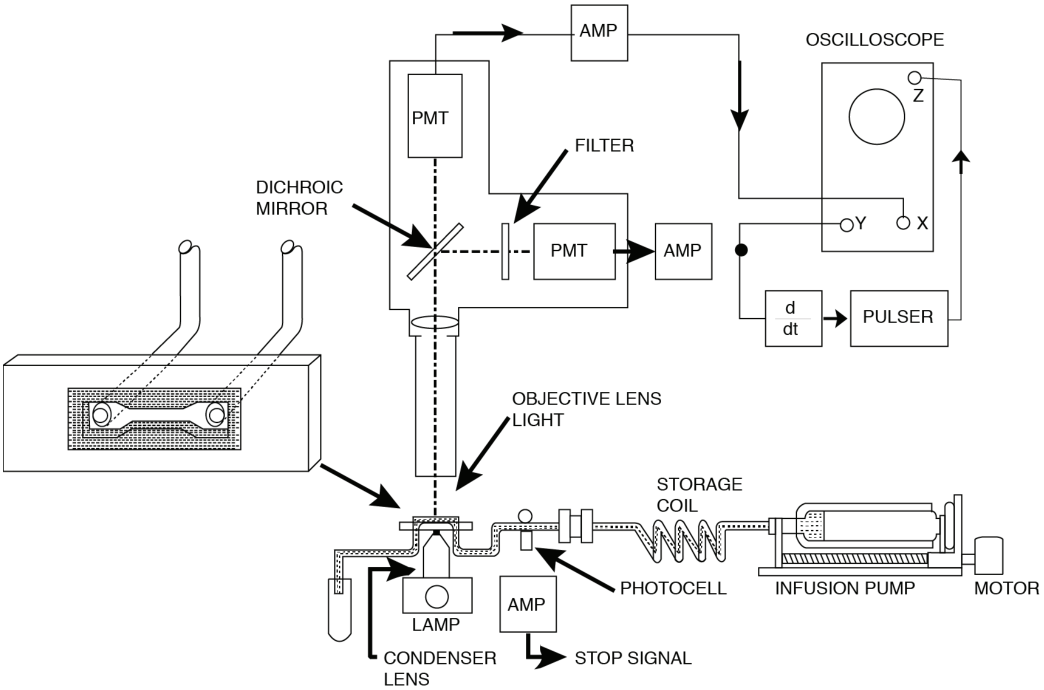

Figure 2.3. Kamentsky's flow cytometer

Adapted From: (Kamentsky et al., 1965)

A two-parameter flow cytometer was developed by Kamentsky in 1965 (Kamentsky et al., 1965). Firstly, they stained and isolated the nuclei of cells. Then, they screened and measured the size and absorption of cell nuclei under visible light and fluorescence in 1963 (Kamentsky et al., 1963). Then they made further improvements and studied stained and unstained smear cells such as cancer, normal and abnormal cells using visible and ultraviolet light. These cells were photographed at different wavelengths using which they constructed their absorption profiles. On the other hand, they could not distinguish cell nucleus from the cytoplasm (Kamentsky et al., 1963). Two years later, they developed a device that could measure and display multiple spectrophotometric properties of cells such as nucleic acids and cell functionality in 1965 (Kamentsky et al., 1965). The device could count 500 cells per second and it was studying according to two parameters as absorption and scattering. Furthermore, they determined that background scattering was originating from unstained cells. The device estimated the amount of nucleic acid per unit volume of each cell in a cell population (Kamentsky et al., 1965), and is generally accepted as the first multi-parameter flow cytometer (Macey, 2007). The first cell sorter was developed concurrently as the other major improvement in 1965 (Fulwyler, 1965). The device separated the cells according to their volumes. The alters used device to identify human and mouse erythrocytes and mouse lymphoma cells in a cell mixture (Fulwyler, 1965).

The first fluorescence-based flow cytometer was developed by Van Dilla at Los Alamos National Laboratory (Van Dilla et al., 1969) and Dittrich and Göhde at Germany (Dittrich and Göhde, 1969) in the same year. The Los Alamos research group developed a high-speed flow system that could count 10000 to 100000 cells in a minute. They used the hydrodynamic focusing principle, an 488 nm argon ion laser as a light source and a photomultiplier tube in their system. In cell preparation, DNA of human leukocytes and Chinese hamster ovary cells were stained with Feulgen. They observed asynchronized growing of the Feulgen-DNA distributions on Chinese ovary cells. Then, they made volume and Feulgen-DNA measurements on normal human leukocytes and observed differences between Feulgen-DNA and volume distributions. They observed bi-modality at the volume distributions: small particles such as small lymphocytes caused the smaller peak, and the larger peak was representing the larger cells such as granulocytes and others, while the fluorescence distribution had a single peak depending on DNA content and dye amount (Van Dilla et al., 1969). Their study was aimed at identifying the cancer cells from the healthy cells based on their sizes.

The ICP-11 impulse cyto-photometer (Dittrich and Göhde, 1969) was the first commercial fluorescence-based flow cytometer, developed in 1969 (Schmid, 2012). For illumination, they used an arc-lamp (Shapiro, 2005), wavelength sensitive dichroic mirrors, longpass, and shortpass filters (Sack et al., 2009). In their study, they stained DNA with ethidium bromide instead of Feulgen staining (Shapiro, 2005).

Fluorescence-Activated Cell Sorter (FACS) was developed by Leonard Herzenberg and his group at Stanford University in 1972. They used argon ion laser for illumination and they stained cells with fluorescein and rhodamine. This instrument was later commercialized by Beckton Dickinson in 1974 (Shapiro, 2005). Two-colour immunofluorescence using FACS was developed in 1977 (Loken et al., 1977). The first clinical-use flow cytometers were developed in 1983 (Macey, 2007).

In the following years, further developments in computers, dye chemistry, lasers and other related fields contributed to additional improvements in the flow cytometer technology.

2.1.1. Biomarker Staining Using Monoclonal Antibodies

Monoclonal antibodies have great importance in the development of flow technology. They are widely used in medical and drug research, diagnosis and classification of diseases (Production, 1999). The first multi-parametric cell counting method was performed using monoclonal antibodies in 1977 (Loken et al., 1977). In following years, the development of the monoclonal antibody technology was awarded the Nobel Prize in medicine in 1984 (Givan, 2013). Monoclonal antibodies identify specific target antigens on cells that are of significance for many diseases (Provan, 2005). The detection and labeling of specific cell populations are carried at using monoclonal antibodies. Generally speaking, when a foreign substance enters the body, the immune system attacks it and makes a large number of antibodies that encircle circulate the foreign substance. The antibody is a protein that identifies and neutralizes the antigen or foreign objects by specific binding.

A monoclonal antibody recognizes only one specific protein and binds that target protein. A particular type of immune cell produces monoclonal antibodies that are identical, and all clones or cell lines belong to a single cell parent. B lymphocytes derive the cell lines. The monoclonal antibodies are produced and designed to a specific target antigen in a laboratory environment. They have identical binding antigen binding domains or sides (Provan, 2005).

The monoclonal antibodies are produced by using immunization of an animal. First, immune cells are obtained from the spleen of the mouse, and fused with cancer cells which are the tumour of lymphocytes as myeloma. This process provides a hybridoma that is dividing and growing cells limitlessly. The hybridoma cells secrete the

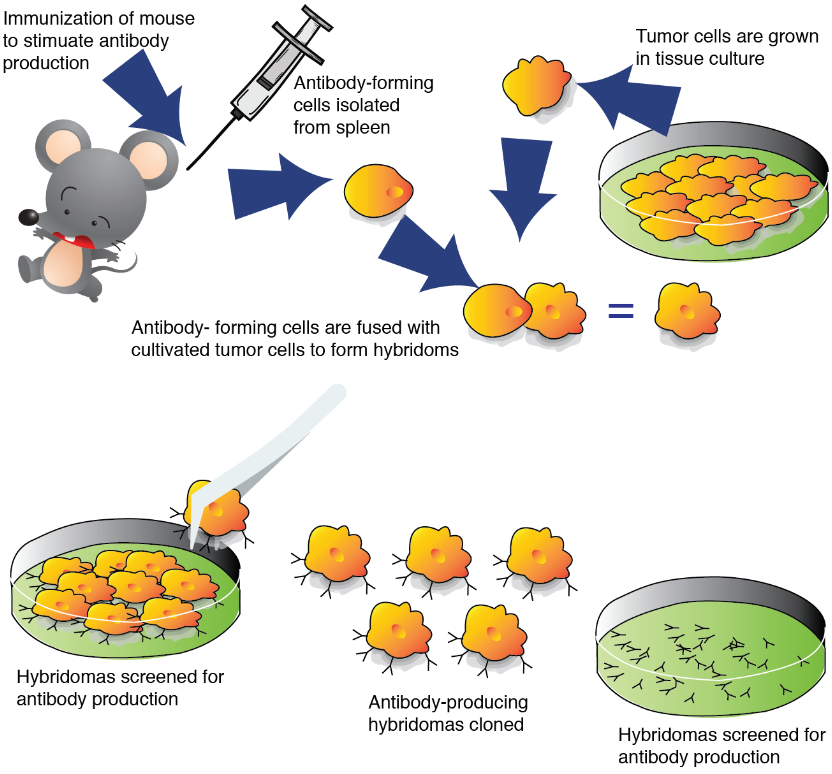

Figure 2.4. Process of Monoclonal Antibody Production

Adapted from:https://speakingofresearch.com/tag/monoclonal-antibodies/

monoclonal antibodies (Production, 1999). The monoclonal antibodies are used to identify and determine the cell types using cell surface proteins, in the heterogeneous cell populations through a process called immunophenotyping.

A polyclonal antibody recognizes multiple epitopes such as collection of many immunoglobulins on the same antigen. In the polyclonal process, the target proteins can bind to more than one antibody. When we compare the polyclonal antibody with the monoclonal antibody, the polyclonal process is inexpensive, quick producible, highly stable, less complex, allows more robust detection but with background noise. The monoclonal process is expensive to produce, more time to produce, less background noise, more homogeneity and less robust detection. All of these reasons, flow cytometers use the monoclonal antibodies.

Flow cytometry uses fluorescent dyes to identify a particular cell type in a cell population. The developments on fluorescent dyes are as old as the invention of the microscope and the evolutionary of the fluorescent dyes is related to the microscope and their using of many of areas (Rosenthal et al., 2009). The microscope was developed by Robert Hooke in 1665 and Antonie van Leeuwenhoek in 1673 and the first view of a stained object by Robert Hooke in under the light microscope in (Evanko et al., 2011). The first fluorescent dye was discovered by Adolf von Bayer in 1871, which was fluorescein (Evanko et al., 2011). From Robert Hooke to the present day, many new advances were achieved for the fluorescent dye technology, and all of these advances play a crucial part in cell biology, dye chemistry, and medicine.

A flow cytometer gathers information from the fluorescence of the fluorophore-conjugated cells. Staining of cells with fluorescence dyes aims to label a protein of interest in a cell. When the specimen is stained with fluorescent dyes, each fluorochrome-conjugated antibody finds and binds to its target molecule. This process between the target protein and the fluorochrome-conjugated antibody is typically described by key and lock model in protein-protein interactions. While some fluorescent dyes bind membrane molecules, some of them enter the cell then stain the markers on the cytoplasm.

Fluorochromes are excited at certain wavelengths of light and after the excitation, they emit light at longer wavelengths through fluorescence. In flow cytometry, the selection of a fluorescent dye is very important for identification of the cell types: an incompatible dye causes toxicity and damage in the cell (Shapiro, 2005). Another important point for the choice of a dye to label cytoplasmic targets is that the cell membrane must be permeable for fluorescent dye. Especially when the specimen contains living cells, the permeability of the cell membrane becomes vital, as investigation time of living cell becomes limited. So the selection of a fluorophore depends on the type of cells and excitation light sources. In the early years, fluorescent dyes were selected for their primary fluorescence or autofluorescence in fluorescence microscopy. But now, fluorochromes are developed for their brightness.

In a multicolor flow cytometry experiment, the most common fluorescent dyes are fluorescein isothiocyanate (FITC), propidium iodide, Phycoerythrin (PE), Alexa Fluor, and Rhodamine to name of a few, while a large number of types of fluorescent dyes are available currently (Shapiro, 2005).

2.2. Flow Cytometer Subsystems

Flow cytometer comprises four main subsystems that are fluidics, optics, electronics, and sorting. All system has crucial priorities in itself. We give the order of the systems part according to working principles.

2.2.1. Fluidics

The fluidics subsystem is responsible for transporting the cells in a stream to an interrogation point that is also the measurement point. The most significant part of the fluidics subsystem is hydrodynamic focusing as the sheath flow, that guides the sample fluid or sample core that contains the cells to the center of the flowing stream. Another important property of hydrodynamic focusing is that it restricts the diameter of the core stream in a very small region to make sure that the cell covers the interrogation volume. The sheath fluid encloses the sample fluids and the two fluids never mix with each other. The sheath fluid is also responsible for preventing any obstruction of the flow. It is crucial to obtain a stable (laminar) and unobstructed flow to control the velocity and the position of the sample stream. In the event of turbulence, all measurements become inaccurate and suspect (Shapiro, 2005).

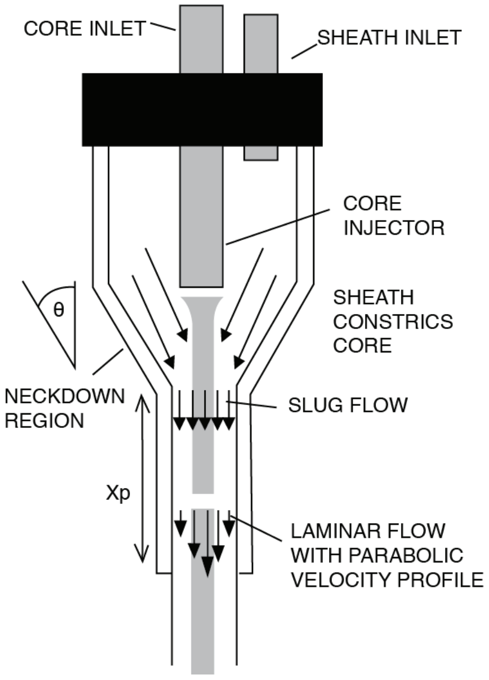

Figure 2.5. Fluid flow in a flow cytometer

Adapted From: (Shapiro, 2005)

The flow chamber is the heart of any flow cytometer. Fig.2.5 shows some aspects of the flow cytometer. In the illustration, the core inlet and the sheath inlet are at the top of the flow chamber. The flow chamber ensures that the cells pass through the interrogation point in a single file. The core injector at the center brings the sample to the flow cell (Shapiro, 2005). The characteristics of the flows are controlled according to fluid dynamics principles.

2.2.1.1. Laminar Flow

The core flow must be laminar for accurate measurements, which can be achieved by controlling the core velocity and position (Shapiro, 2005). In stationary flow, the velocity of the flow does not change with time at any given point in the system. For this reason, the flow velocity is also time-independent for steady flow. The conservation of mass principle says that the exact volume of fluid must pass at the same time through the narrow and wide parts of the capillary. So the velocity of the wider portion of the capillary is smaller than the velocity of the narrow portion. The product of the cross-sectional area and the average velocity must be constant according to the conservation of mass principle, and this product gives the flow rate. The sheath fluid and the sample fluid have the different viscosity that determines the characteristics of their flow. In addition, the velocities of the fluids are also different from each other: The velocity of the sheath fluid is greater than the core fluid and the pressure of the sample fluid is greater than the pressure of the sheath. When the sheath fluid moves, it causes a massive drag effect on the narrowing center of the flow chamber (Shapiro, 2005). The drag effect changes the velocity of the center fluid parabolically while the velocity at the wall of the tube is zero (Shapiro, 2005). Howard Shapiro and his group made experiments on a cylindrical tube with radius R that contained flowing water to determine the flow profile (Shapiro, 2005). They found the velocity of water at a different number of distances from the center of the tube. While the highest water velocity was through the center of the tube, the velocity at the wall of the tube was zero. Finally, they measured the water velocity at any intermediate point with a distance r along the radius, and they found that the velocity varied with $(R-r)^2$, and it had a parabolic profile. In conclusion, they reported that the velocity of the fluid could not be assumed constant over the entire cross-section of the tube, and they added that they could make their calculations using the average velocity and the conservation law.

Sudden changes in the shape of the tube affect the behaviour of the flow (Shapiro, 2005). The tube shapes are thus designed to avoid initiating turbulence. For this reason, in Fig.2.5, the angle θ at the neck-down region is chosen to be approximately 30°. Reynold firstly explained the conditions for laminar flow in fluid flow through the tube in 1883 (Reynolds, 1883). The Reynolds number is used to determine the stability of the fluid flow. The characteristics of the central flow are determined by comparing the Reynolds number with a constant value. If the Reynolds number is smaller than 2300, then the flow is characterized as laminar; otherwise, the flow can be turbulent. The Reynolds number is determined by the following equation;

$$R_e = \frac{\rho V D}{\eta} \tag{2.1}$$

where R_e is Reynolds number, ρ is the density of the fluid, η is the viscosity of the fluid, and V is the mean velocity (Shapiro, 2005).

Any complete or partial obstruction in the flow tube can result in turbulent flow. Obstruction affects the velocity and trajectory of a big range of the particles, and also affects all measurements made at the optical and electronic systems of the flow cytometer. When the velocity or trajectory of cells differ, voltage pulses that are observed at the detectors are altered and this, in turn, affects the cell distributions of interest (Shapiro, 2005).

2.2.1.2. Flow Chamber

Flow chamber or flow cell is another important part of the fluidics system. The biggest role of the flow chamber is to obtain hydrodynamic focusing. There are two different types of the flow chamber, which are fully closed flow chamber and microscope-based flow chamber (Shapiro, 2005).

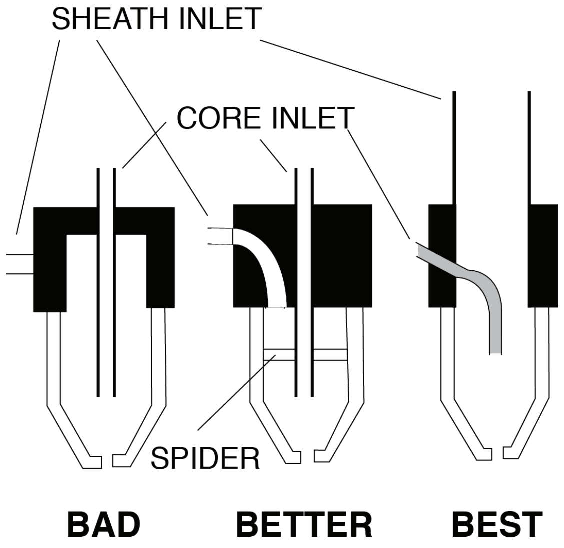

Figure 2.6. Turbulence affect according to shapes of sheath and core inlets at the flow chambers (Adapted From: (Shapiro, 2005))

Flow chamber generally comprises a sheath nozzle which ends with a conical orifice to obtain hydrodynamic focusing. When the sample fluid is injected by the core nozzle, it causes a fast laminar flow. The velocity of the fluid varies between the 1-10 m/s (Shapiro, 2005). The flow velocity is adjusted according to the investigated cell or particle type.

The probability of turbulence is higher at the inlets than the outlets in some flow chamber types as the diameter of the sheath inlet tube is relatively smaller than the diameter of the flow chamber. The illustration of the shape of core and sheath inlets is given in Fig.2.6. There are three different configuration types where the diameters of the sheath inlet and also the angle with which the sheath tube feeds into the chamber are different. The configurations are ordered with respect to their performances.

2.2.2. Optical System

Flow cytometry is strongly related to light. The optics system comprises two subsystems; excitation and collection optics. Two types of light scattering are significant in flow cytometry: side scattering and forward scattering. The scattered light gives information about measurable parameters of the cells and particles. Selection of the components of excitation optics system is based firstly on compatible excitation light sources with significant fluorescent markers of the cells, while collection optics system is designed to detect light scattering that, it directs to appropriate detectors to determine the fluorescence amounts.

2.2.2.1. Excitation Optics

The optics system of a flow cytometer has two important responsibilities: illumination of cells and detection of emitted light. Excitation optics is involved in exciting the fluorophore molecules. Components of excitation optics are lasers, fiber optic cables, beam-shaping prisms and an achromatic focusing lens. Lasers are light sources that are commonly used to excite the fluorochromes, though some flow cytometers use arc lamp as a light source. Excitation optics brings the light from lasers to focus on the flow cell by means of beam-shaping prisms and an achromatic focusing lens. Below, we give details about fluorescence, fluorescent dyes, light scattering along with the equipment of the excitation optics.

Lasers: Lasers are essential light sources in flow cytometer technology. The first idea of stimulated emission is described by Einstein in 1917 (Einstein, 1917). Einstein argues that when a molecule or atom absorbs a photon, it is excited as an electron rises to the upper energy state. The excess energy causes the emission of a photon caused by the electron returning to the lower energy state. While the photon returns the lower energy state interacted with another photon at the same medium, the interacted photon is stimulated. These photons are described as stimulated or induced in the same direction, phase, and identical frequency. After years from the postulate of Einstein, the laser was invented by Theodore Maiman in 1960 (Maiman, 1960). Expansion of laser is light amplification by stimulated emission of radiation. Lasers generate coherent photons, then the generated light is amplified. The invention of laser leads additional innovations that extend many research areas. For instance, in flow cytometric measurements, the first flow cytometer was developed by two different groups and one of them was Los Alamos group that used a laser, for the first time in fluorescence flow cytometry (Van Dilla et al., 1969): They had used a 488 nm argon ion laser.

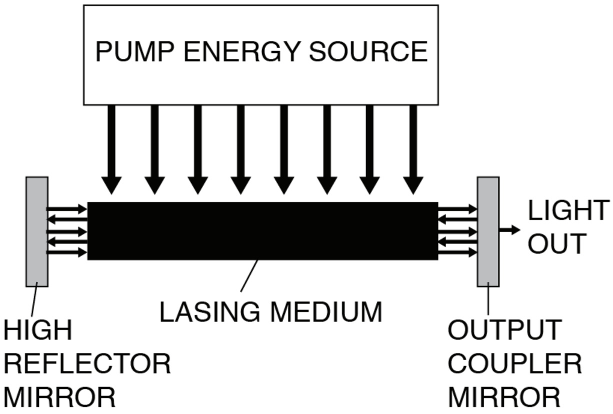

Figure 2.7. Schematic of a laser

Adapted From: (Shapiro, 2005)

In Fig.2.7, lasing medium is excited by a pump energy source that has high intensity, causing stimulated emission occurs in the lasing medium. The volume of the lasing medium is critical; it is selected to provide emission certain directions.

The lasing medium is shaped into a long and narrow cylinder for commonly used laser types. The lasing medium carries in an optical cavity or resonator that increases the directionality of the lasing medium. The optical cavity comprises aligned and spaced mirrors. The output of the laser is taken from the output coupler mirror. The amount of the output light is proportional to incident light and generally, a small amount of the incident light is transmitted through the output coupler mirror because of the loss that occurs within the cavity. High reflector mirror in Fig.2.7 reflects the vast proportion of the light.

Flow cytometers use different types of lasers and the most commonly used lasers are argon and krypton ion lasers, dye lasers, and helium-neon lasers.

- **Argon and Krypton Lasers:** Argon-ion lasers are powerful gas lasers and the most commonly used laser types in flow cytometers. The lasing medium is plasma which comprises high density argon ions. The plasma is obtained by an intense electrical discharge between two hollow electrodes. A solenoid around the tube generates a strong magnetic field and the ionization of the gas starts the plasma by a high voltage. The krypton lasers work according to the same principle with the argon-ion lasers. Argon-ion lasers are generally operated at 488 nm, so that they excite various fluorochromes FITC and PE.

- **Dye Lasers:** Another commonly used laser type in flow cytometers is dye laser. The lasing medium is a fluorescent dye selected specifically to dissolve in organic solvents. Dye lasers are used in immunofluorescence measurements generally in two colour experiments.

- **Helium-Neon Lasers:** Helium-neon lasers are also frequently used excitation light sources, and such as their stability and small size in a flow cytometer. Typically, they are 633 nm red lasers.

2.2.2.2. Collection Optics

Collection optics gather the scattered and emitted light from the cells and route the fluorescent light to appropriate detectors. Collection optics part is equipped with different detector arrays that contain photomultiplier tubes, photocathode, bandpass filters, longpass filters, optical blank holders, beam-splitters, lenses, and dichroic mirrors. The lenses collect the scattered light and focus it onto fiber optic cables. The fiber optic cables direct the light to appropriate detector arrays, organized as octagon or trigon arrays. The filters transmit specific wavelengths of the fluorescent light located towards the detectors.

Filters: Collection optics system firstly collects the fluorescent light scattering and direct the light towards the detectors. The filters are used for distributing the light through all the detectors. The flow cytometers most commonly use bandpass filters and long-pass filters. Each flow cytometer has a different number of filter types according to their multicolor technology.

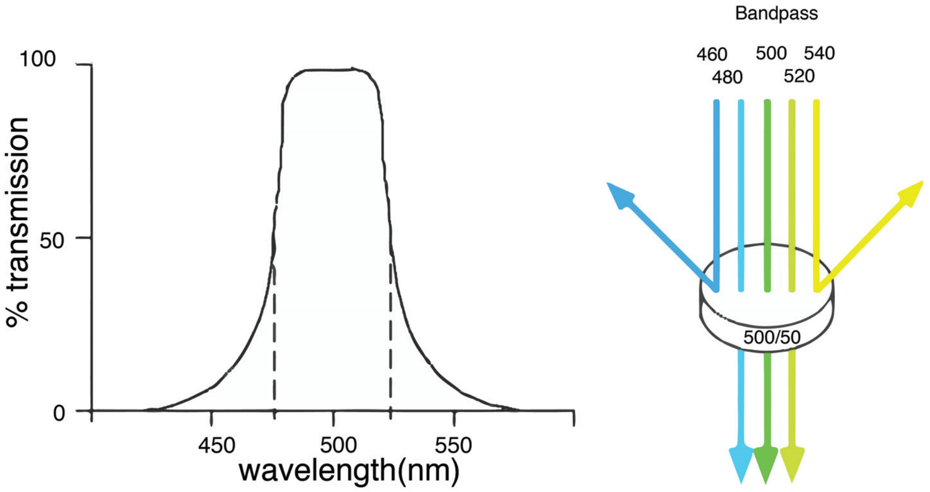

Figure 2.8. Bandpass Filter

Adapted From: (BD FACSCanto, 2006)

Bandpass filters have a variety of applications such as flow cytometry, fluorescence microscopy, and clinical chemistry. Flow cytometers contain a different number of bandpass filters which are selected to match fluorescent dyes and excitation light sources. Bandpass filters transmit a specific range of the spectrum while blocking other wavelengths and differ in terms of their absorption and transmission characteristics. The most common passband widths in the bandpass filter vary between 20 nm and 70 nm.

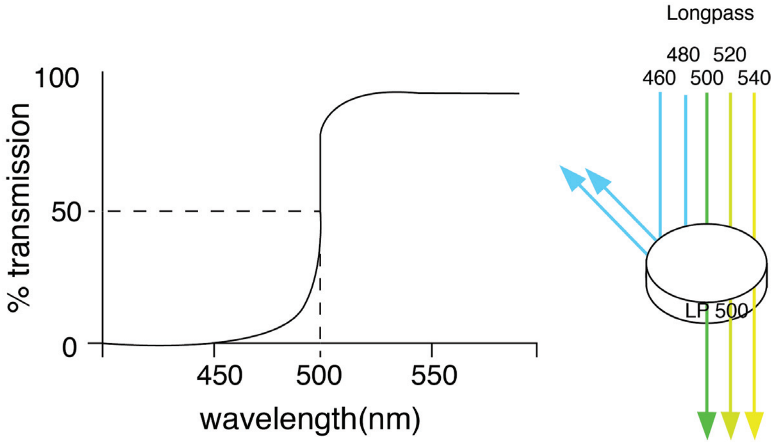

Figure 2.9. Longpass Filter

Adapted From: (BD FACSCanto, 2006)

In contrast, longpass filters transmit wavelengths that are greater than their rating. Longpass filters vary in terms of their transmission and reflection characteristics. Similar to bandpass filters, longpass filters are also chosen according to the excitation source and fluorescent dyes.

Beam-splitters: Beam-splitters are common optical components that are routinely used in illumination and laser systems. Beam-splitters split incident light by a percentage of overall intensity at a designated ratio into two separate beams according to either polarization or wavelength. The optical systems of flow cytometers contain plate or dichroic beam-splitters or mirrors. The dichroic beamsplitters are used as longpass filters in the collection optics part of a flow cytometer.

Blank Optical Holder: Blank optical holders contain no glass. They merely occupy the slot at which they are placed to prevent unwanted ambient light from getting inside the flow cytometer.

Photomultiplier Tubes: Photomultiplier tubes are important components of the collection optics. They are quite sensitive light detectors which convert light to electrical current as a result of a process that amplifies the number of photoelectrons through a cascade and then converts the charges to current. Detector arrays that use photomultiplier tubes to collect side scattering fluorescence signal in the flow cytometer. A photomultiplier tube detects the weak signal and then amplifies it. The photomultiplier tubes are comprised of a vacuum phototube, a photocathode, an electron multiplier or dynodes, anode and have an output circuit.

Light enters from the input window. The incident light hits the photocathode and causes emission of electrons. Then the emitted electrons are accelerated and focused by using focusing electrodes onto the first dynode in Fig.2.10[1]. The dynodes cause secondary electron emissions that repeat through all dynodes. Then, all multiplied electrons at the last dynode are collected from the anode. Lastly, all charges in the anode are converted to electrical current.

- **Photocathodes:** Light enters PMT by means of the input window and hits the photocathode in Fig.2.10. Photocathodes are comprised of the light-sensitive materials that are mostly alkali metals. Photocathodes of PMT used in flow cytometers are

---

[1] Available on:http://www.olympusmicro.com/primer/digitalimaging/concepts/photomultipliers.html

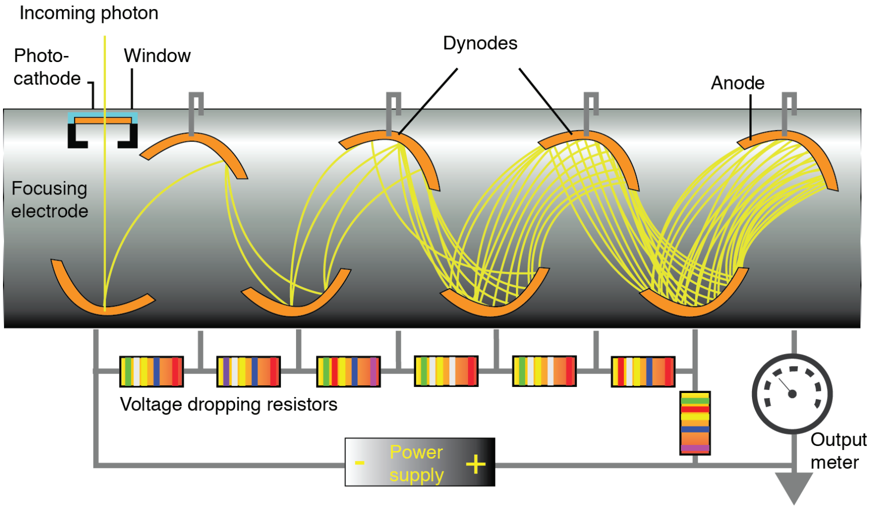

Figure 2.10. Schematic of a photomultiplier tube

multi-alkali tubes that are selected to match desired spectral response ranges. When the light hits the photocathode, it responses by emitting electrons. The emitted electrons occur as a result of the photoelectric effect that was described by Einstein in 1905 (Einstein and into English, 1965). The electrons are emitted due to the photoelectric effect are called photoelectrons. Thus, photocathode effectively converts the incident light energy to photoelectrons. The relationship between the incident light and the photocathode is determined by characteristics of spectral response.

- **Radiant Sensitivity:** Photocathode sensitivity is the ratio of the photocathode current to incident radiant flux. This relationship is given by the following equation;

$$S_k = \frac{I_k}{\Phi_e} \tag{2.2}$$

where S_k is the radiant sensitivity, I_k is the photocathode current and Φ_e is the incident light flux. The unit of the radiant sensitivity is ampere per watt, though many sources use milliampere instead of ampere because the generated current can not be greater than milliampere range. This equation is for monochromatic radiation and the photocathode surface is not uniform. In actuality, the radiant sensitivity depends on the wavelength of radiation as well as the type of cathode surface (Hamamatsu, 2006a).

- **Quantum Efficiency:** Quantum efficiency is the ratio of number of emitted photoelectrons from the photocathode to number of photons of incident light, defined by,

$$q_{radiant} = \frac{n_k}{n_p} \tag{2.3}$$

where $q_{radiant}$ is the quantum efficiency, n_k is the number of emitted photons and n_p is the number of incident photons.

The quantum efficiency can also be obtained from the radiant sensitivity S_k using the following equation

$$q_{radiant} = S_k \frac{hc}{\lambda e} \tag{2.4}$$

where h is Planck′s constant, λ is the wavelength of the incident light in nanometres, c is the speed of light in vacuum in meters per second, and e is the electron charge in Coulomb (Hamamatsu, 2006a).

- **Dynodes:** Dynodes are electrodes that are used for secondary electron emissions and the surface of dynodes are coated with photoemissive materials. The dynodes are also called electron multipliers. Positive high voltages are applied to each dynode and the supplied voltages gradually increase between each dynode. The voltage between the dynodes is adjusted with resistors in bleeder circuits. Applied voltages and bleeder circuits depend on the type of the PMT. The supplied voltage accelerates the emitted electrons. The gain of the photomultiplier tube is proportional to the number of dynodes.

- **Anode:** An anode is an electrode that collects the secondary emission electrons at the last dynode. The geometry of the anode is designed to collect all secondary electron emissions. The transition of the secondary emission electrons to the anode is guided by applying a high electrical field between the last dynode and the anode. Anodes also have their own sensitivity characteristics.

  The output of the PMT is a current that is converted to the voltage by means of a voltage divider and amplifier circuits.

2.2.3. Electronics

The main functions of the electronics subsystem are converting the light signal into a proportional electronic signal, digitizing the electronic signals, eliminating small signals as noise, autofluorescence, and debris and finally sending the data to a computer. The electronic subsystem is comprised of photo-detectors, amplifiers, and signal processors.

These electronic parts work in order to convert firstly the light signal into a current, then the current into a voltage, and finally the voltage into digital data for further analysis. As described earlier, photomultiplier tubes convert the light signal into currents in the detectors. The pre-amplifier circuit is placed at the output of PMT and essential pulses that determine characteristics of the cells are observed at the output of the pre-amplifier circuit.

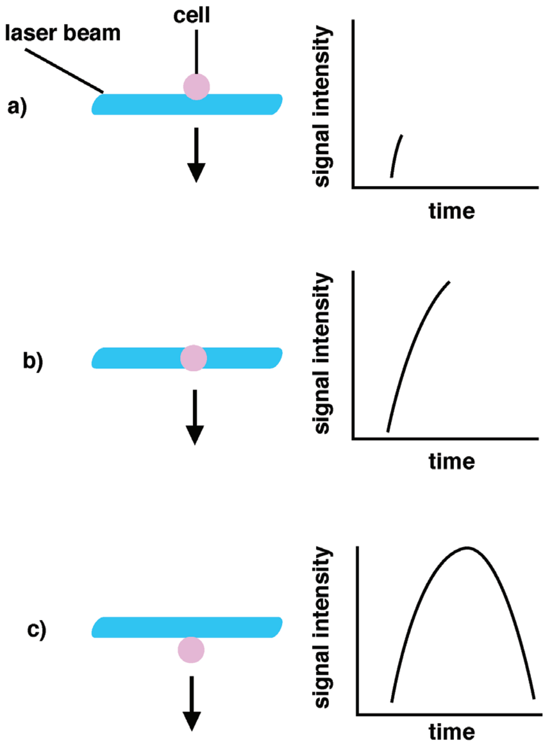

Figure 2.11. Anatomy of a pulse

Adapted From: (BD FACSCanto, 2006)

The evolution of a pulse begins at the time of the first intersection of the laser beam with the cell. The pulse gradually increases until the cell reaches the middle of the laser beam, then the cell continues to move and the pulse decreases until the cell exit the laser beam. An illustration of this process is given in Fig.2.11. Signal processors quantify the width, the area and/or the amplitude of voltage pulses. These quantifications give information about the size and granularity of investigated cells. The collected data is transferred to a computer for storage and statistical analysis. We give further details of the pre-amplifier circuit in the following chapter.

2.3. Flow Cytometry Data Analysis

Flow cytometry data analysis comprises data collection and data processing parts. Light signals are generated as cells pass through the laser beam at the interrogation point. The light signals are converted to voltage pulses as electronic signals that are converted to integer numbers by analog-to-digital converters. The computers store the data according to flow cytometry standard (FCS) developed by International Society for Advancement of Cytometry (ISAC). The computers save digital data as a list that includes multiple measurements for each cell for basic and advanced data processing, such as statistical analysis. The stored data can also be displayed in varies scales, typically using log and bi-exponential scaling. When the data is displayed on a log scale, some of the data can fall on or below the axes. In this case, bi-exponential scaling plot turns on displaying the data. The events can be displayed as the histograms, as dot, density and contour plots. Data analysis part involves data displays, the creation of the gates and statistical analysis and a manual expert analysis for biological interference.

2.3.1. Gating on Scatter Plots

Gating is an important process for flow cytometry data analysis. It is a procedure that extracts only interested cells while eliminating unwanted results coming from unwanted cells, dead cells, autofluorescence, and debris. A gate is a numerical or graphical boundary that is used to define measurement characteristics for cells to be included in further analysis. Gates are also used to identify subset populations of interest. Gating can be made either manually and automatically. Populations defined according to the gates used to generate statistics. There is one more than gate types.

An interval or histogram gate specifies a boundary around a meaningful range of events in a histogram plot. A quadrant gate divides a flow cytometric scatter plot into four separate populations are quadrant four populations. A polygon gate specifies a boundary around a population on a dot, contour or density plot.

Different colours are typically used to display gate events. This allows comparing subpopulations visually at the different plots.

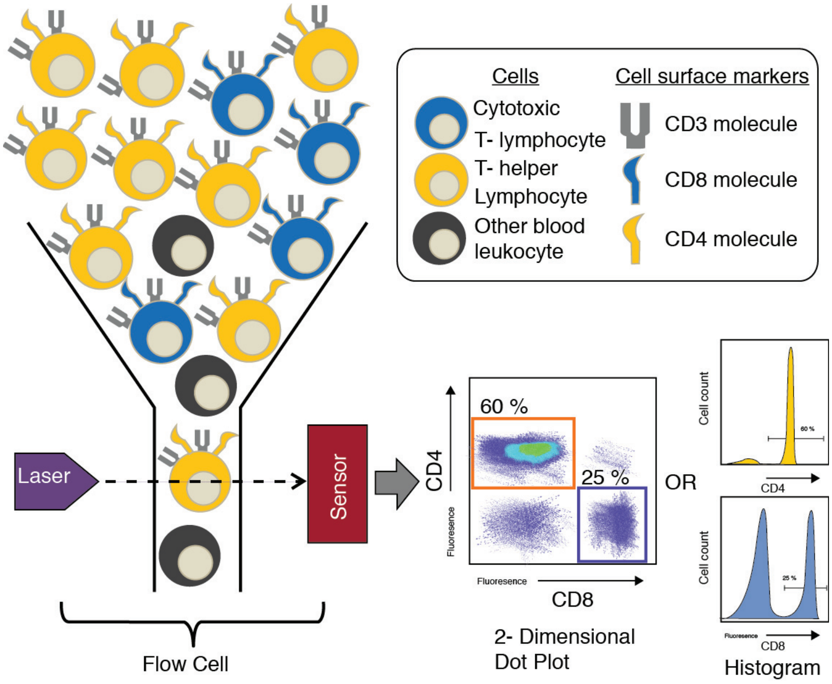

Figure 2.12. Gate Types

Adapted From: (Verschoor et al., 2015)

2.3.2. Light Scatter

When an object is exposed to light, it absorbs and scatters the light in all directions. This phenomenon is called light scattering. Both processes of absorption and scattering of light are random. The scattered light generates new photons with different wavelengths and directions. The light scattering has been exploited solve various problems related to cell biology over the last decades (Tuchin, 2011). Flow cytometers use light scattering to determine the cell structure. In a flow cytometer, the object of the study is a cell and the light source is a laser. Cells stained with fluorescent dyes are transported to the interrogation point where a laser beam hits the cells. Each cell absorbs some light energy and when released light energy scatters in all directions. The amounts of scattered light are assessed and used to discriminate cells according to their size, shape, morphology, and granularity. One of the most important points of the light scattering is that incident beam angle has a specific direction in flow cytometry; so that the detector collect the only side scattered light. Forward and side scattering is explained in some details in the following paragraphs.

The intensity of the scattered light depends on the ratio between the size of particles and the wavelength of the light source. Light scattering has different patterns in

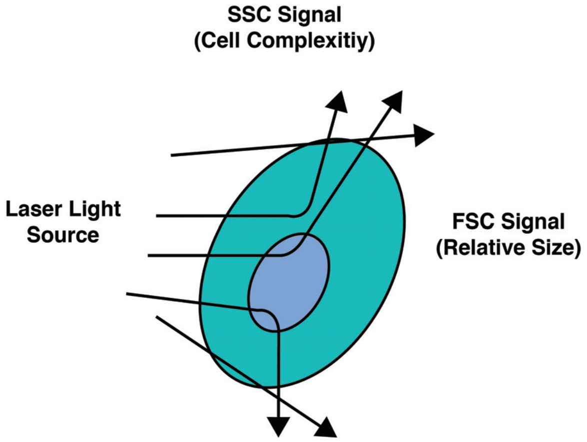

Figure 2.13. Forward scatter (FSC) and side scatter (SSC)

Adapted From: (BD FACSCanto, 2006)

case the diameters of cells are greater than the wavelength of the laser and when the diameters of cells are smaller than the wavelength of the laser. For larger cells or particles, the behaviour of the light scattering is explained by Mie theory (Shapiro, 2005), that is concerned with spherical objects and calculates the single scattering properties (Tuchin, 2011).

2.3.2.1. Forward Scattering

The angle of the scattered light that is roughly in the same direction of the laser beam is called as forward scattering. Technically, a scattering angle of $0.5 - 2^\circ$ to the incident light is called small angle scattering or forward scattering (Mullaney et al., 1969). Forward scattering gives information about cell size and examines whether the cell is dead or alive: The larger the cell size causes the stronger forward scatter light.

Forward scattering does not only depend on the size of cells or particles, but also depends on refractive indices of the sheath fluid, core fluid, and the cell itself. For this reason, the refractive index of the cell is related to their surface properties. The refractive indices of flow fluids must be different from the refractive index of the cell. Forward scattering is explained by Mie theorem (Shapiro, 2005) in the flow cytometry.

Forward scattering offers discrimination between dead cells with damaged membranes. When a cell dies destruction begins in the cytoplasm and also at the cell membrane. When the destruction of the cell membrane reaches a specific threshold, the cell membrane becomes permeable for the surface dyes that enter the cell non-specifically

(Shapiro, 2005). This causes lower forward scattering in comparison with the forward scattering of the live cell. Furthermore, when lipid packing occurs in the membrane that indicates apoptosis, programmed cell death, it affects the forward scattering (Scherer et al., 1999).

The laser beam is blocked in front of the forward scattering detector via obscuration bar that prevents the laser beam to reach the forward scatter detector when there are no cells at the interrogation point.

2.3.2.2. Side Scattering

Side scattered light is roughly perpendicular to the laser beam. Side scattering gives information about the granularity or internal complexity of the cells: The more granular cells the stronger side scattering light.

2.4. Fluorescence

Fluorescence was first described by George Stokes in the mid-1800s (Stokes, 1852). Fluorescent antibody technique was developed by Coons and colleagues in 1940′s, with immunofluorescence staining taking a big role in cell biology in the following years. Coons and his research group use fluorescein in an effort to view antibodies in their research (Coons et al., 1941). In following years, further developments on fluorescent measurements were introduced for flow cytometry in the late 1960′s (Shapiro, 2005).

Fluorescence is a quantum mechanical process (Sklar, 2005). Fluorochrome molecules are sensitive to light energy. Fluorochromes absorb light over a specific range of wavelengths. As a result, an electron is raised to a higher energy level from the ground state. This process is called excitation. Each fluorophore has different characteristic excitation range. The lifetime of the excited state is very short in a few nanoseconds, because all energy states tend to revert very quickly to the minimum energy state. Thus, the fluorophore in an excited state has an unstable high energy configuration and it goes down to the lowest excited energy state that is semi-stable. Hence, energy in the excitation state decays or decreases in a short time. The fluorophore emits the light energy as it goes down to the ground state from the semi-stable excited state. This process is called emission. The wavelength of the emitted light is longer than the absorbed light, as the emitted light energy is smaller than the absorbed light energy. In fluorescence, the process of emission follows the process of excitation that can be repeated many times. This phenomenon is known as Stokes shift that briefly states there is to be a difference between the peaks of the excitation spectrum and emission spectrum. This means that the colour of excited and emitted lights are slightly different. It is used to distinguish the excitation spectrum from the emission spectrum for the fluorescent molecules. When Stokes shift increases, it is easier to discriminate the excitation spectrum to emission.

Jablonski Diagram: The first energy transition diagram is illustrated by Jablonski in 1935 (Jabłoński, 1935), that also represents the energy states. When a fluorophore is excited by the light source, the excited molecule rises an upper energy state as in Fig.2.14. Emission occurs only between the electronic energy levels. The excess energy of the excited molecule in S_2 in Fig.2.14 causes vibrational relaxation and inner conversion, though not radiative transition or emission of a photon. The non-radiative transitions are therefore either lost or converted to heat. In Fig.2.14, the solid arrows are illustrated as radiative transitions while the dashed arrows show the non-radiative transitions.

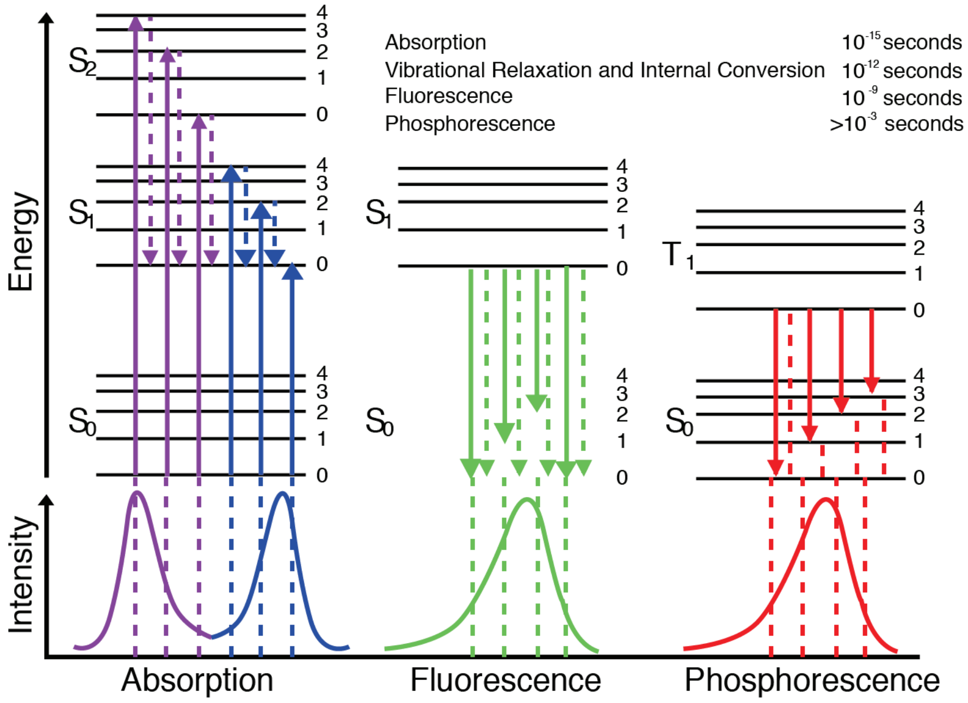

Figure 2.14. A Jablonski diagram

Adapted From: http://photobiology.info/Visser-Rolinski.html

In the diagram, there are two different energy states as singlet and triplet states. Pauli exclusion principle explains that two electrons have paired spins in the same orbital. According to the Pauli exclusion principle, singlet excited states are described as allowed, while the triplet excited states are forbidden. The process of phosphorescence occurs the triplet state to the singlet state with the longest lifetime according to the other processes.

Autofluorescence: Fluorescence does not only occur in exogenous fluorescent contents. Conversely, certain fluorescent substances present in the cells cause the fluorescence endogenously. So, the cells have a self-fluorescence property that is described as autofluorescence. These substances are present in a great number of mammalian and plant cells such as flavins and pyridine nucleotides, chlorophylls, elastins and collagen proteins (Shapiro, 2005). These molecules can generally be excited by the light sources such as a blue laser and also fluoresce in the lower energy state.

To identify the autofluorescence signal from the fluorophore signal is important in multicolor flow cytometric experiments. Because, autofluorescence from certain blood cells causes the small signal at the measurement channels, and then, the dim signals interfere with the autofluorescence signal. Autofluorescence also decreases the signal resolution and sensitivity (Shapiro, 2005).

2.5. Fluorescence Spillover

Fluorescence spillover occurs due to physical overlap between the emission spectra of different fluorochromes present in a multicolor flow cytometry experiment. Emission wavelengths of certain fluorochromes are very close to others. For this reason, if there are one more than fluorochromes in the experiment, however, the emission spectrum of a fluorochrome overflows into the emission spectra of other fluorochromes. So, the fluorescence signal other than the intended fluorochrome contributes to the intended fluorescence detector.

Optical filters are centered at the peak of emission spectra of the fluorochromes to detect only the fluorescence intensities of the intended fluorochromes as shown in Fig.2.15. But, the long tails of emission wavelengths leak into the used bandpass filters. It causes unwanted correlations between fluorescence intensity measurements and also increased fluorescence readings at the fluorescence detectors than it is an actuality.

The fluorescence intensities can be manually corrected using the linear algebra in the case of two fluorochromes. Let I_{FITC} be FITC intensity and I_{PE} be PE intensity. Then, suppose that A be a fraction of FITC fluorescence intensity interfering into the PE detector FL2 and B be a fraction of PE fluorescence intensity interfering into the FITC detector FL1. This is corresponding to a linear system with two equations and these

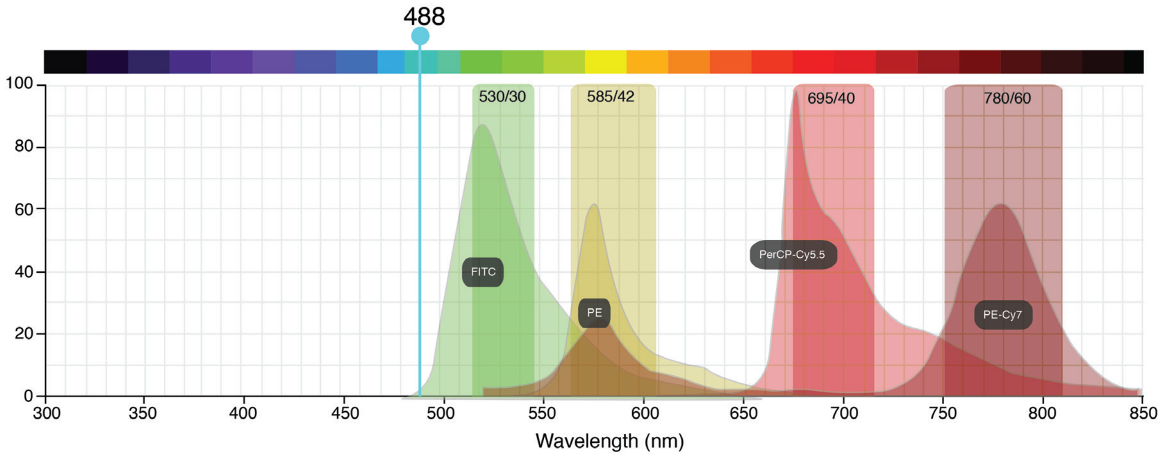

Figure 2.15. Emission spectra of different fluorochromes excited 488 nm laser with their corresponding bandpass filters

Adapted From: http://www.bdbiosciences.com/us/s/spectrumviewer

equations are given in the following equations[1] as;

$$FL1 = I_{FITC} + BI_{PE} \tag{2.5}$$

$$FL2 = AI_{FITC} + I_{PE} \tag{2.6}$$

If the A and B are known, the solution is then identified as;

$$I_{FITC} = (1 - AB)^{-1}(FL1 - BFL2) \tag{2.7}$$

$$I_{PE} = (1 - AB)^{-1}(FL2 - AFL1) \tag{2.8}$$

2.6. Compensation

Compensation is the process by which fluorescence spillover between detectors is mathematically corrected. Two colours compensation uses the equations 2.5 and 2.6. If A and B are exactly unknown, an approximate solution is derived, when A and B are much less than 1, $AB \ll 1$, $(1 - AB)^{-1}$ be approximately equal to 1. Then, the two colour compensation equations are;

$$I_{FITC} \approx (FL1 - BFL2) \tag{2.9}$$

---

[1] http://www.drmr.com/compensation/indexDetail.html

$$I_{PE} \approx (FL2 - AFL1) \tag{2.10}$$

where A and B can be determined.

Manual compensation is the process that it is adjusted to the appearance of the data. The problem complexity increasing as the number of fluorochromes increase. So, it is difficult to perform manual compensation in case of more than two colours. This increasing problem complexity requires automated compensation methods. To solve this problem, experts use FLowJo (PO Box 82636 Portland, OR, 97282), Summit (Beckman Coulter, Inc. 4300 N. Harbor Blvd. Fullerton, CA 92835), WinList (PO Box 247, Topsham ME 04086, US) programs.

CHAPTER 3

METHODS

In this thesis, all mathematical models and simulations are constructed based on the configuration of a BD FACSCanto Flow Cytometer. The parameters of the BD FACSCanto flow cytometer were obtained from various companies that manufactured the corresponding parts through the direction of BD technical and scientific team.

In this chapter, we present a numeric model of BD FACSCanto flow cytometer. This chapter begins by describing BD FACSCanto and explaining its excitation light sources and optic channel specifications. The next sections are organized as follows: modelling cells, modelling the fluorescence phenomenon absorption and emission processes, modelling the optic channel of a BD FACSCanto flow cytometer. All work is carried at in MATLAB© (1 Apple Hill Drive Natick, MA 01760-2098 USA) and LTspice© (1630 McCarthy Blvd. Milpitas, CA 95035-7417) software platforms.

3.1. BD FACSCanto Flow Cytometer

A BD FACSCanto flow cytometer is available in Biotechnology and Bioengineering Research and Application Center in our university to be used as an in vitro diagnostic device. The specifications of the BD FACSCanto flow cytometer allow multicolor analysis with up to six fluorescent markers and two scatter parameters at a time, as described in the BD FACSCanto reference manual (BD FACSCanto, 2006). Two years after the production of BD FACSCanto, BD developed FACSCanto II intended for enumeration and identification of lymphocytes.

3.2. Modelling of BD FACSCanto Flow Cytometer

BD FACSCanto Flow Cytometer optics system is comprised of two main parts: excitation and collection optics in Figure 3.1. Firstly, we explain the optical system of BD FACSCanto Flow Cytometer and their components. Then, we incorporated the operation processes of BD FACSCanto flow cytometer in our model.

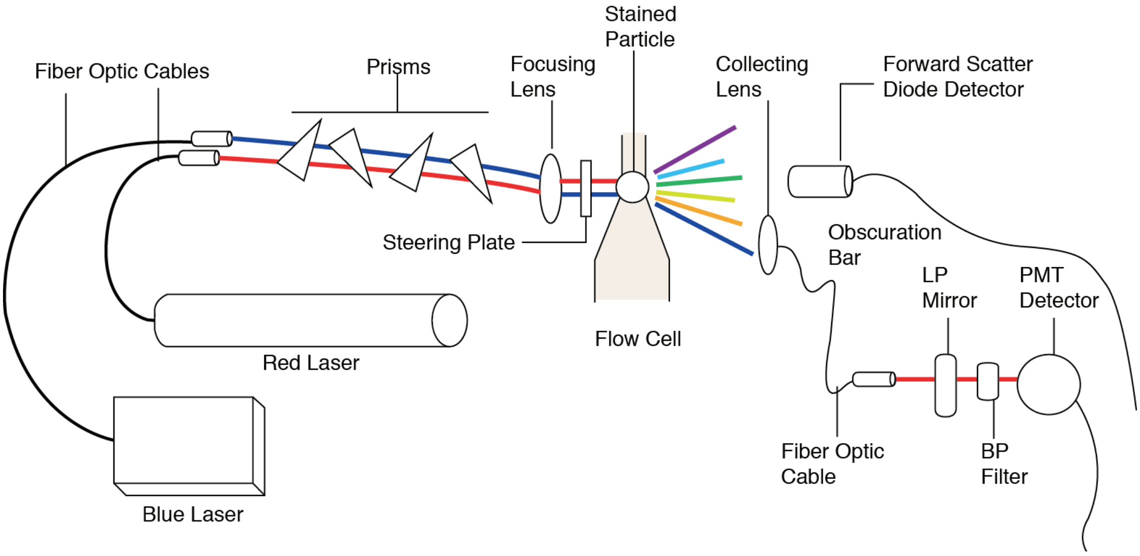

Figure 3.1. Light pathway in the BD FACSCanto flow cytometer

Adapted From: (BD FACSCanto, 2006)

3.2.1. Excitation Optics and Laser Specifications

Excitation optics subsystem brings the light from lasers and focuses them on the flow cell using fiber optic cables, beam-shaping prisms, and achromatic focusing lenses. Two different lasers are used in BD FACSCanto Flow Cytometer. They are;

- 488nm blue laser
- 633 nm red laser

The red laser has 17 mW minimum power and the minimum power of the blue laser is 20 mW. Their powers are measured at the output of the fiber optic cable (BD FACSCanto, 2006). The light is directed and transmitted onto beam shaping prisms using fiber optic cables (Fig.3.1). Four beam-shaping prisms expand the vertical axis of the laser beams scaling their original size to provide better laser distribution at the interrogation point. The achromatic focusing lens adjusts the shape of the laser profile with a height of 9μm and a width of 65μm to focus the beam onto the core stream. Lastly, the laser beam hits the cells at the interrogation point in the flow cell. We modeled the excitation process in cells with specific target fluorophores: Cells with specific biomarker concentrations absorb the laser light when they encounter the laser beam. The absorption and excitation processes occur in femtoseconds. Then, the cells scatter the emitted fluorescence light in all directions, referred to as the side scatter. In our model of the excitation process, the absorption varies according to fluorophore concentration and the cell size. Forward scatter that corresponds to laser light scattered along the incoming beam direction is not modelled, as it does not contain fluorescence light.

3.2.2. Optic Channel Specifications

Collection optics consists of one of two detector arrays: the octagon detector array and the trigon detector array (BD FACSCanto, 2006). The octagon detector array only detects the scattered light from the cells excited by 488 nm blue laser while the trigon detector array only detects light originated from 633 nm red laser. The detectors themselves are equipped with appropriate longpass and bandpass filters, photomultiplier tubes, and blank optical holders.

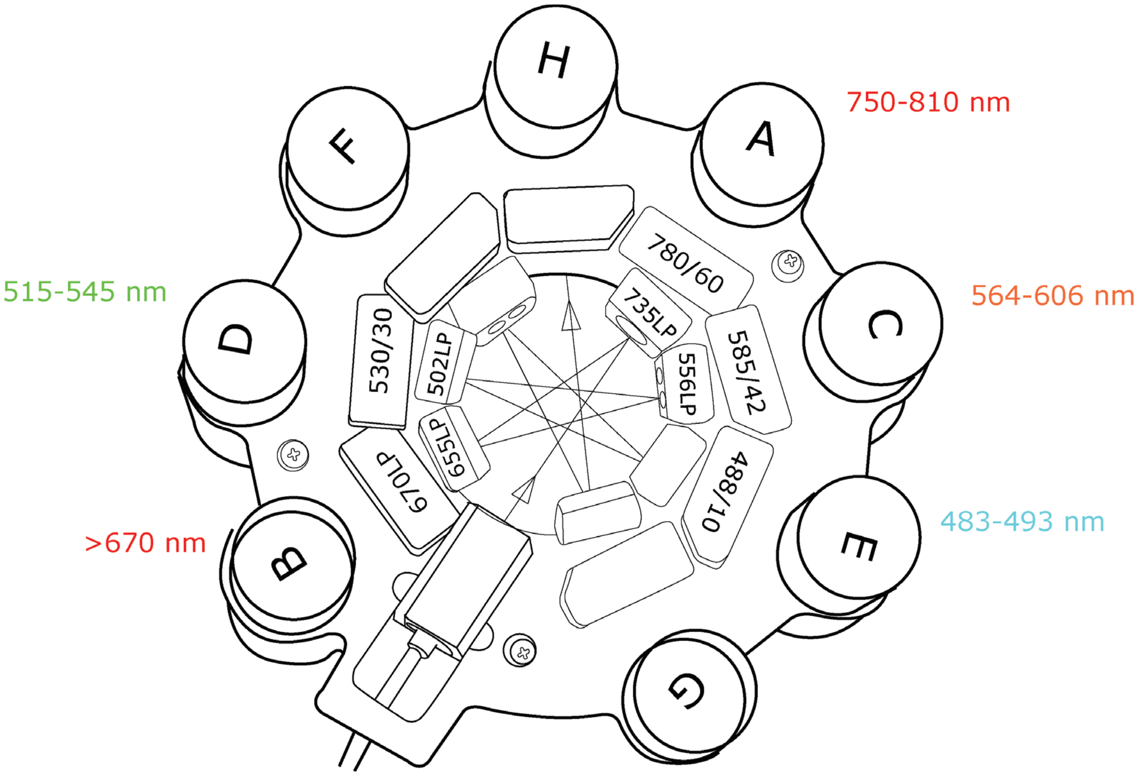

Figure 3.2. Octagon Detector Array

Adapted From: (BD FACSCanto, 2006)

We selected the octagon detector array in the simulation of the mathematical model of BD FACSCanto flow cytometer. The octagon detector array has five active detectors, the remaining three detectors contain optical blank holders and it uses the 488 nm blue laser as the excitation source. The active detectors contain longpass and bandpass filters as well as photomultiplier tubes. The filters are responsible for selective transmission and reflection of the wavelengths according to their specifications. The blank optical holders have no glass, and are simply used to block unwanted ambient light from interfering with the fluorescence signal.

The longpass filters present in the octagon detector array (Fig.3.2) are;

- 735 nm LP
- 670 nm LP
- 655 nm LP
- 556 nm LP
- 502 nm LP

The optic channel comprises four different bandpass filters. They are;

- 780/60 nm BP
- 585/42 nm BP
- 530/30 nm BP
- 488/10 nm BP

The specifications for the bandpass and long pass filters used in the BD FACSCanto Flow Cytometer were obtained from Chroma Technology Inc. (10 Imtec Lane, Bellows Falls, VT 05101 USA) and AHF Inc. (DE 72074 Tübingen, Germany). Each filter data file contains transmission percentages as a function of wavelength.

3.3. Modelling Cells

In this section, we provide the details of the quantitative data used in the simulations of cells. We modelled the cells according to the volume and the protein content properties to simulate flow cytometry readings. These readings depend on fluorescence intensity parameters that are related to biomarker concentrations in the cell. To determine the biomarker concentration and then model the fluorescence emission process, we modelled the size and protein amounts in cells. We selected the lymphocytes as cell models in our simulations. The lymphocytes are a subset of white blood cells that are part of the immune system.

In modelling of the size of cells, we used the range of lymphocyte radii from the Database of Useful Biological Number[1]. The range of the human lymphocyte diameters varies between 6.8μm and 7.8μm (Kuse et al., 1985). We created a Gaussian distribution with a mean of 3.65×10^{-6}m and a variance of 1.6269×10^{-14}m^2 to generate a random number for the radius of each cell. The probability density function of Gaussian distribution with mean μ and variance σ^2 is defined as

$$f_x(x) = \frac{1}{\sqrt{2\pi\sigma^2}} e^{-(x-\mu)^2/2\sigma^2} \tag{3.1}$$

for all $x \in (-\infty, \infty)$. The mean and variance values described above correspond to a Gaussian distribution with a 0.95 confidence interval equaling [3.4 μm, 3.9 μm]. The pink area in Fig.3.3 covers 0.95 of the probability located in the range between 3.4μm and 3.9μm.

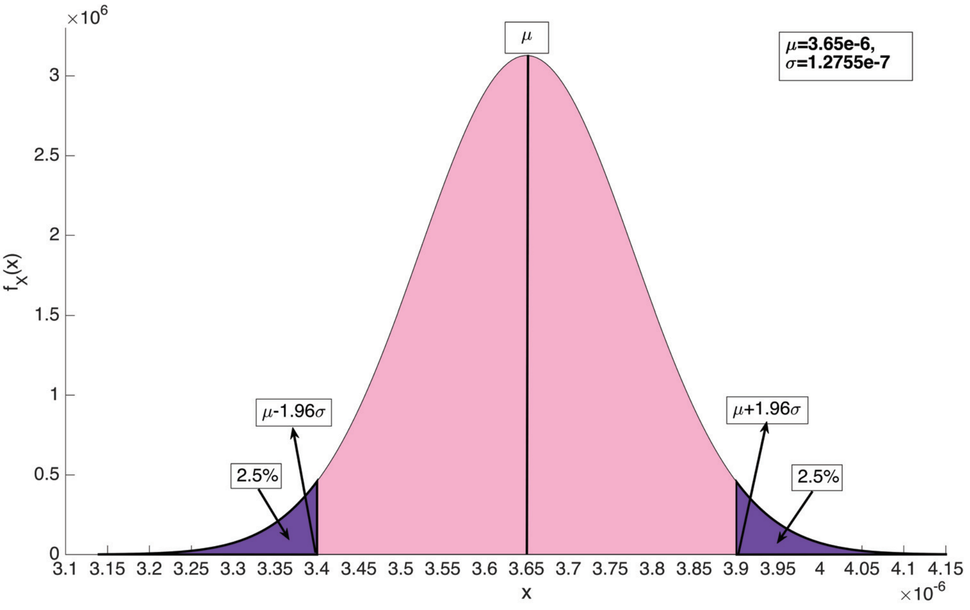

Figure 3.3. Size distribution of the cells with 0.95 confidence interval

In modelling the fluorescence process, we firstly assumed that the biomarker concentration is identical to the concentration of the target protein, and the cells conjugate uniformly to their target protein. So we modelled the cells in accordance with the number of proteins present in the cell to determine the fluorochrome concentration. We determined the number of proteins in a model cell using the statistics provided for human U2OS cells (Milo, 2013). The number of proteins in a U2OS cell varies between

---

[1] http://bionumbers.hms.harvard.edu/

0.95×10^9 and 1.7×10^9. Hence, we modelled the amount of proteins of interest for 'positive' cells using the protein range of U2OS cells. The 'positive' cells represent cells bearing fluorochromes in the simulation of cells. We firstly generated a lognormal distribution with a mean of 1.325×10^9 and a variance of 3.6606×10^9 from the range of the U2OS proteins that possesses loss confidence interval matching the range above. Then, we drew random values representing the average number of each target protein in cells expressing the target protein of interest.

Let X_1 be a lognormally distributed random variable with mean m_1 and variance s_1^2, describing, the number of, say, FITC-conjugated target protein in cells that express the target protein. Similarly, let X_2 be another lognormally distributed random variable with mean m_2 and variance s_2^2, describing the number of PE-conjugated target protein in the cells that are positive for the second protein. The corresponding probability density functions are given by:

$$f_{X_1}(x) = \frac{1}{\sqrt{2\pi s_1^2}x} e^{-(\log x - m_1)^2/2s_1^2} \tag{3.2}$$

$$f_{X_2}(x) = \frac{1}{\sqrt{2\pi s_2^2}x} e^{-(\log x - m_2)^2/2s_2^2} \tag{3.3}$$

To determine the m_1 and m_2 parameters of the lognormal protein distributions, we firstly selected the actual average numbers of each protein for positive cells μ_1 and μ_2 as $(\mu_1, \mu_2) \sim \mathcal{N}(1.325\text{x}10^9,\ (1.913\text{x}10^8)^2)$. In the following equations, the means and variances of the target protein distributions, 1 and 2, are indexed by i that are calculated using the relation between mean of normal distribution and means of the lognormal distributions as

$$\mu_i = e^{m_i + s_i^i/2} \qquad \Rightarrow \qquad m_i = \log \mu_i - \frac{s_i^2}{2} \tag{3.4}$$

The variance of lognormal distribution is given as;

$$\sigma_i^2 = e^{s_i^2 + 2\mu_i}(e^{s_i^2} - 1) \tag{3.5}$$

Since the protein numbers are provided using the coefficient of variation CV, we can obtain s_i using

$$\frac{\sigma_i^2}{\mu_i^2} = CV^2 = (e^{s_i^2} - 1) \qquad \Rightarrow \qquad s_i^2 = \log(1 + CV^2) \tag{3.6}$$

We calculated the means, m_i, and variances, s_i, of the lognormal target protein distributions using a typical CV value of 0.3 (Milo, 2013).

3.4. Modelling Fluorescence Emission

In this section, we describe the model of the emission process of the fluorochromes in cells that are positive for the conjugated protein. Firstly, we calculated the duration of excitation as a function of cell radius using the blue laser and the velocity of fluid flow. Secondly, we derived the expressions for the absorbed energy for cells with one or more fluorochromes. Using the absorbed energy, we determined the number of absorbed photons and then the number of emitted photons via the quantum efficiency of the corresponding fluorochrome. Lastly, we drew the corresponding amount of photons from each fluorochrome's emission spectrum that we treated as a probability density function and directed a fixed fraction of the emitted photons towards the optic channel. The details of each step are provided below.

3.4.1. Excitation Duration and Illuminated Volume

In this section, we present the expressions for laser exposure time for a spherical model cell with a specific radius. We used the 488 nm blue laser that has an elliptical output with 9μm height and 65μm width (BD FACSCanto, 2006). We calculated the excitation duration as a function of cell radius and the speed of fluid flow through the interrogation point.

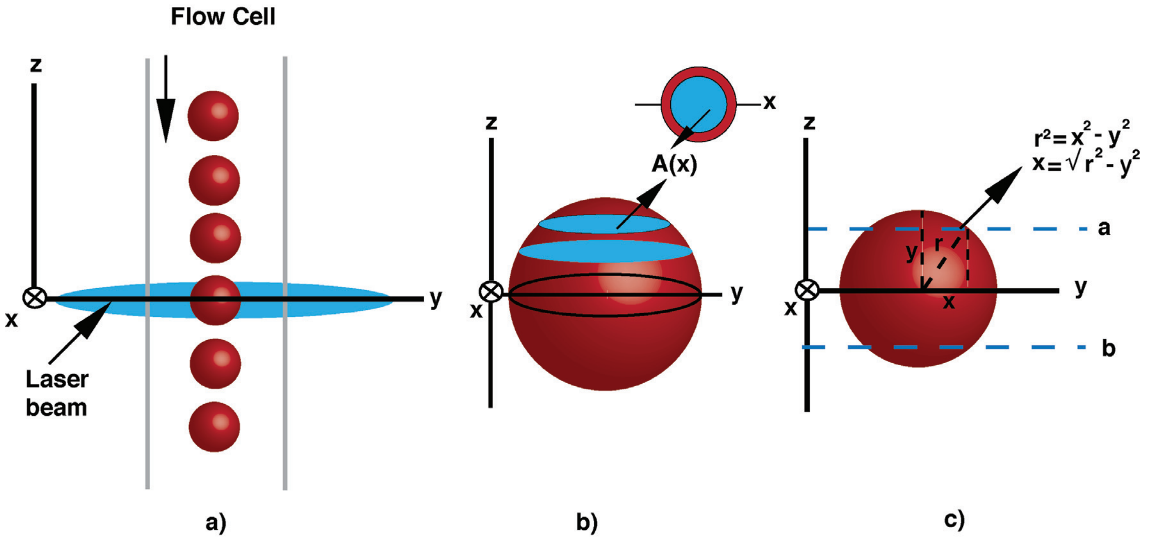

Figure 3.4. Illustration of the illuminated region under the laser beam

We illustrated spherical cells under laser illumination in Fig.3.4 where (a) is an illustration of the laser illumination of the cells at the interrogation point, and (b) shows a scaled cell for two distinct cross-section areas as it passes through the laser beam. If we look at the cell from the top, it looks like a disk as shown at the top of (b). Finally, (c) is an illustration of the illuminated volume of the cell as shown from the front. In our model, the diameters of the lymphocytes are smaller than the height of laser output. In this case, the illuminated volume of a cell is generally proportional to the square of the cell diameter (Peeters et al., 1989).

To calculate the illuminated volume of each cell at a given time instant as it passes through the laser beam, we firstly assumed that the cells are spherical as shown in Fig.3.4. Secondly, we also assumed that the laser power is uniform across the beam cross-section. When the laser hits the cells, it illuminates a band of width 9μm. We calculated the illuminated volume of the cell as a function of position z shown in Figure 3.5 along the vertical axis using expression below, where a and b denote the points where the laser cross-section cuts the spherical cell:

$$V(a,b) = \int_a^b \pi(r^2 - z^2)dz \tag{3.7}$$

The illuminated volume depends on a and b that vary with time. After calculating the

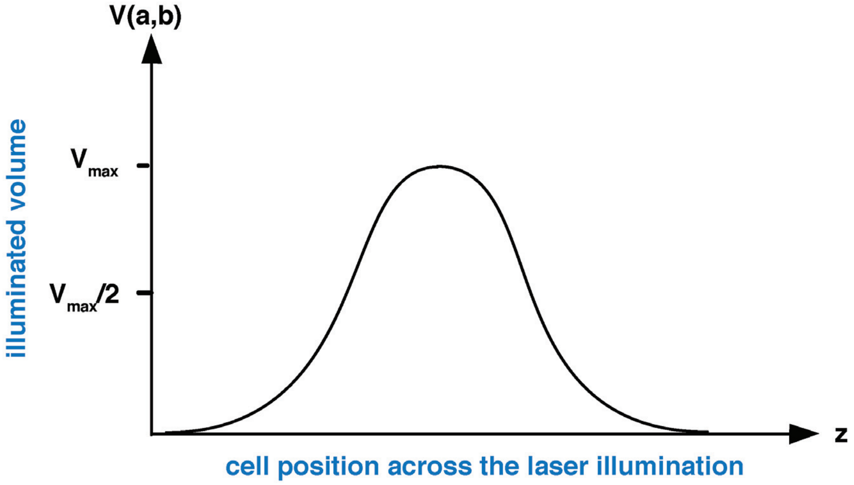

Figure 3.5. Illuminated volume of cell according to cell position un

illuminated volume in terms of the position of cell, we determined the excitation duration of each cell. We used the velocity of fluid flow given as 10m/s (Shapiro, 2005). The illumination for each cell time is then given by

$$t = \frac{X}{\vartheta_{flow}} \tag{3.8}$$

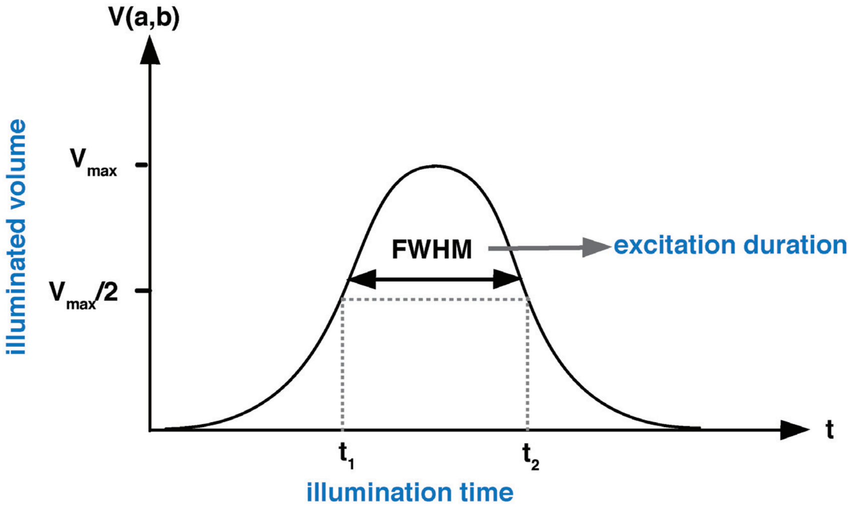

Figure 3.6. Schematic of full width at half maximum value

where X denotes position of the cell across the laser beam, ϑ_{flow} is the velocity of fluid flow. Inserting the actual value of fluid velocity Equation 3.8, we obtained the time interval that the laser illuminates the cell for each model cell. We used the full width at half maximum (FWHM) value of the graph of the illuminated volume as a fraction of time as the excitation duration of the cell in Figure 3.6.

3.4.2. Energy Absorbance for a Single Fluorophore

In this part of the study, we determined the amount of laser light absorbance for each cell. Absorbance is firstly related to the intensity of the light source. The absorptivity of a molecule is determined by Beer-Lambert law that relates absorbance to path length, concentration and extinction coefficient of the fluorescent molecule (Shapiro, 2005). The absorption path length is related to the radius of the cell. The concentration is the amount of the fluorescent molecule per unit volume. In this section, we describe the absorbance process when only one fluorescent marker is present in a specific concentration. The absorbance of a fluorochrome is given by

$$A = \ln \frac{I}{I_0} = \varepsilon c l \tag{3.9}$$

where A is the absorbance without units, c is molar concentration in moles per liter, ε is the extinction coefficient or molar absorptivity in litre per mole per centimetre defined as the capacity of light absorbance at a certain wavelength, and l is the optical path length in centimetres. Absorbance can be expressed in terms of transmittance, defined as the ratio of the intensity of transmitted light to the intensity of incident light as

$$T = \frac{I}{I_0}. \tag{3.10}$$

Transmittance is therefore related to absorbance in Equation 3.9 via

$$A = \ln T. \tag{3.11}$$

Accordingly, I_0 is the intensity of incident light and I is the intensity of light that is transmitted across the absorbing medium. The extinction coefficient ε is an intrinsic value and it changes for every fluorescent molecule. The spectrum of the extinction coefficients is related to the excitation spectrum as the absorptivity curve is the mirror image of the excitation curve. The specifications of fluorescent dyes are typically given as the percent transmittance with respect to wavelength.

We adopted the Beer-Lambert Law in Equation 3.9 for a fluorophore-conjugated cell in the flow cell of a flow cytometer. In the adopted formula, we assumed that r is the radius of the cell and c is the target protein concentration that is uniformly distributed across the cell volume. Then, light absorbance of a point (x, y) in the cell cross-sectional plane under laser illumination is equal to

$$A(x, y) = \varepsilon(\lambda) L(x, y) c \tag{3.12}$$

where $L(x, y)$ given by

$$L(x, y) = \begin{cases} 2\sqrt{r^2 - x^2 - y^2} & \text{if } x^2 + y^2 \leq r^2 \\ 0 & \text{otherwise} \end{cases} \tag{3.13}$$

denotes the laser path length entering the cell at point (x, y) in the laser beam cross-section, and λ is the wavelength of the excitation light source. This expression is illustrated in the following figure.

The laser beam illuminates each point (x, y) in the cross-section with power P during excitation time described in subsection 3.4.1. Note that extinction coefficients are commonly given at the maximum absorptivity value. For this reason, to find the extinction coefficient of each fluorophore at the wavelength of the laser, we normalized the emission spectrum of each fluorophore using the maximum absorptivity value of fluorophores.

To calculate the concentration of each fluorescent marker, we used the expression

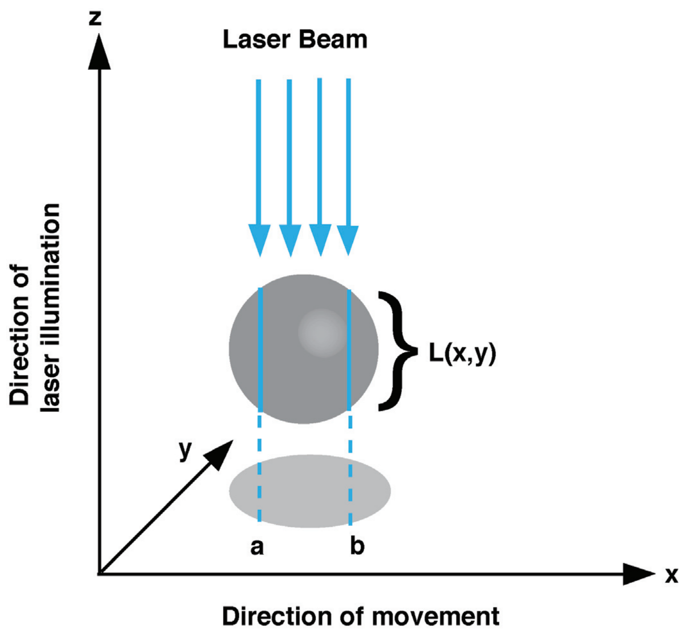

Figure 3.7. Laser illumination in the cross-section of the cell

$$c_{dye} = \frac{N_{protein}}{\frac{4}{3}\pi r^3 N_A} \tag{3.14}$$

where c_{dye} indicates the biomarker concentration per cell in moles, $N_{protein}$ describes the number of target proteins in the cell and N_A is the Avogadro number.

Next, we calculated the amount of the laser power falling on the cell per unit area in the beam cross-section using

$$P = \frac{P_{laser}}{\pi r_a r_b} \tag{3.15}$$

where r_a is the small radius and r_b is the large radius of the blue laser beam cross section. At the interrogation point, all cells are exposed to this radiant energy, and it causes a radiant flux on the cell defined in watts per unit time (Shapiro, 2005). We obtained the energy falling on the cell for Δt seconds per unit area as

$$E_0 = P\Delta t. \tag{3.16}$$

Note that Δt is constant and equals the duration of time for which each point (x, y) at the cell cross-section is illuminated by the laser.

Using the concentration data, the laser path-length, and extinction coefficients of the fluorophores, we calculated the transmittance intensity via

$$I(x, y) = I_0 10^{-\varepsilon(\lambda)L(x,y)c_{dye}} \tag{3.17}$$

Rewriting this equation in terms of the energies, we obtained

$$E(x,y) = E_0(1 - 10^{-\varepsilon(\lambda)L(x,y)c_{dye}}) \tag{3.18}$$

where $E(x,y)$ denotes the absorbed energy at a point (x,y) in the cell cross-section.

Integrating the absorbed energy $E(x,y)$ at a point x,y across the cell cross-section, we finally obtained total absorbed energy as

$$E = \iint_{x^2+y^2 \leq r^2} E(x,y)dxdy \tag{3.19}$$

From total absorbed energy, we calculated the number of absorbed photons using

$$N_{dye} = \frac{E}{h\nu} \tag{3.20}$$

where ν is the frequency of excitation light source and h is Planck's constant.

3.4.3. Energy Absorbance for Multiple Fluorophores

For the case where multiple fluorophores are present in a cell, we firstly adopted the absorbance of a fluorophore in Equation 3.9 for multiple fluorophores as;

$$A_{total}(x,y) = \sum_{i=1}^{n} A_i(x,y) = \sum_{i=1}^{n} \varepsilon_i(\lambda)L(x,y)c_i \tag{3.21}$$

where $A_{total}(x,y)$ denotes total absorbance while $A_i(x,y)$ is the fluorochrome-specific absorbance indexed by i. Substituting $A_{total}(x,y)$ with $A(x,y)$ into Equation 3.18, we obtained the total absorbed energy by all fluorochromes at the point (x,y) as;

$$E_{total}(x,y) = E_0(1 - 10^{-A_{total}(x,y)}) \tag{3.22}$$

In order to determine how much of $E_{total}(x,y)$ is absorbed by the different fluorochromes, we calculated the energy to be absorbed by the i$^{\text{th}}$fluorochrome in solitude by

$$\tilde{E}_i(x,y) = E_0(1 - 10^{-A_i(x,y)}) \tag{3.23}$$

and calculated the total via

$$\tilde{E}(x,y) = \sum_{i=1}^{n} \tilde{E}_i(x,y). \tag{3.24}$$

Assuming that $E_{total}(x,y)$ would be distributed proportionally with among the different fluorochromes, we determined the absorbed energies by each fluorophore using

$$E_i(x,y) = \tilde{E}_i(x,y)\frac{E_{total}(x,y)}{\tilde{E}(x,y)}. \tag{3.25}$$

Substituting $E_i(x,y)$ with $E(x,y)$ into Equation 3.19, we obtained the total absorbed energy for fluorophore i as;

$$E_i = \iint_{x^2+y^2 \leq r^2} E_i(x,y)dxdy \tag{3.26}$$

Finally, we can express the fluorochrome-specific absorbed photons N_i in terms of the absorbed energy and the energy of light source in the following equation as;

$$N_i = \frac{E_i}{h\nu} \tag{3.27}$$

where ν is again the frequency of the excitation light source.

3.4.4. Emission

We determined the number of emitted photons from each fluorophore using their quantum efficiency values. The quantum efficiency is defined as the ratio of the number of emitted photons to absorbed photons:

$$q = \frac{N^e_{dye}}{N^a_{dye}} \tag{3.28}$$

This means that the number of emitted photons by each fluorochrome can be calculated using

$$N^e_{dye_i} = N^a_{dye_i} q_i \tag{3.29}$$

where $N^e_{dye_i}$ and $N^a_{dye_i}$ denote the number of emitted and absorbed photons respectively and for each fluorochrome indexed by i, with q_i indicating the corresponding quantum efficiency.

In our implementation, i represents FITC and PE fluorophores. Therefore, we derived absorbance and emission expressing that are positive for FITC-conjugated proteins, PE-conjugated proteins, and both (Figure 3.8).

On a final note, a fraction of the emitted photons from each fluorochrome is routed towards the detectors according to the specifications of the optical components as well as their geometry. Unfortunately, no details are provided for this fraction for the BD FACSCanto. Therefore, based on the aperture of the optic channel at the flow chamber geometries, we assumed that only ten percent of the number of emitted photons entering the optic channel. We treated each fluorochrome's emission spectrum as a probability density function to generate the emitted photons.

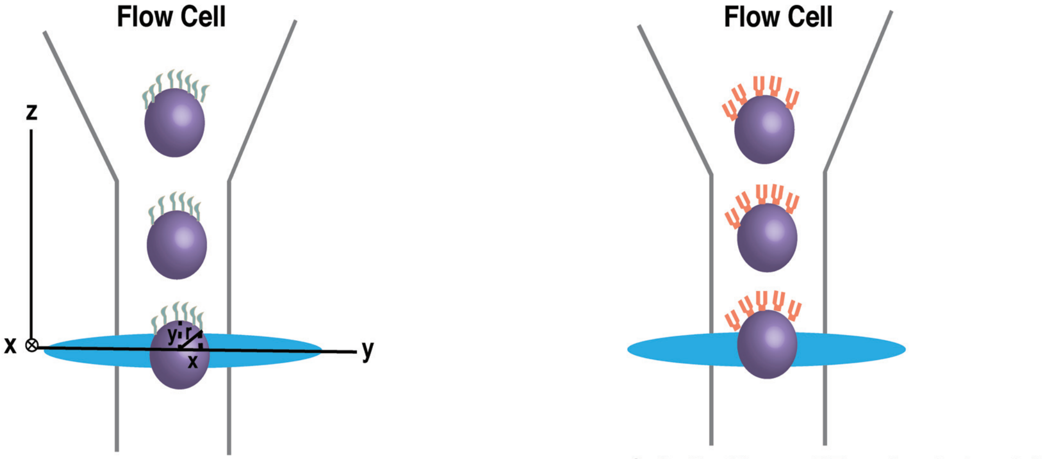

a) Cells Position for FITC-conjugated proteins

b) Cells Position for PE-conjugated proteins

Absorbed energy for FITC:
$E_{FITC}(x,y)=E_0(1-10^{-A_{FITC}(x,y)})$

Total absorbed energy for FITC:
$E_{FITC}=\iint E_{FITC}(x,y)dxdy$
Emitted Photon Numbers:
$N_{FITC}=(E_{FITC}/hv)q_{FITC}$

Absorbed energy for PE:
$E_{PE}(x,y)=E_0(1-10^{-A_{PE}(x,y)})$

Total absorbed energy for PE:
$E_{PE}=\iint E_{PE}(x,y)dxdy$
$N_{PE}=(E_{PE}/hv)q_{PE}$

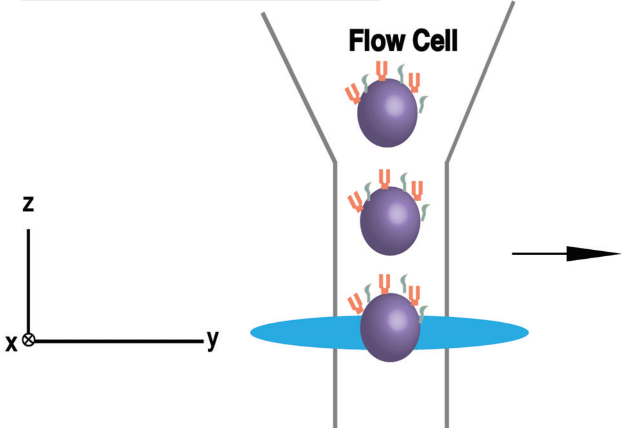

c) Cells Position for both FITC and PE-conjugated proteins

Absorbed Energies:

$\tilde{E}_{FITC}(x,y)=E_0(1-10^{-A_{FITC}(x,y)})$

$\tilde{E}_{PE}(x,y)=E_0(1-10^{-A_{PE}(x,y)})$

$E(x,y)=E_0(1-10^{-A_{PE+FITC}(x,y)})$

$\tilde{E}(x,y)=E_{PE}(x,y)+E_{FITC}(x,y)$

$E_{FITC}(x,y)=\tilde{E}_{FITC}(x,y)(E(x,y)/\tilde{E}(x,y))$

$E_{PE}(x,y)=\tilde{E}_{PE}(x,y)(E(x,y)/\tilde{E}(x,y))$

Total absorbed energies:

$E_{FITC}=\iint E_{FITC}(x,y)dxdy$, $E_{PE}=\iint E_{PE}(x,y)dxdy$

Emitted Photon Numbers:

$N_{FITC}=(E_{FITC}/hv)q_{FITC}$; $N_{PE}=(E_{PE}/hv)q_{PE}$

Figure 3.8. Summary of energy absorbance equations for cells that are positive for only FITC, only PE and FITC and PE conjugated cells

3.4.5. Modelling The Optical Channel

In this section, we present the model of the optical channel used to determine the distribution of all photons emitted by the fluorochromes over all detectors. The model is based on the octagon detector array that directs emissions from each fluorochrome to the appropriate detectors. Table 3.1 details the bandpass filters and longpass filters of the octagon and trigon detector arrays. Each detector is designed to detect emissions from a specific fluorophore. The longpass filters or dichroic mirrors at the octagon detector array selectively reflect and transmit the light in accordance with their cut-off frequencies. Likewise, the bandpass filters selectively absorb and transmit the light. Appendix A includes the characteristics of each filter at the octagon detector array shown in Table 3.1. These characteristics are provided in the form of transmission rates across their wavelength range that we treated as transmission probabilities.

Table 3.1. Filters and Dyes in the Octagon Detector Array

Source: (BD FACSCanto, 2006)

Detector Array (Laser)	**PMT Position**	**LP Mirror**	**BP Filter and LP Mirror**	**Intented Dye**
Octagon (488-nm blue laser)	A	735	780/60	PE-Cy7
	B	655	670 LP	PerCP-Cy5.5, PerCP
	C	556	585/42	PE
	D	502	530/30	FITC
	E	blank optical holder	488/10	Side Scatter (SSC)
	F	blank optical holder	blank optical holder	-
	G	blank optical holder	blank optical holder	-
	H	blank optical holder	blank optical holder	-
Trigon (633-nm red laser)	A	735	780/60	APC-Cy7
	B	blank	660/20	APC

In other words, the transmission rate curves represent the probability with which a photon with wavelength λ can pass through or be detected or absorbed in the filters, to contribute to a latent detector of photon loss. Let $T_X^{lp}(\lambda)$ be the transmission percentage of a longpass filter and $T_X^{bp}(\lambda)$ be the transmission percentage of a bandpass filter at wavelength λ normalized to the range [0, 1], where X is the label of a detector at the octagon detector array with $X \in \{A, B, C, D, E, F, G, H\}$. The following equations represent the probabilities with which a photon with wavelength λ will fall on each detector in the octagon detector array configuration:

$$\begin{aligned}
&P_A(\lambda) = T_A^{lp}(\lambda)T_A^{bp}(\lambda)\\
&P_B(\lambda) = (1 - T_A^{lp}(\lambda))T_B^{lp^1}(\lambda)T_B^{lp^2}(\lambda)\\
&P_C(\lambda) = (1 - T_A^{lp}(\lambda))(1 - T_B^{lp}(\lambda))T_C^{lp}(\lambda)T_C^{bp}(\lambda)\\
&P_D(\lambda) = (1 - T_A^{lp}(\lambda))(1 - T_B^{lp}(\lambda))(1 - T_C^{lp}(\lambda))T_D^{lp}(\lambda)T_D^{bp}(\lambda)\\
&P_E(\lambda) = (1 - T_A^{lp}(\lambda))(1 - T_B^{lp}(\lambda))(1 - T_C^{lp}(\lambda))(1 - T_D^{lp}(\lambda))T_E^{lp}(\lambda)T_E^{bp}(\lambda)\\
&P_F(\lambda) = (1 - T_A^{lp}(\lambda))(1 - T_B^{lp}(\lambda))(1 - T_C^{lp}(\lambda))(1 - T_D^{lp}(\lambda))(1 - T_E^{lp}(\lambda))\\
&T_F^{lp}(\lambda)T_F^{bp}(\lambda)\\
&P_G(\lambda) = (1 - T_A^{lp}(\lambda))(1 - T_B^{lp}(\lambda))(1 - T_C^{lp}(\lambda))(1 - T_D^{lp}(\lambda))(1 - T_E^{lp}(\lambda))\\
&(1 - T_F^{lp}(\lambda))T_G^{lp}(\lambda)T_G^{bp}(\lambda)\\
&P_H(\lambda) = (1 - T_A^{lp}(\lambda))(1 - T_B^{lp}(\lambda))(1 - T_C^{lp}(\lambda))(1 - T_D^{lp}(\lambda))(1 - T_E^{lp}(\lambda))\\
&(1 - T_F^{lp}(\lambda))(1 - T_G^{lp}(\lambda))T_H^{lp}(\lambda)T_H^{bp}(\lambda)\\
&P_L(\lambda) = 1 - (P_A(\lambda) + P_B(\lambda) + P_C(\lambda) + P_D(\lambda)) + P_E(\lambda) + P_F(\lambda) + P_G(\lambda) + P_H(\lambda))
\end{aligned} \tag{3.30}$$

Note that the detector model denotes a latent detector for lost photons due to bandpass filters and blank optical holders. All events assumed to be independent from each other. The details of these calculations are provided below.

Detector A: The emitted light entering from the optic channel is firstly met with detector A comprised of 735 nm longpass filter and 780/60 nm bandpass filter (Table 3.1). Generally, the 735 nm LP filter only permits to pass photons with wavelengths longer than 735 nm and reflects the photons that have wavelengths lower than 735 nm through the transmission rates are not exact. The transmitted light is directed onto 780/60 nm bandpass filter that permits to pass the wavelengths between 750 nm and 810 nm while it blocks the other wavelengths.

Note that $T_{735}^{lp}(\lambda)$ represents the transmission probability in terms of λ for 735 nm LP and $T_{780/60}^{bp}(\lambda)$ represents the transmission probability at wavelength λ for 780/60 nm BP filter. The probability with which a photon with wavelength λ falls at the detector A is then given by

$$P_A(\lambda) = T_{735}^{lp}(\lambda)T_{780/60}^{bp}(\lambda). \tag{3.31}$$

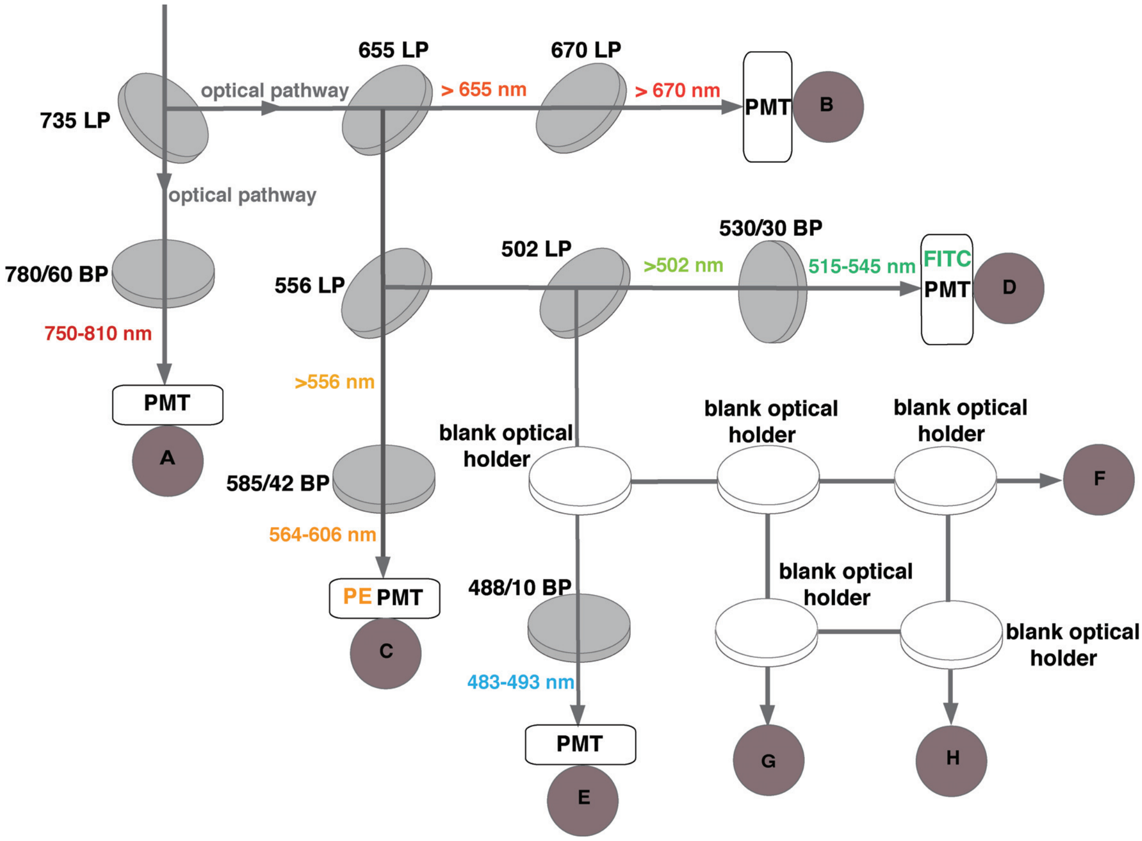

Figure 3.9. Schematic overview of the octagon detector array

Detector B: Detector B is designed using 655 nm LP and 670 nm LP filters. The 735 nm LP filter reflects the photons, that their wavelengths are lower than 735 nm, onto 655 nm LP filter. It transmits the photons with wavelengths longer than 655 nm while it reflects the photons with wavelengths lower than 655 nm. In the same way, 670 nm LP filter behind the 655 nm LP filter transmits the photons longer than 670 nm and reflects other photons.

Note that $T^{lp}_{655}(\lambda)$ and $T^{lp}_{670}(\lambda)$ describe the transmission probabilities of the filters, respectively. Given that the probability of a photon with wavelength λ reaching the B detector slot is equal to $1 - T^{lp}_{A}(\lambda)$, the total probability with which it falls at the detector B is given by

$$P_B(\lambda) = (1 - T^{lp}_{735}(\lambda))T^{lp}_{655}(\lambda)T^{lp}_{670}(\lambda). \tag{3.32}$$

Detector C: Detector C is equipped with 556 nm LP filter and 585/42 nm BP filter. 655 nm LP filter reflects photons with wavelengths smaller than 655 nm to 556 nm LP that transmits the photons longer than 556 nm. Then, 585/42 nm BP filter permits to pass the photons with wavelengths between 564 nm to 606 nm while it blocks the other photons. Note that the probability of a photon with wavelength λ hitting the C detector slot is equal to $(1-T_A^{lp}(\lambda))(1-T_B^{lp}(\lambda))$, the total probability with which the photon falls at the detector C is calculated via

$$P_C(\lambda) = (1 - T_{735}^{lp}(\lambda))(1 - T_{655}^{lp}(\lambda))T_{556}^{lp}(\lambda)T_{585/42}^{bp}(\lambda). \tag{3.33}$$

Detector D: Detector is designed using 502 nm LP filter and 530/30 nm bandpass filter. 556 nm LP filter reflects the photons, that their wavelengths are smaller than 556 nm, onto 502 nm LP filter. It directs the photons longer than 502 nm onto 530/30 nm BP filter while it reflects the photons with wavelengths lower than 502 nm. 530/30 nm BP filter permits to transmit the photons with wavelengths between 515 nm and 545 nm while it is blocks the other photons. Given that the probability of a photon with wavelength λ hitting the D detector slot is equal to $(1 - T_A^{lp}(\lambda))(1 - T_B^{lp}(\lambda))(1 - T_C^{lp}(\lambda))$, the total probability with which the photon falls at the detector D is given by

$$P_D(\lambda) = (1 - T_{735}^{lp}(\lambda))(1 - T_{655}^{lp}(\lambda))(1 - T_{556}^{lp}(\lambda))T_{502}^{lp}(\lambda)T_{530/30}^{bp}(\lambda). \tag{3.34}$$

Detector E: Detector E is equipped with a blank optical holder and 488/10 nm bandpass filter. 502 nm LP filter reflects the photons with wavelengths smaller than 502 nm onto the blank optical holder, while it transmits the others to 488/10 nm BP filter that permits to pass the photons with wavelengths between 483 nm and 493 nm. Given that the probability of a photon with wavelength λ hitting the E detector slot is equal to $(1 - T_A^{lp}(\lambda))(1 - T_B^{lp}(\lambda))(1 - T_C^{lp}(\lambda))(1 - T_D^{lp}(\lambda))$, the total probability with which the photon falls at the detector E is calculated using the following equation;

$$P_E(\lambda) = (1 - T_{735}^{lp}(\lambda))(1 - T_{655}^{lp}(\lambda))(1 - T_{556}^{lp}(\lambda))(1 - T_{502}^{lp}(\lambda))T_{488/10}^{bp}(\lambda). \tag{3.35}$$

Other Detectors: Detectors F, G, and H are comprised of the blank optical holders. E detector does not contain any dichroic mirror. For this reason, the E detector does not reflect the light onto F detector. It causes that no light is routed to the F detector and then remaining G, and H detectors from detector E. In Equation 3.36, the probability of a photon with wavelength λ hitting the F detector slot is equal to $(1 - T_A^{lp}(\lambda))(1 - T_B^{lp}(\lambda))(1 - T_C^{lp}(\lambda))(1 - T_D^{lp}(\lambda))(1 - T_E^{lp}(\lambda)$, where $(1 - T_E^{lp}(\lambda))$ that equals to zero. The total probability with which the photon falls at the detector F is calculated using the following equation;

$$P_F(\lambda) = (1-T_{735}^{lp}(\lambda))(1-T_{655}^{lp}(\lambda))(1-T_{556}^{lp}(\lambda))(1-T_{502}^{lp}(\lambda))(1-T_E^{lp}(\lambda))T_F^{lp}(\lambda)T_F^{bp}(\lambda) \tag{3.36}$$

Note that the light intensity of the blank optical holders equal zero at the detectors G and H. Since the minute amount of light that reaches the detector F is absorbed and otherwise lost.

Latent Detector for Lost Photons We determined the amount of lost light at all detectors of the octagon detector array as the sum of the absorbed photons. The probability $P_L(\lambda)$ with which a photon with wavelength λ will be lost is then given by

$$L_X(\lambda) = 1 - \sum_{X \in \{A,B,C,D,E,F,G,H\}} P_X(\lambda) \tag{3.37}$$

where X denotes the label of actual detectors at the octagon detector array.

3.5. Photon Distributions across Detectors

In this section, we present the model of stochastic photon counting across the optic channel. The emitted photons are randomly distributed among the detectors according to the detector probability for the specific wavelength. To this end, for a photon with wavelength λ, we created the probability intervals of each detector in terms of the probability of receiving photons as shown in following Fig.3.10. The intervals associated with detectors A, B, C, D, E, and L are given as[1]:

$I_A = [0, P_a(\lambda));$

$I_B = [P_a(\lambda), P_a(\lambda) + P_b(\lambda));$

$I_C = [P_a(\lambda) + P_b(\lambda), P_a(\lambda) + P_b(\lambda) + P_c(\lambda));$

$I_D = [P_a(\lambda) + P_b(\lambda) + P_c(\lambda), P_a(\lambda) + P_b(\lambda) + P_c(\lambda) + P_d(\lambda));$

$I_E = [P_a(\lambda) + P_b(\lambda) + P_c(\lambda) + P_d(\lambda), P_a(\lambda) + P_b(\lambda) + P_c(\lambda) + P_d(\lambda)) + P_e(\lambda));$

$I_L = [P_a(\lambda) + P_b(\lambda) + P_c(\lambda) + P_d(\lambda)) + P_e(\lambda), P_a(\lambda) + P_b(\lambda) + P_c(\lambda) + P_d(\lambda)) + P_e(\lambda), 1)$

Then, for each photon, we generated a random value **U** from a uniform distribution over the unit interval, and directed the photon towards are of the detectors using the rule 3.10.

---

[1] The intervals for F, G, H detectors have zero length because blank optical holders blocks all photons and there is no photon transmission.

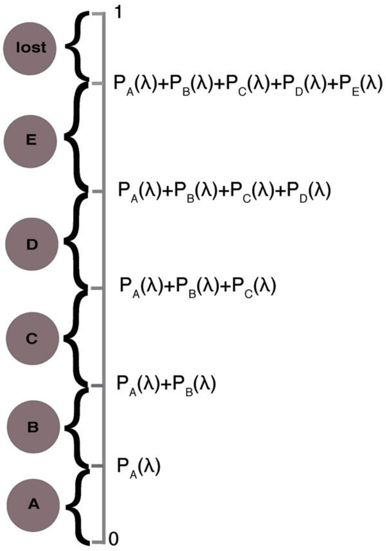

Figure 3.10. Probability interval of each detector at the octagon detector array

$$\mathbf{X} = \begin{cases} \text{photon falls on A detector} & \text{if } \mathrm{U}\epsilon I_a \\ \text{photon falls on B detector} & \text{if } \mathrm{U}\epsilon I_b \\ \text{photon falls on C detector} & \text{if } \mathrm{U}\epsilon I_c \\ \text{photon falls on D detector} & \text{if } \mathrm{U}\epsilon I_d \\ \text{photon falls on E detector} & \text{if } \mathrm{U}\epsilon I_e \\ \text{the photon is lost} & \text{otherwise} \end{cases} \tag{3.38}$$

All photons falling at a given detector are then routed to the corresponding photomultiplier tube behind the detector.

3.5.1. Photomultiplier Tube's Response at the Detectors

This subsection contains the calculation of the photomultiplier tube (PMT) response to the received photons in terms of the optical fluxes and the currents. Photomultiplier tubes convert the optical signal to an electrical signal. We used Hamamatsu R928 PMT to determine the PMT response. Note that each detector in the octagon detector array is equipped with identical photomultiplier tubes that are placed behind each detector's bandpass filter. The photons hit the surface of the photocathode, resulting in photoelectric emission as photoelectrons (Fig.2.10). Photoelectric emission continues as long as there

Figure 3.11. R928,R955 Photomultiplier Tube

Source: (Hamamatsu, 2006b)

is optical photon flux to the photomultiplier tube.

We obtained specifications of R928, R955 PMT from Hamamatsu Photonics Inc. (Arzbergerstr.10, D-82211 Herrsching am Ammersee, Germany) comprising of cathode radiant sensitivity values, quantum efficiency of cathode in terms of the wavelength and gain values of the electron multipliers for different supplied voltages. Cathode radiant sensitivity curves contain radiant sensitivity values for varying wavelengths that are listed in Appendix A. In the first step, we determined the energy of a photon received by the photocathode surface using

$$E_i = \frac{hc}{\lambda_i} \tag{3.39}$$

where λ_i denotes wavelength of the i'th photon, h is Planck's constant and c is the velocity of light. Second, we calculated the total energy in terms of all received photons to the photocathode surface as:

$$E_{total} = \sum_{i=1}^{n} E_i \tag{3.40}$$

where n is the number of received photons. Total photon flux at the photocathode surface is calculated using the ratio of the total energy to excitation duration of the cell as determined in subsection 3.4.1. The equation that describes the photon flux is thus given by

$$\Phi_e = \frac{E_{total}}{\Delta t} \tag{3.41}$$

where Δt is the excitation duration of a cell. Then, we calculated the cathode current, I_k, inserting Φ_e to Equation 2.2 as;

$$S_k = \frac{I_k}{\Phi_e}$$

Note that, the radiant sensitivity of the photocathode, S_k, depends on the wavelength of incident light beam in Equation 2.2. This expression is defined for the monochromatic radiation. In the flow cytometry, the radiation receiving each photomultiplier tube is not monochromatic. But, this received radiation is selected by the different BP filters, placed in front of each PMT, in a very narrow wavelength range. Therefore, this selected wavelengths exist in a same colour of visible spectrum. For this reason, we used the radiant sensitivity value at the center of bandwidth value of the corresponding bandpass filter for each PMT to calculate the cathode current.

Finally, to calculate the anode current, we used the expression:

$$G = \frac{I_a}{I_k} \tag{3.42}$$

where I_a represents anode current and G denotes the gain of the photomultiplier tube with that varies the supplied voltage and the number of dynodes in PMT.

3.6. Pre-amplifier Circuit

In this section, we present a simulation of the pre-amplifier circuit for various combinations of amplitude and duration levels to obtain the peak, duration and integral of the resulting voltage pulse obtained as the detector output in flow cytometers.

We have determined the current output of the photomultiplier tubes for each cell in subsection 3.5.1. In flow cytometers, the output of photomultiplier tube connects to a pre-amplifier circuit that converts current to voltage. For this reason, we need a pre-amplifier circuit to determine voltage properties for each cell. In this work, we used a pre-amplifier circuit from Shapiro (Shapiro, 2005), shown in Fig.3.12. Then, we used LTspice© (1630 McCarthy Blvd. Milpitas, CA 95035-7417) to simulate the pre-amplifier circuit. The current outputs of the photomultiplier tubes are negative since the current's flow is from the cathode to the anode. In Figure 3.12, the first circuit is a current to voltage converter and 3 pF capacitor interferes with oscillation. The third circuit is an integrator that behaves as a low pass filter (Shapiro, 2005).

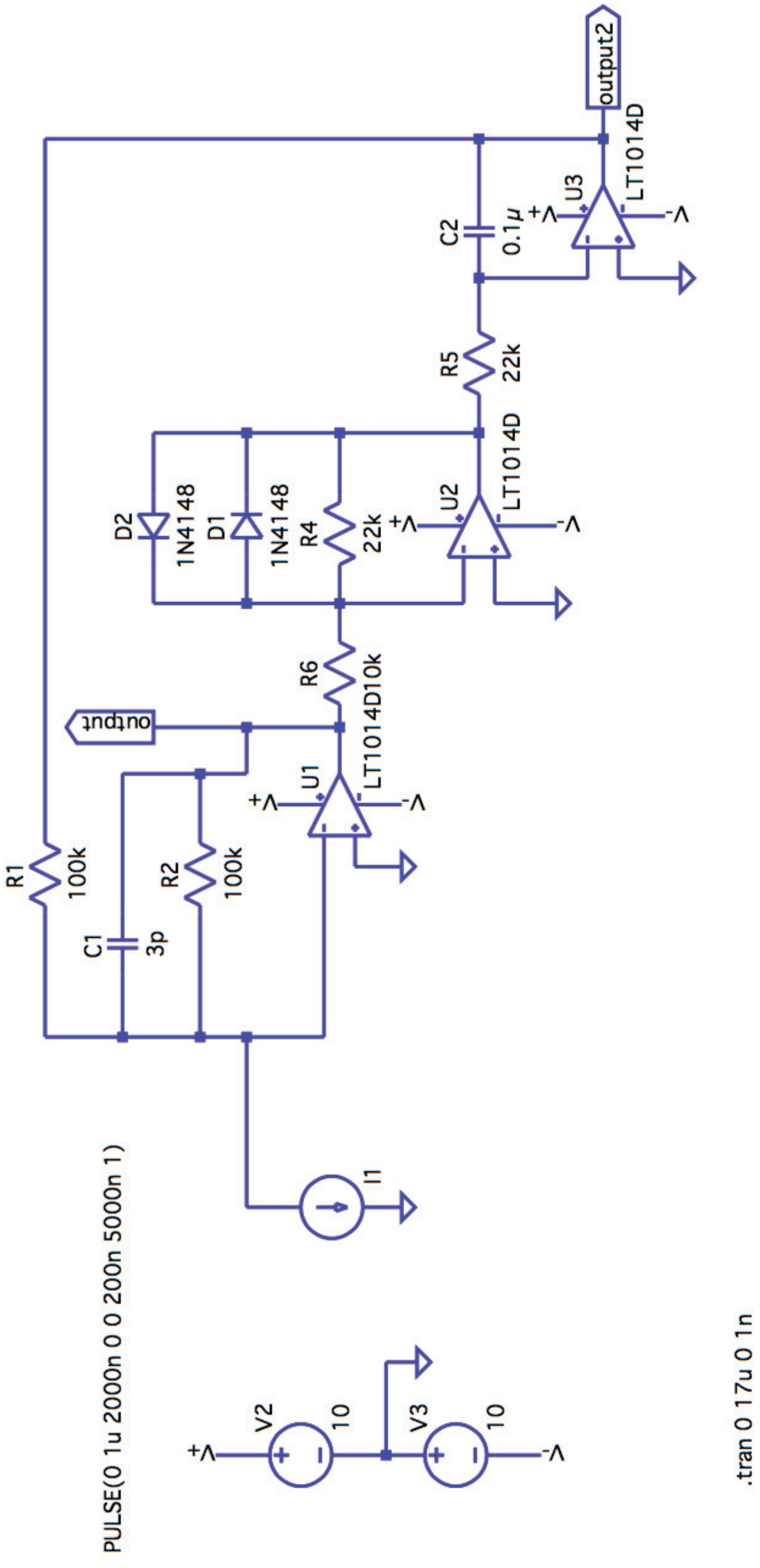

Figure 3.12. Preamplifier Circuit

Adapted From: (Shapiro, 2005)

We simulated the pre-amplifier circuit using various combinations of duration and current values to determine a reference voltage matrix. We took the output of the pre-amplifier circuit output probe in Fig.3.12. Then, we made a bi-linear interpolation to determine each detector response for the amplitude and duration values observed from a given cell at each detector.

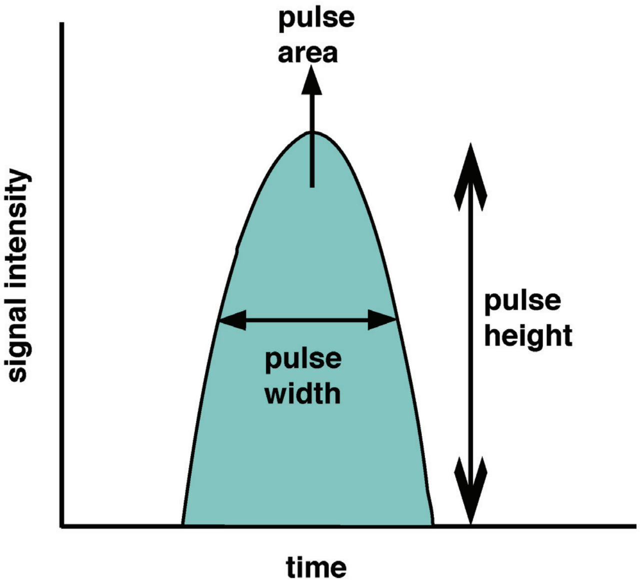

Figure 3.13. Pulse Measurement

Adapted From: (BD FACSCanto, 2006)

Generally, the width of a voltage pulse gives information about the granularity of cell while the height of a voltage pulse gives size information about the cell in the flow cytometers (Shapiro, 2005). In our simulations, we calculated the heights of the voltage pulses observed at the detectors for each specific fluorochrome-conjugated cell using bilinear interpolation. Thus, we determined the detector responses to the received photons in terms of the current, assuming uniform reception of the photons within the signal duration calculated by the duration of excitation.

CHAPTER 4

RESULTS

In this chapter, we present results for the methods described in Chapter 3, organized into five sections. Section 1 outlines results for modelling of cells, providing details of the size of model cells and the amounts of target proteins in positive cells. Section 2 and 3 describe the results for a single cell that is firstly positive for a FITC-conjugated target protein, and then positive for a PE-conjugated protein, including the size of the cell, the numbers of each target protein, total absorbed energy, wavelengths of the emitted photons from each fluorochrome, wavelengths of the received photons at different detectors, and finally, detector responses as voltage pulses obtained via bi-linear interpolation. Section 4 provides the above results again for a single cell that is positive simultaneously for FITC and PE-conjugated proteins. Section 5 explains results for a group of cells including ++, +- ,-+, and - - cell groups, their detector responses, and corrected responses after manual compensation.

4.1. Construction of Model Cells Profiles

We constructed model cell sizes using the range of the lymphocyte radii given in Chapter 3. We created a Gaussian distribution with a mean of 3.65×10^{-6}m and a variance of 1.6269×10^{-14}m^2 over a 0.95 confidence interval equalling [3.4μm, 3.9μm] shown in Figure 3.3. Then, we generated random values according to this Gaussian distribution so that each value represents the radius of a cell. A histogram of 1000 randomly generated radii is shown Figure. 4.1. Secondly, we generated samples of two lognormally distributed random variables, X_1 and X_2, to represent the number of two target proteins. We selected the actual average numbers of each protein for positive cells μ_1 and μ_2 as $(\mu_1, \mu_2) \sim \mathcal{N}(1.325\text{x}10^9,\ (1.913\text{x}10^8)^2)$, from which we determined the means m_1 and m_2 of the corresponding lognormal distributions.

The first lognormal distribution represents the number of FITC-conjugated target protein in the cells with a mean of m_1 equalling 1.3464×10^9 and a variance of s_1 equalling 1.6498×10^{17}, providing a CV value of 0.3017. The histogram of the number of the FITC-conjugated target proteins is given in Figure 4.2.

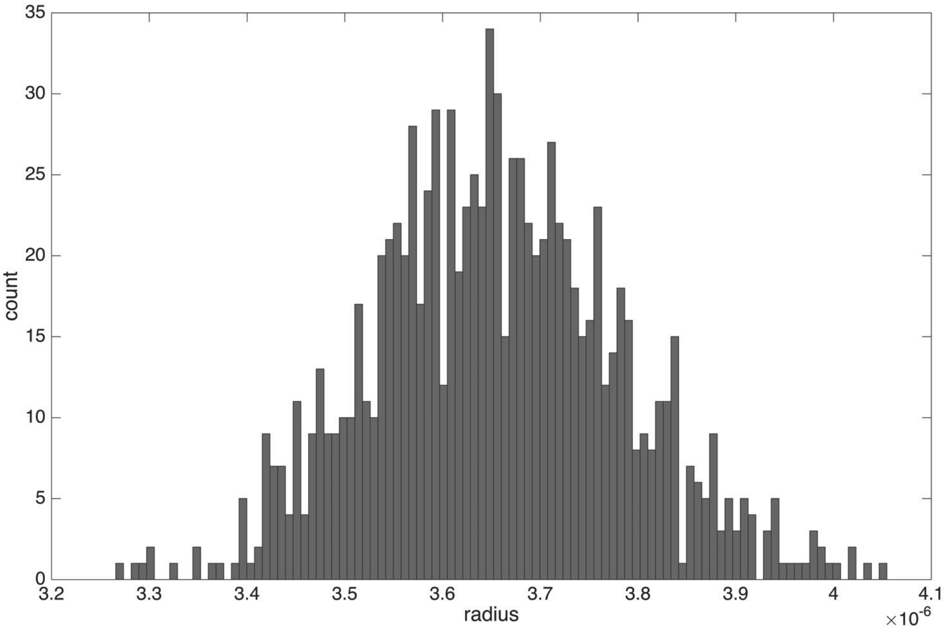

Figure 4.1. Radii histogram for 1000 model cells

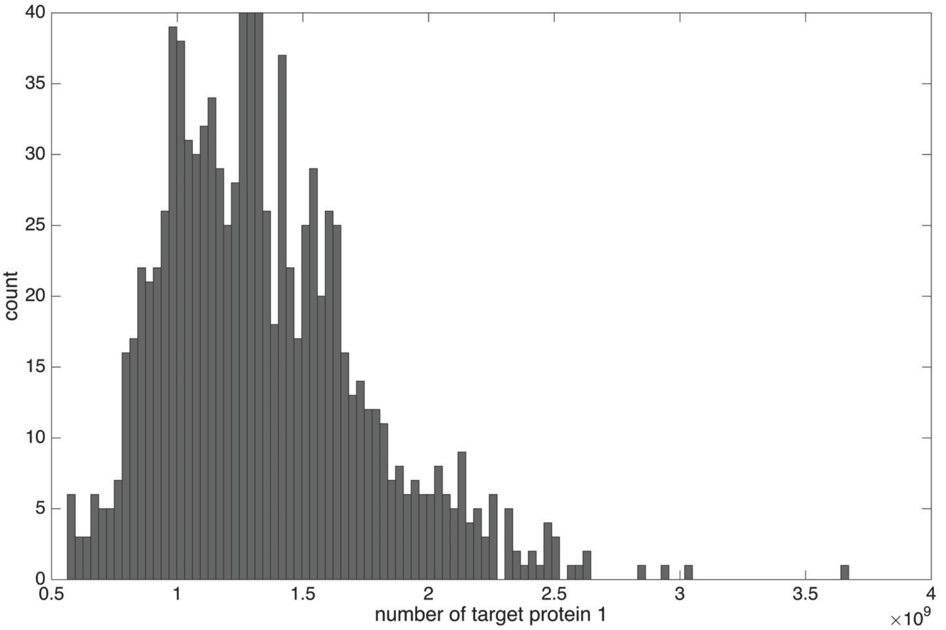

Figure 4.2. Histogram of FITC-conjugated protein numbers for 1000 model cells

Similarly, we created a second lognormal distribution representing the number of the PE-conjugated target protein in cells with a mean of equalling 1.3749×10^9 and a

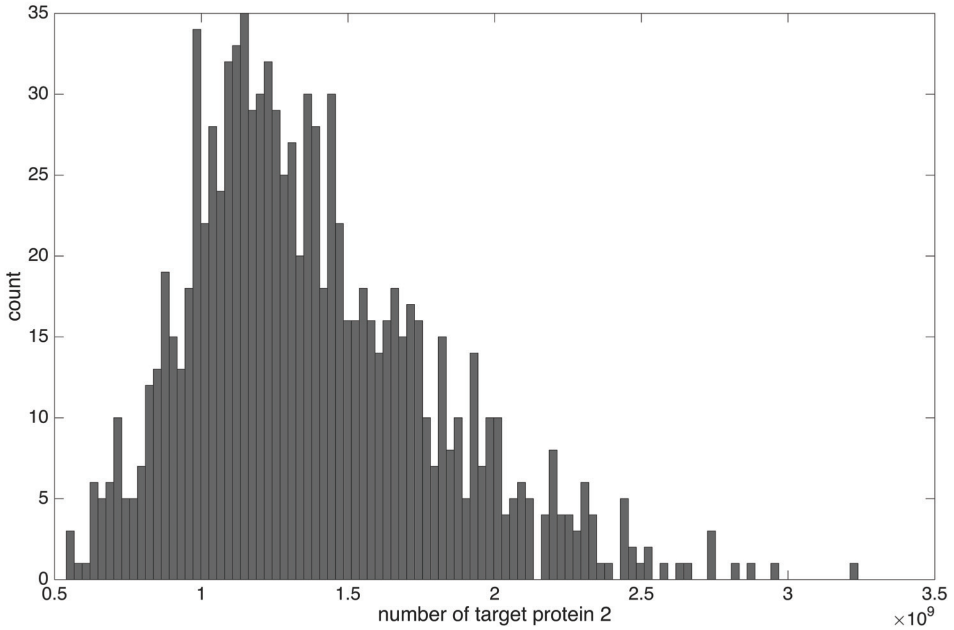

Figure 4.3. Histogram of PE-conjugated protein numbers for 1000 model cells

variance of s_1 equalling 1.7427×10^{17}, providing a CV value of 0.3036, as shown in Figure 4.3.

4.2. Results for a Single Cell with FITC-Conjugated Proteins

We simulated the fluorescence emission of a cell that is positive for FITC-conjugated proteins by selecting a radius value from these shown in Figure 4.1 at a protein number from these in Figure 4.2. Table 4.1 shows the radius of the cell and its corresponding number of target protein, as well as the total absorbed energy, denoted by E_{FITC}, calculated using Equation 3.26 for the given radius and the number of FITC target proteins as described below.

Table 4.1. FITC-conjugated cell

Radius	3.6078e-06m
Target Protein Number	1.3117e+09 copies
E_{FITC}	1.1704e-14 joules

To calculate the total absorbed energy, we firstly calculated the laser path length

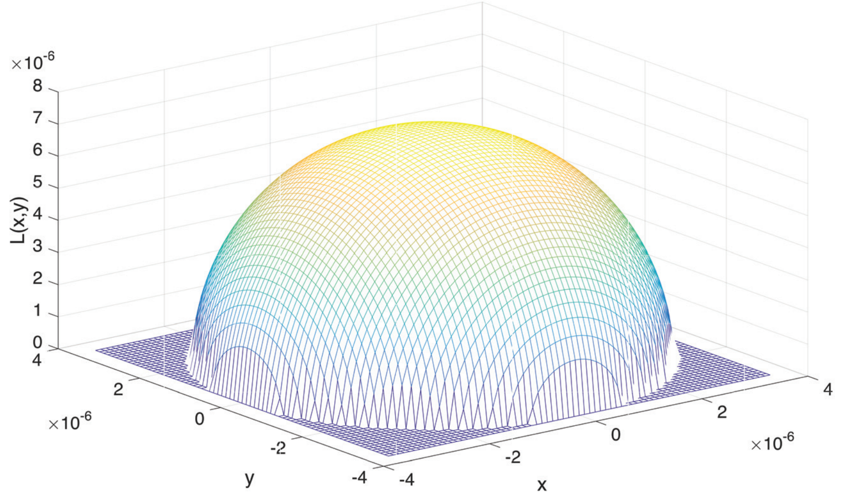

Figure 4.4. Laser path length entering the cell at point (x, y) in the cross section

entering given cell at point (x, y) in the cross section using Equation 3.13 where (x, y) varies according to the radius of the cell as between -3.6078×10^{-6}m and 3.6078×10^{-6}m with 1×10^{-7} increments (Figure 4.4). The absorbed energy at each point (x, y) is shown in Figure 4.5.

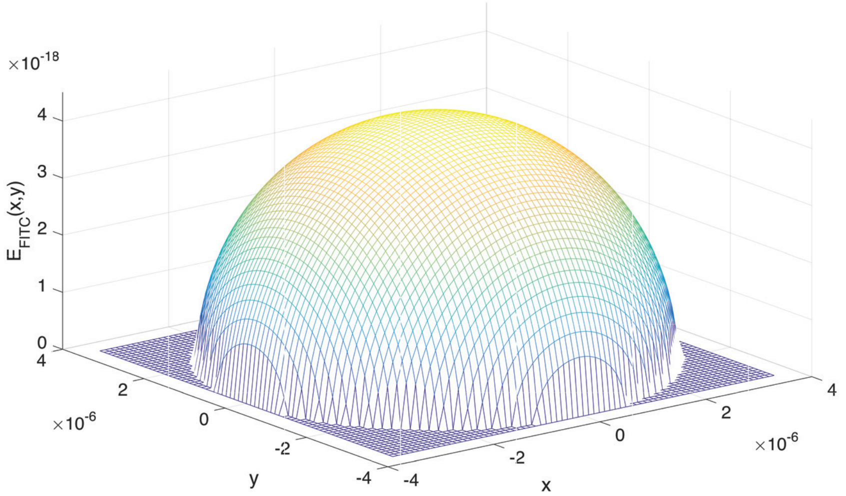

Figure 4.5. Absorbed energy at point (x, y) from FITC- conjugated protein in the cell cross section

Integrating the absorbed energy at given point (x, y) across the cell cross section, we calculated the total absorbed energy from Equation 3.19 seen in Table 4.1. From the total absorbed energy, we firstly determined the number of absorbed photons by the FITC fluorochrome that conjugates the target protein of interest in cell using Equation 3.20 to be 28733 photons of the laser wavelength of 488 nm.

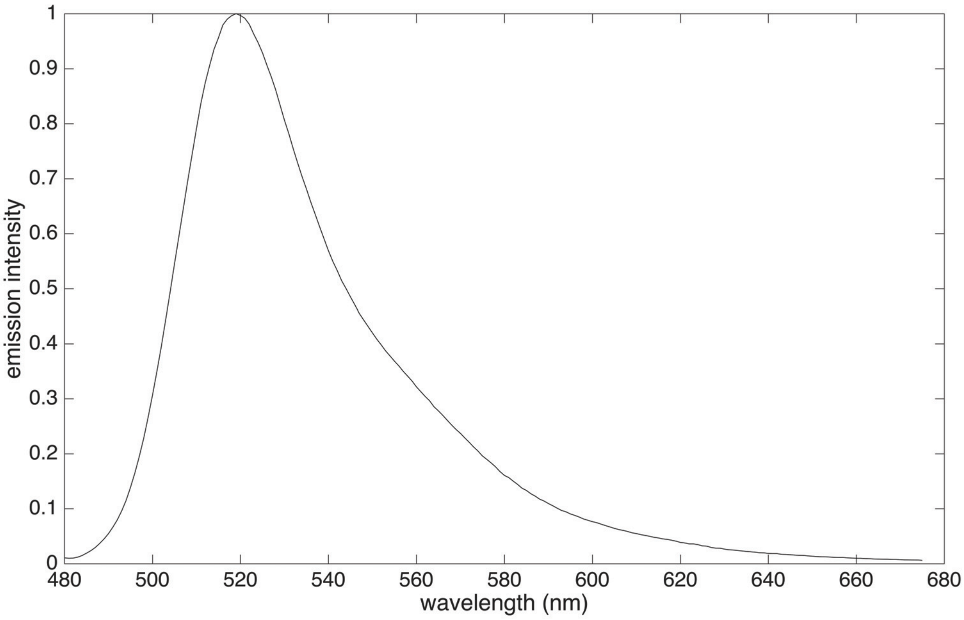

Figure 4.6. Emission Spectrum of FITC

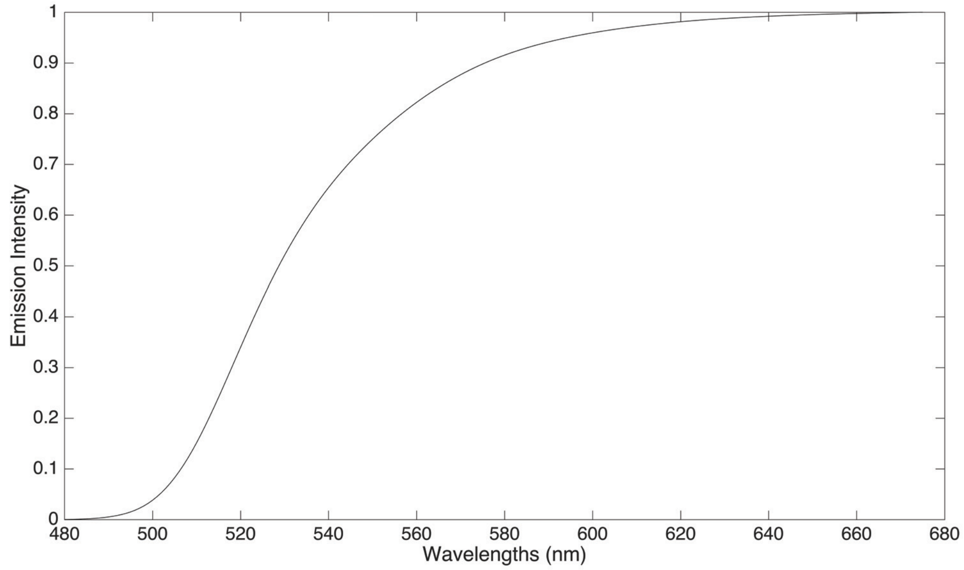

Figure 4.7. Cumulative Distribution Function of FITC

Then, from the quantum efficiency of the FITC dye, we calculated the number of emitted photons using Equations 3.28 and 3.29 to be 2643 photons. In the next step, we drew this number of photons from the emission spectrum of the FITC. The emission spectrum of FITC and its CDF can be seen from Figures 4.6 and 4.7, while the wavelength histogram of the generated photons is shown in Figure 4.8

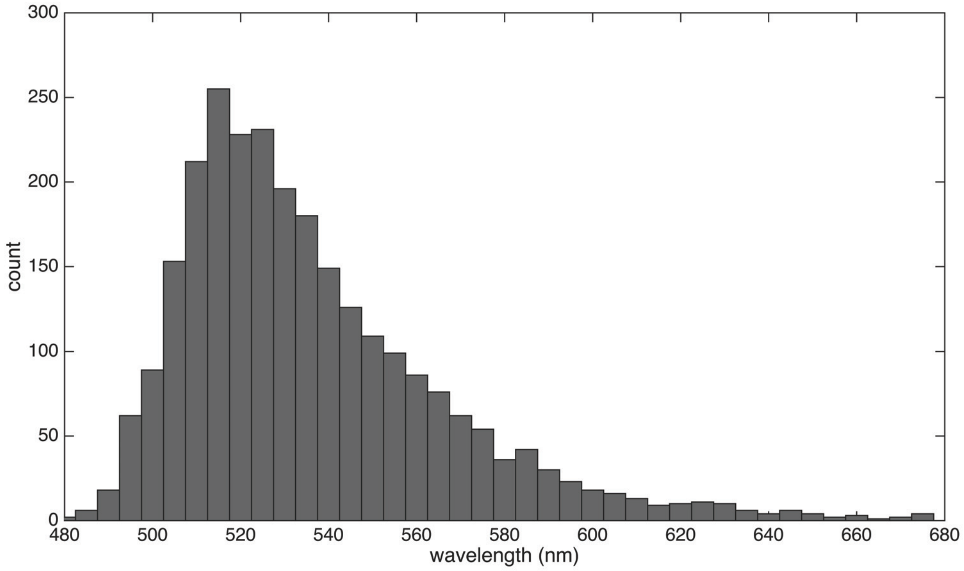

Figure 4.8. Wavelength histogram of the emitted photons from a FITC-conjugated cell for 2643 photons

These results are compatible with the emission spectrum of FITC as Figure 4.6 and Figure 4.8 show that there is a good match between the wavelength histogram of the emitted photons from FITC-conjugated proteins and the emission spectrum of FITC. Note that we have assumed that only a randomly selected ten percent of the emitted photons are routed towards the octagon detector array.

To determine which detector each photon falls, we firstly determined the probability with which the photons fall at each detector at the octagon detector array at these specific wavelengths. This was carried at using the probability curves shown in Figure 4.9 via linear interpolations as the curves in Figure 4.9 were obtained at integer wavelengths. Finally, we distributed all photons across the detectors using Equation 3.38, resulting in the histograms shown in Figure 4.10.

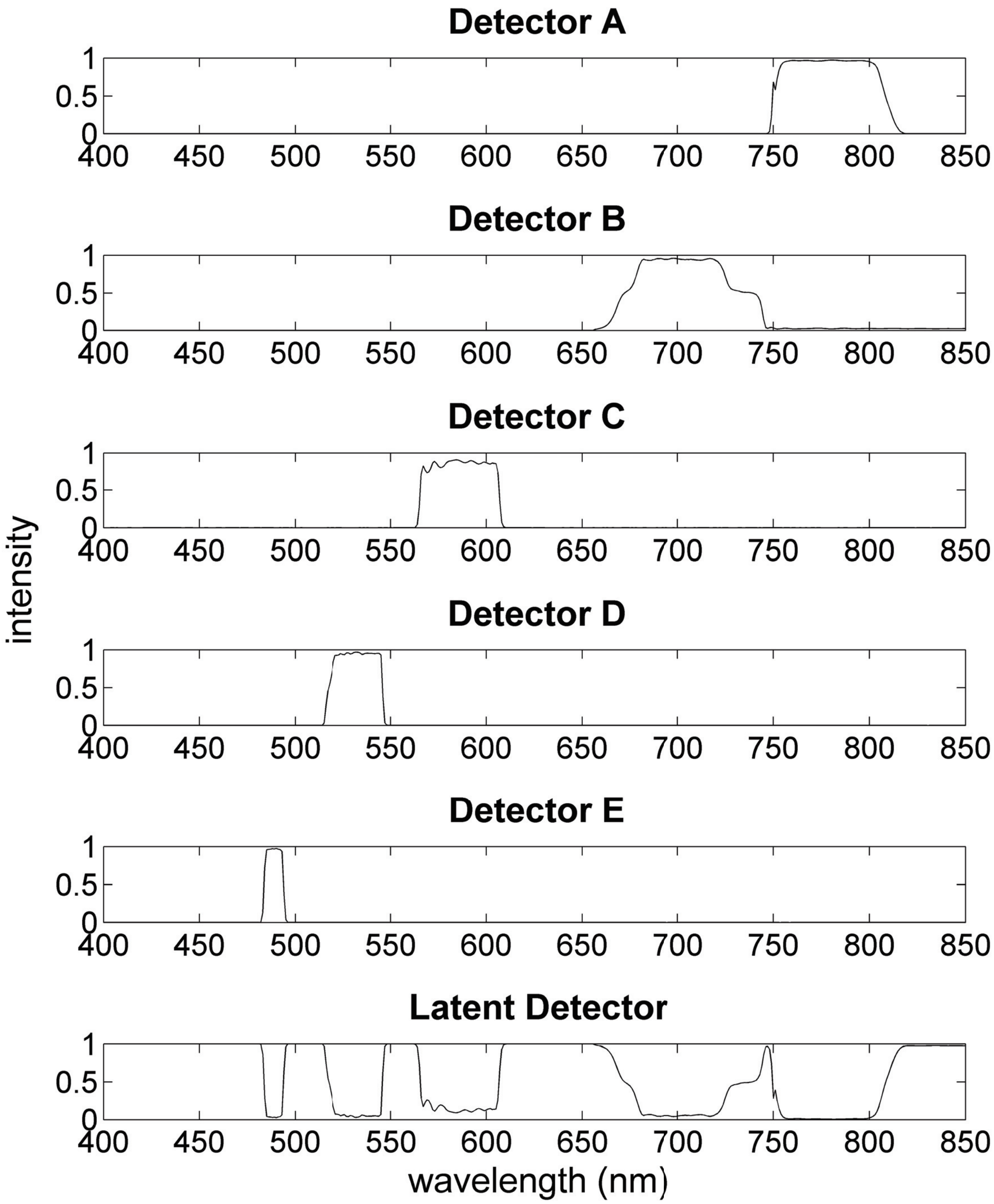

Figure 4.9. Probability curves of each detector at the octagon detector array

The wavelengths of emitted photons from FITC-conjugated proteins vary between 480 nm and 675 nm. The detector D was designed to detect FITC fluorescence intensity at the octagon detector array (Table 3.1). As expected, the results in Figure 4.10 show that the number of photons falling at detector D is greater than the other detectors. We observed no photons at detector A because the wavelength range of detector A does not

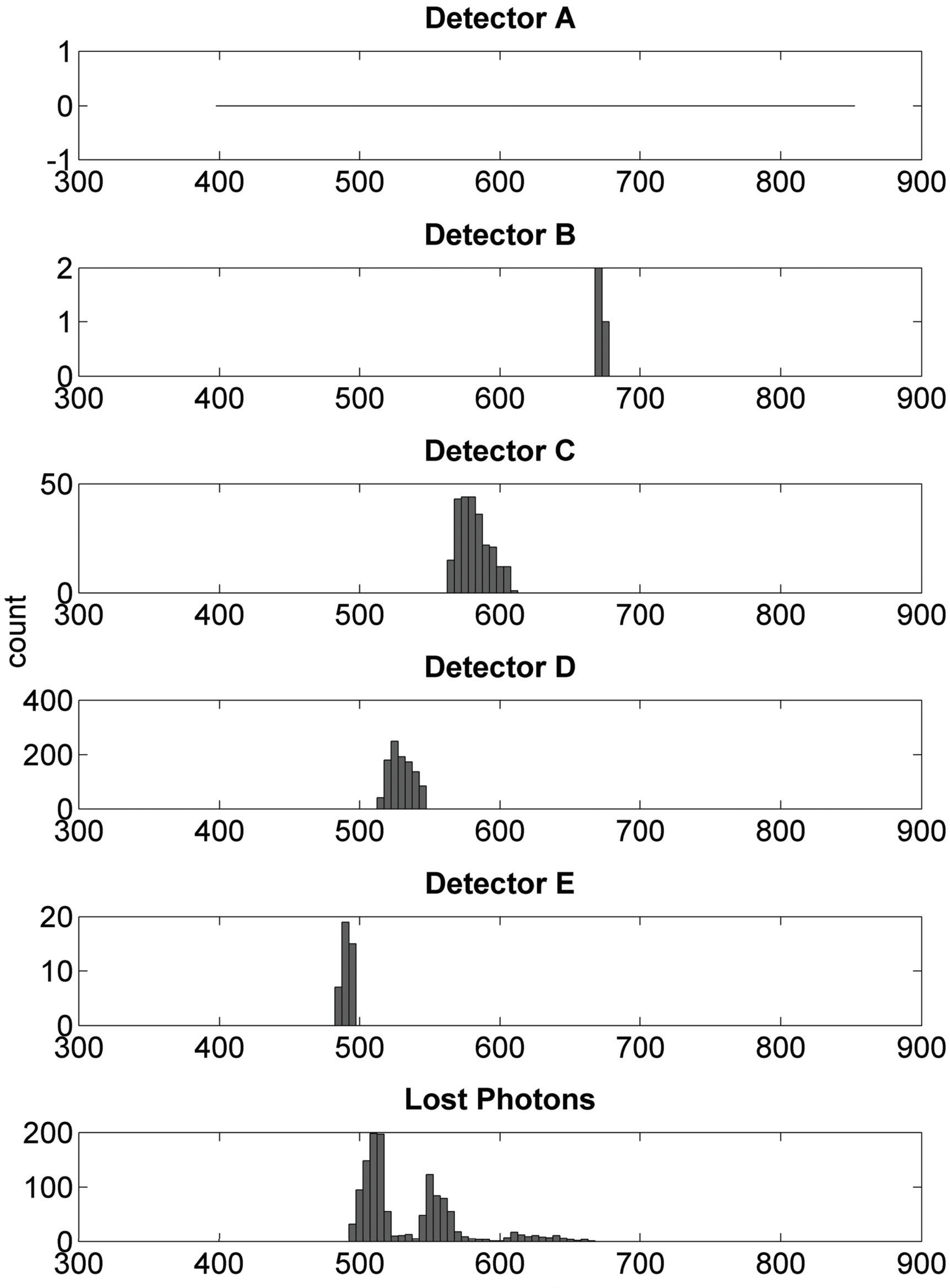

Figure 4.10. Wavelength histogram of the emitted photons by the FITC positive cell at different detectors and lost photons

overlap with the wavelength range of FITC emission. The maximum contribution was observed at detector C that was designed to detect PE fluorescence (Table 3.1). This is due to fact that, the corresponding wavelength range of PE emission varies between 525 nm and 725 nm that overlaps with the wavelength interval between 525nm and 680 nm of the PE detector.

All photons falling at a detector are then routed to the corresponding photomultiplier tubes. We determined the response of each photomultiplier tube as a current output. Then, for each current output and the corresponding excitation duration of the given cell, we determined the voltage pulse height of the pre-amplifier circuit.

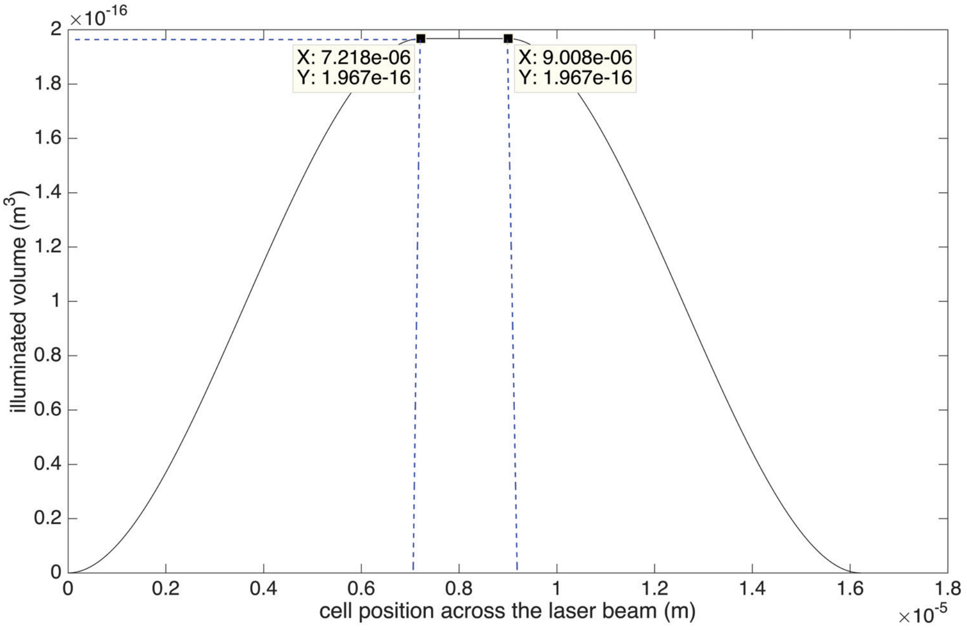

Figure 4.11. The illuminated volume of the cell under the laser illumination

We firstly calculated the excitation duration of each cell by determining the illuminated volume of the cell with respect to the position of leading edge of the cell through the interrogation point across the laser beam, as shown in Figure 4.11. Note that, we observed the maximum illuminated volume at point 7.2156×10^{-6}m that corresponds to the diameter of given cell in Table 4.1. The maximum illumination continues while the cell reaches to the width of the laser of 9×10^{-6}m. Normalizing the position with the flow velocity, we determined the illumination time of the cell (Figure 4.12). This allowed calculating a full width at half maximum value of 8.99769×10^{-7} seconds as the excitation duration of the cell.

We calculated the response of each detector as the height of voltage pulse for a given cell via bilinear interpolation in terms of the excitation duration of the cell and the

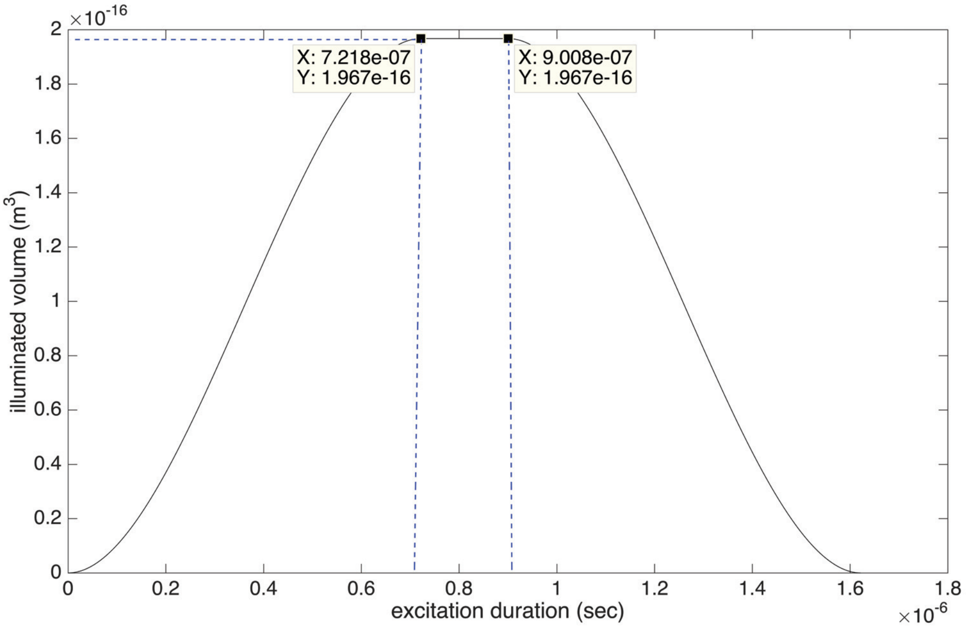

Figure 4.12. Time that the laser illuminates the cell

Table 4.2. Detector responses in terms of voltage height

Detector Responses	
Detector A	0
Detector B	0.0002V
Detector C	0.0401V
Detector D	0.1466V
Detector E	0.0072V

corresponding photomultiplier current strength. For bilinear interpolation, we simulated the pre-amplifier circuit shown in Figure 3.12 using various combinations of durations and current strengths to construct a reference voltage matrix (Table 4.3). Using this reference voltage matrix, we determined the detector responses obtained via bi-linear interpolation for the cell at hand as given in the following table and Figure 4.14.

Table 4.3. Reference voltage matrix in a table form

		Duration						
		200 ns	500 ns	800 ns	900 ns	1 μs	3 μs	5 μs
Current	0.1 nA	1.4074e-06	4.6187e-06	8.7109e-06	8.8956e-06	8.8838e-06	1.0330e-05	1.0344e-05
	1 nA	2.9825e-05	6.4414e-05	8.4470e-05	8.6312e-05	8.6193e-05	1.0238e-04	1.0111e-04
	10 nA	3.0465e-04	6.4280e-04	8.4200e-04	8.8249e-04	9.1427e-04	0.0010	0.0010
	100 nA	0.0030	0.0065	0.0084	0.0088	0.0092	0.0101	0.0101
	1 μA	0.0301	0.0640	0.0838	0.0881	0.0914	0.1006	0.1006
	10 μA	0.1791	0.3145	0.4336	0.4726	0.5115	1.0136	1.0137
	50 μA	0.3307	0.5005	0.6343	0.6762	0.7175	1.4889	2.1484
	100 μA	0.4148	0.6020	0.7433	0.7867	0.8292	1.5993	2.2477
	1 mA	0.6906	0.8500	0.9809	1.0228	1.0644	1.8434	2.4849
	2 mA	0.7423	0.8949	1.0236	1.0652	1.1067	1.8868	2.5281
	7 mA	0.8268	0.9723	1.0992	1.1405	1.1819	1.9649	2.6060
		Voltage Height						

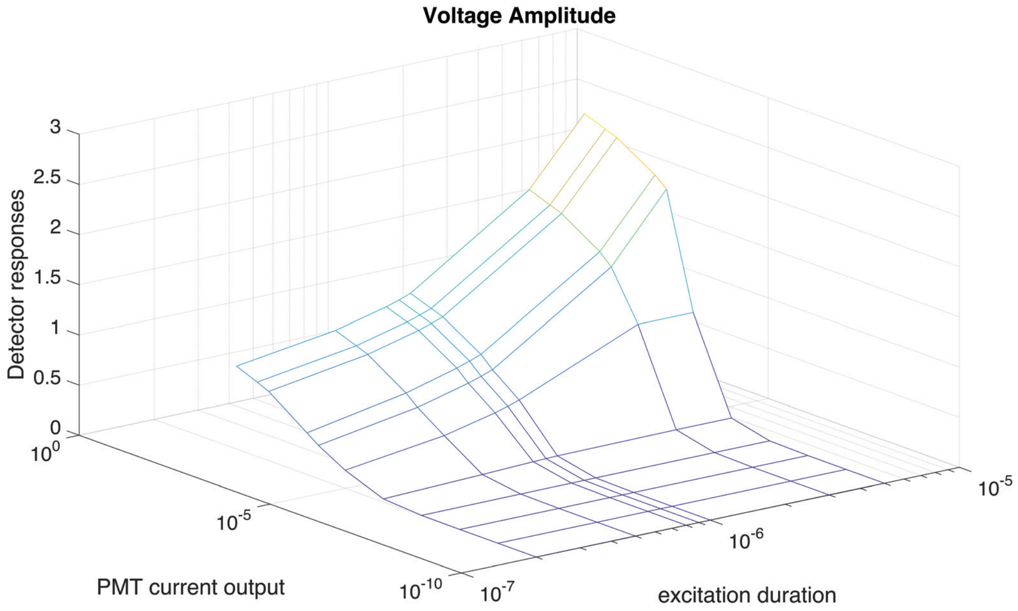

Figure 4.13. Surface graph of the reference voltage matrix

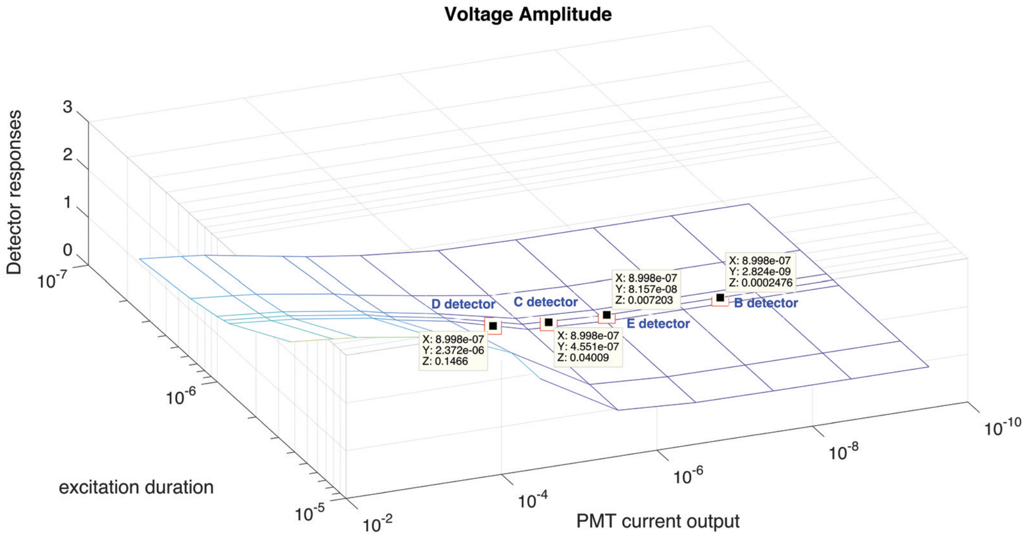

Figure 4.14. Detector responses obtained via bilinear interpolation

Note that these results are compatible with the histogram of the emitted photons received at different detectors. The maximum number of photons were received at detector D, and we observed the maximum detector response at detector D. Because, the detector D was designed to detect FITC fluorescence detector while the detector C was designed for determining PE fluorescence (Table 3.1). We have determined the maximum contribution from FITC fluorescence into detector C. The FITC spillover into PE channel is an expected result due to the closest emission spectra of FITC and PE.

4.3. Results for a Single Cell with PE-Conjugated Proteins

We have repeated the previous calculations for a cell of identical size that is positive for PE-conjugated proteins. Table 4.1 summarizes the size value of the cell and its corresponding number of the target protein and total absorbed energy E_{PE}, calculated using again Equation 3.26, for given radius and the corresponding number of the PE-conjugated target protein of the cell. The total absorbed energy depends on the target protein concentration in the cell. The number of the PE-conjugated target proteins is bigger than the number of the FITC-conjugated target protein for this cell. For this reason, the total absorbed energy from PE-conjugated target protein is bigger than the total absorbed from FITC-conjugated target protein for the earlier cell. Note that the extinction coefficient of PE is also bigger than the extinction coefficient of FITC.

Table 4.4. PE-conjugated cell

Radius	3.6078e-06m
Target Protein Number	1.4535e+09 copies
E_{PE}	1.8901e-13 joules

The laser path length entering the cell does not vary at point (x, y) in the cross section, since the cell size is identical the earlier cell.

Therefore, using the same laser path length, we calculated the absorbed energy by PE at a point (x, y) as in Figure 4.15.

The difference between the absorbed energy at a point (x, y) by PE-fluorochrome and the absorbed energy at the same point from FITC is due to differences in the number of target proteins and the differences in the extinction coefficients.

As before, we calculated the total absorbed energy by PE-fluorochrome in the cell given in Table 4.4, and determined the number of absorbed photons using Equation 3.20 to be equal to 464014.

Using the quantum efficiency of PE-fluorochrome, we obtained the number of emitted photons exiting by PE-fluorochrome that conjugates the target protein of interest in the cell to be equal to 38049 photons. Then, we sampled the PE emission spectrum

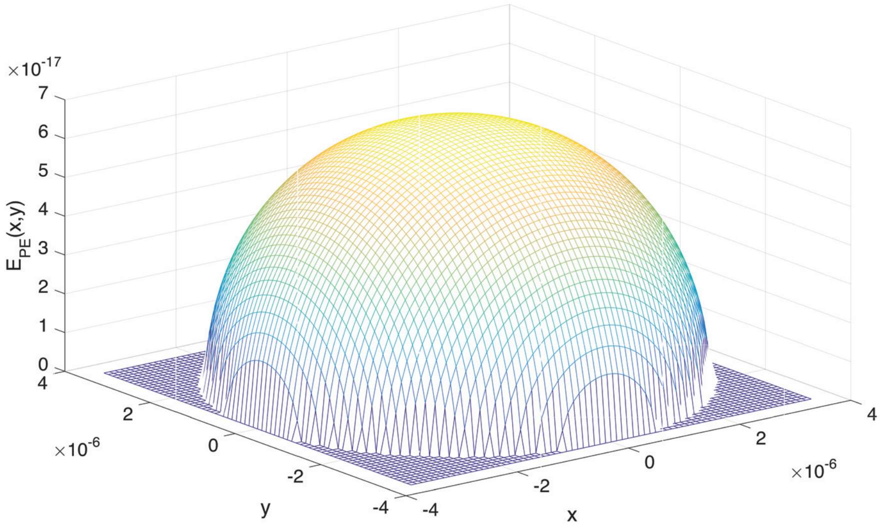

Figure 4.15. Absorbed energy at point (x, y) from PE-conjugated protein in the cell cross section

as a probability density function by the same number. The emission spectrum of PE and its CDF can be seen from Figures 4.16 and 4.17, with the wavelength histogram of the generated photons in Figure 4.18.

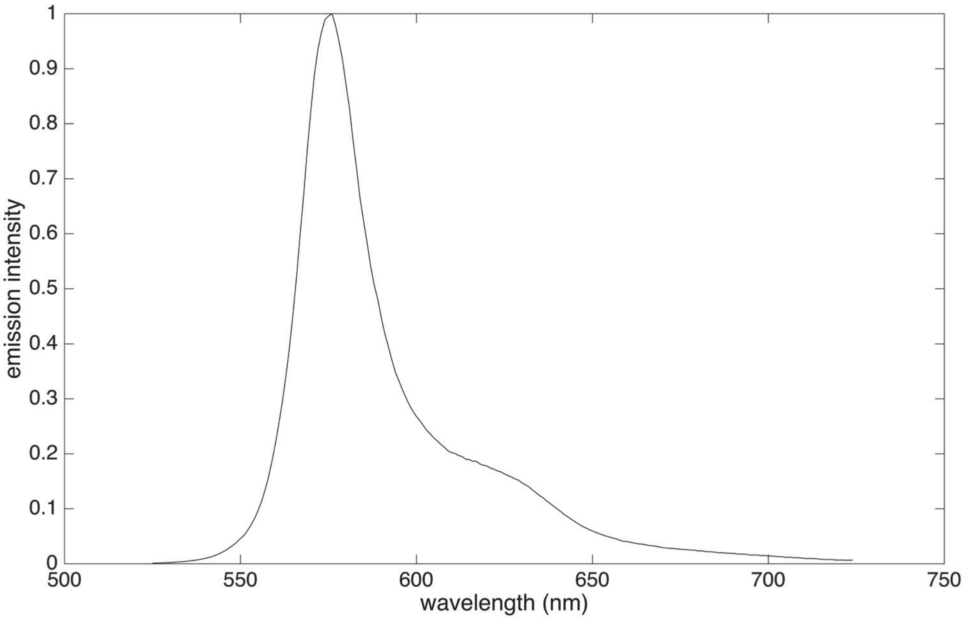

Figure 4.16. Emission Spectrum of PE

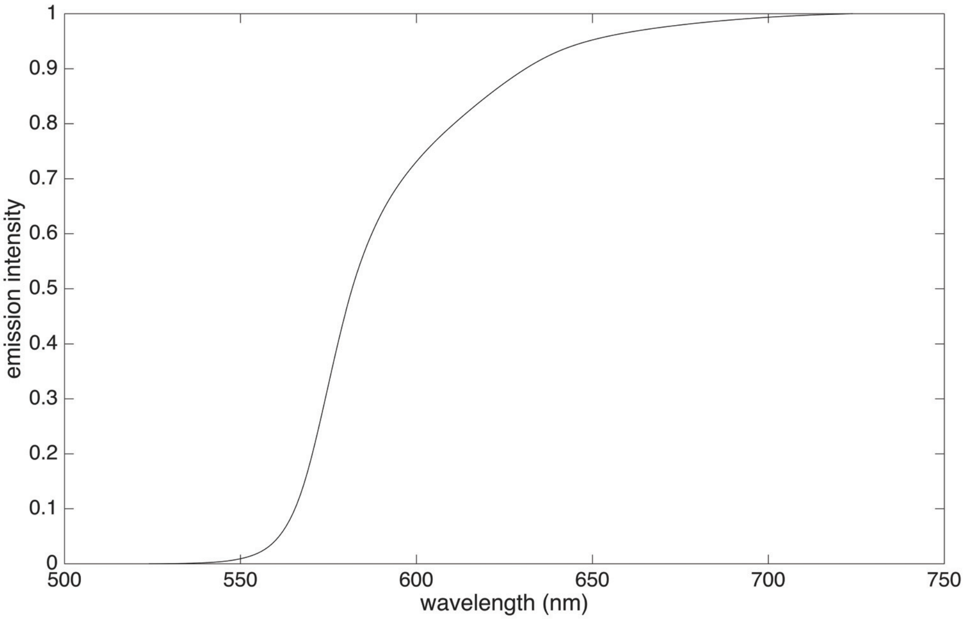

Figure 4.17. Cumulative Distribution Function of PE

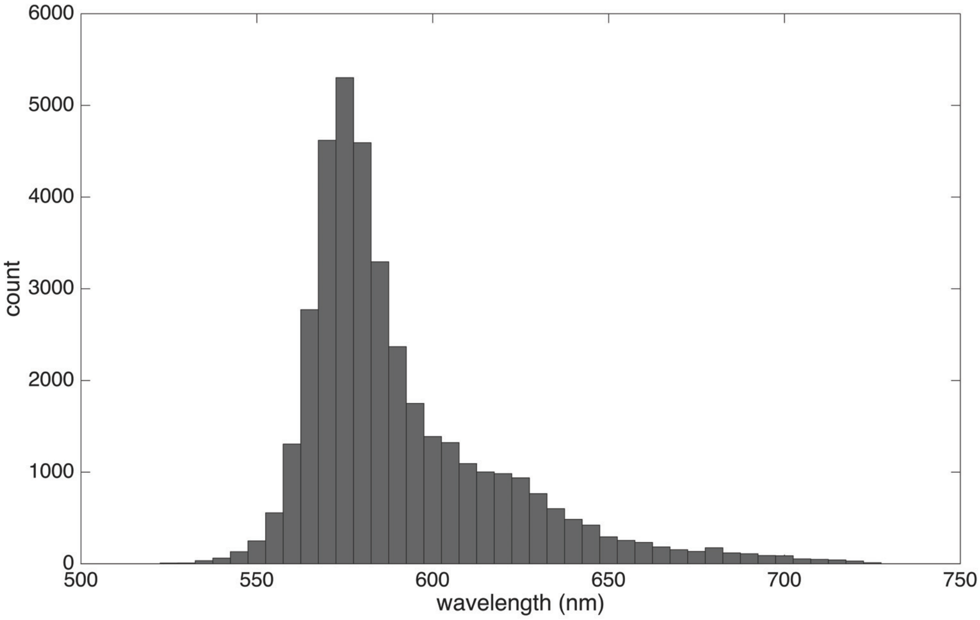

Figure 4.18. Wavelength histogram of the emitted photons from a PE-conjugated cell for 38049 photons

As expected the wavelength histogram of the emitted photons from a PE-conjugated cell is in good agreement with the emission spectrum of PE.

After determining the wavelength of the emitted photons, we randomly selected 0.1 and distributed them across the detectors of the octagon detector array using the probability curves of the detectors shown in Figure 4.9.

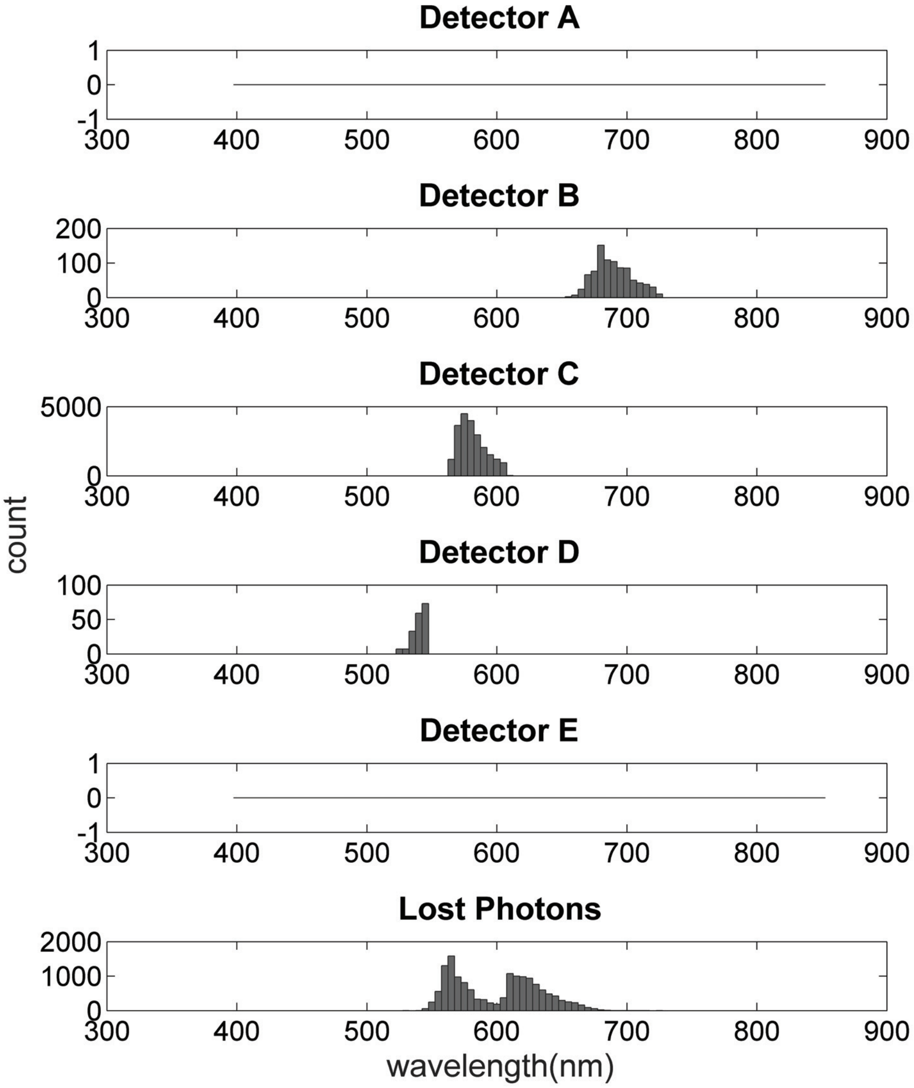

Figure 4.19. Wavelength histogram of the emitted photons by the PE positive cell at different detectors and lost photons

The histograms of the photons falling at each detector is shown in Figure 4.19. Note that, the wavelength range of emitted photons from PE fluorochrome varies between 525 nm and 725 nm. As seen in Table 3.1 in the previous chapter, C detector was designed to detect PE fluorescence intensity in the octagon detector array. We observed that the number falling photons at detector C is greater than the other detectors. The results show that there is no contribution from PE fluorescence at detectors A and E because the wavelength ranges of detectors A and E do not overlap with the wavelength range PE emission. The largest contributions were observed at the detectors B and D that were designed to detect PerCP and FITC fluorescences respectively. The detectors B and D detect the photons with wavelengths 650 nm to 750 nm and 515 nm to 545 nm, respectively. For this reason, the wavelength ranges of B and D detectors overlap with the wavelength range of the PE fluorescence.

All photons received at detectors B, C, and D were directed to their photomultiplier tubes. We calculated the current output of each photomultiplier tube. The illumination times or excitation durations do not vary because the cell is identical in size to the previous cell studied in the section 4.2. Using the current outputs of the photomultiplier tubes and the excitation duration of cell, we determined detector responses via bilinear interpolation (Table 4.5).

Table 4.5. Detector responses in terms of voltage height

Detector Responses	
Detector A	0
Detector B	0.0706V
Detector C	0.6034V
Detector D	0.0322V
Detector E	0

These results show that the detector responses are in agreement with the number emitted photons falling on each detector. Figure 4.20 shows the detector response of each detector given in Table 4.5.

Finally, we compare results of detector responses of the FITC-conjugated proteins that is positive in a cell with again the same cell that is positive PE-conjugated proteins, detector responses change according to the total absorbed energy from the PE-fluorochrome that affects the number of photons emitted from PE-fluorochrome, and also the number of falling photons at each detector. The detector responses are is a good agreement with wavelength histogram of emitted photons by the PE fluorochrome that conjugated to the target protein of interest at the different detectors.

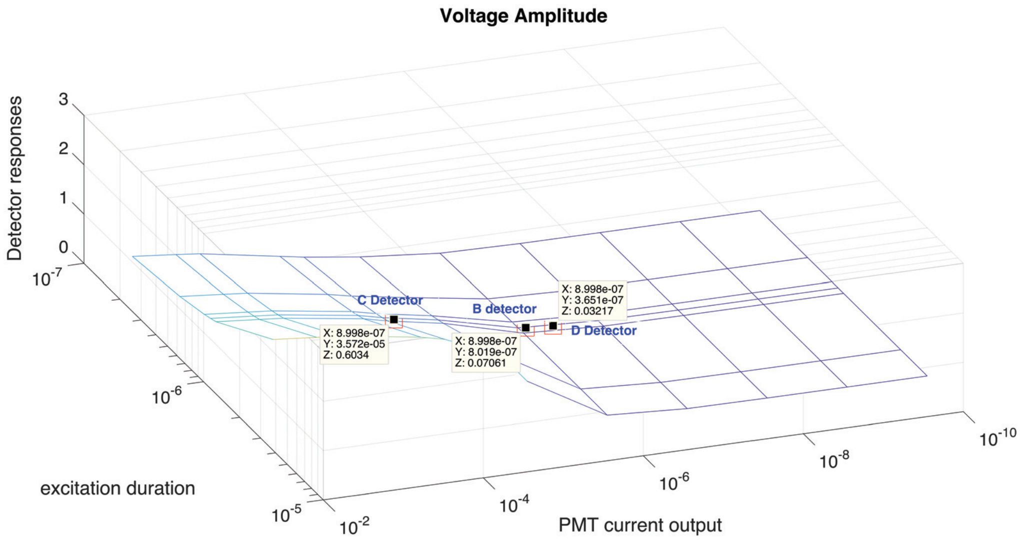

Figure 4.20. Detector responses

4.3.1. Results for a Single Cell with Two Fluorochromes

Earlier, we investigated the differences between the results of total absorbed energies and detector responses for a randomly selected positive cell for firstly FITC-conjugated proteins and for secondly PE-conjugated proteins. Here, we investigate the detector responses for a cell that is positive for both FITC and PE conjugated proteins. We have repeated all calculations for a cell with the same that is positive for both FITC and PE conjugated proteins. Table 4.6 represents the size of cell, the number of target proteins of interest, and the total absorbed energies from FITC-conjugated proteins and from PE-conjugated proteins in the cell. E_{FITC} and E_{PE} denote respectively the total absorbed energies from FITC-conjugated and PE-conjugated proteins.

Table 4.6. FITC and PE conjugated cell

Radius	3.6078e-06m
FITC-conjugated target protein number	1.3117e+09 copies
PE-conjugated target protein number	1.4535e+09 copies
E_{FITC}	1.1614e-14 joules
E_{PE}	1.8755e-13 joules
E_{total}	1.9917e-13 joules
$\tilde{E}$	2.0071e-13 joules

It is clear that there is no difference in the laser path length entering the cell at point (x, y) in the cross-section. We firstly calculated total absorbed energy, $E_{total}(x, y)$, by both FITC and PE conjugated proteins at point (x, y) using Equation 3.22 and determined how much of $E_{total}(x, y)$ is absorbed by FITC-conjugated proteins and PE-conjugated proteins. The resulting plots for $E_{FITC}(x, y)$ and $E_{PE}(x, y)$ are given in Figures 4.21 and 4.22. Then, we calculated the absorbed energy by FITC-conjugated proteins and PE-conjugated proteins across the cell using Equation 3.26.

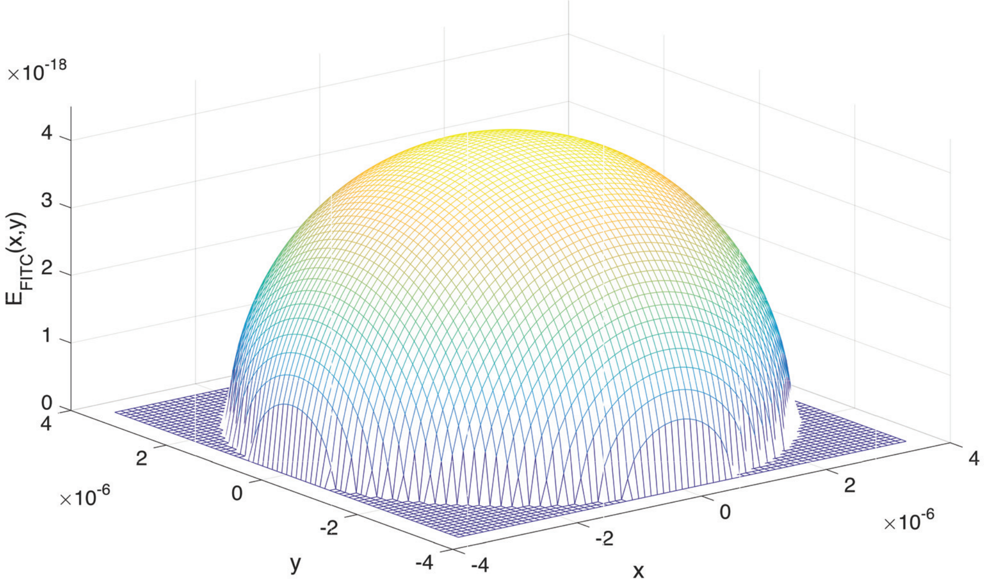

Figure 4.21. Absorbed energy at a point (x, y) by FITC-conjugated protein in the cell cross section

The previous sections have revealed that the absorbed energy E_{FITC} by the FITC-conjugated target proteins that is positive for the selected cell, equalling 1.1704×10^{-14} joules and the absorbed energy E_{PE} by PE-conjugated target proteins that is positive for the cell of identical size, equalling 1.18901×10^{-14} joules. We observed that the absorbed energy E_{FITC} by both FITC and PE conjugated target proteins that are positive for same selected cell with identical protein numbers and radius to the previous cell. The absorbed energy E_{FITC} decreases from 1.1704×10^{-14} joules to 1.614×10^{-14} joules, while the absorbed energy E_{PE} decreases from 1.18901×10^{-14} to 1.8755×10^{-14}. Because, the PE-conjugated target proteins use simultaneously the energy of FITC-conjugated target proteins during the energy absorbance. Using the absorbed energies, we calculated the number of photons emitted from FITC and PE fluorochromes that are conjugated to their

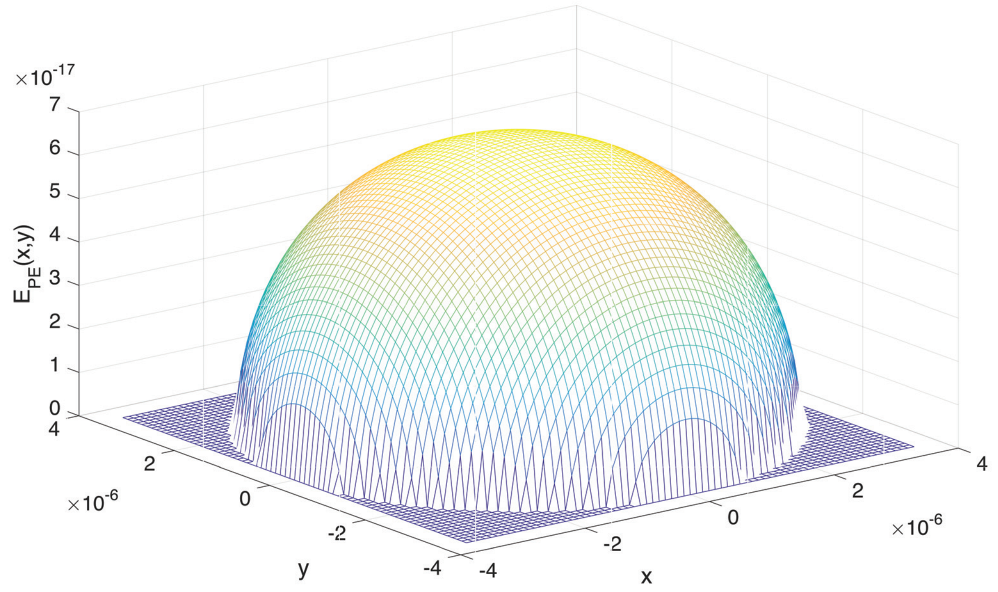

Figure 4.22. Absorbed energy at a point (x, y) by PE-conjugated protein in the cell cross section

target proteins of interest in the cell, and drew corresponding numbers of photon wavelengths from their emission spectra. The wavelength histograms of the emitted photons is shown in Figure 4.23.

As is clear from the previous results in Figures 4.16 and 4.18, the wavelength histogram of the emitted photons by the fluorochrome conjugated target proteins of interest that is positive for the cell is compatible with the emission spectrum of the fluorochrome. We observed that the result of wavelength histogram of the total emitted photons in Figure 4.23 appears the sum of the wavelength histograms of the FITC-conjugated target proteins with the PE-conjugated target proteins. Note that again the wavelength range of PE emission spectrum varies between 525 nm and 725 nm shown in Figure 4.16, and similarly, FITC emission spectrum varies between 480 nm and 675 nm shown in Figure 4.6. In the result of wavelength histogram of total emitted photons in Figure 4.23, the wavelength range varies between 480 nm and 725 nm. There is a good match between the result of the wavelength histogram of total emitted photons by both FITC and PE conjugated target proteins and wavelength histograms of the emitted photons from FITC-conjugated and PE-conjugated target proteins in Figures 4.8 and 4.18, respectively.

Then, we distributed 0.1 of all emitted photons across the detectors in the octagon detector array according to the probability curves shown in Figure 4.9. The wavelength

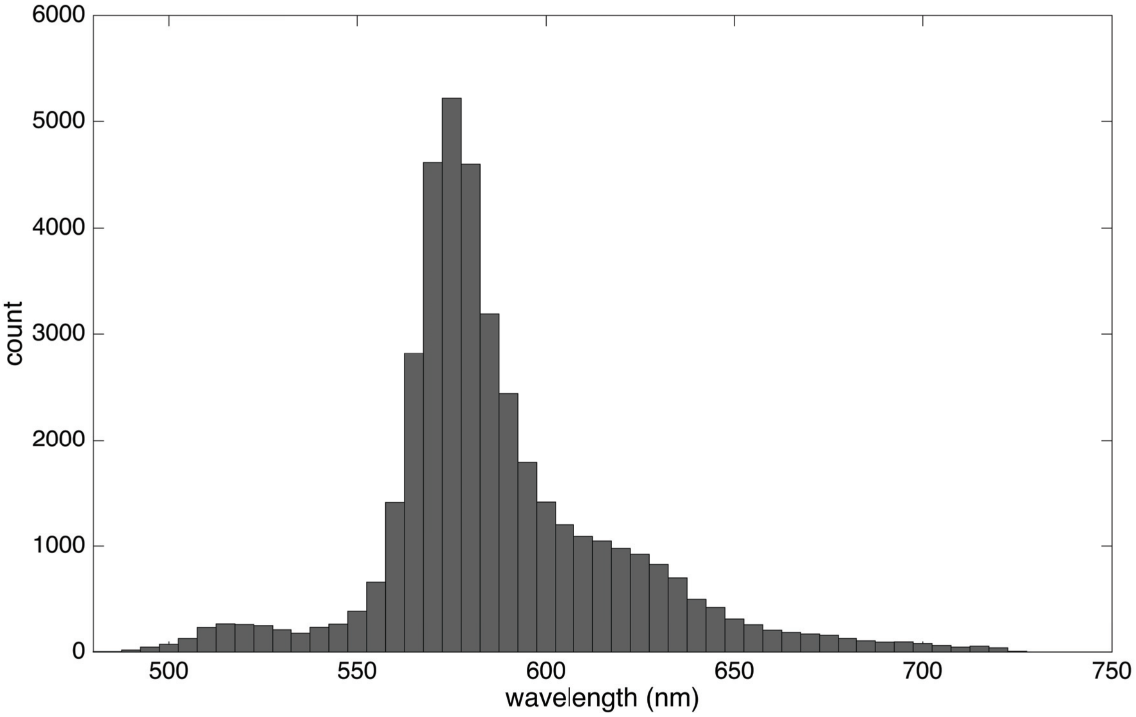

Figure 4.23. Wavelength histogram of the total emitted photons for a cell that is positive for FITC-conjugated target protein and also positive for a PE-conjugated target protein

histograms of the photons falling at each detector are given in the following figure. The results from each corresponding detector are given in the following figure.

These results show that the number of photons falling at detector C is bigger than the other detectors. From this we conclude that the the wavelength histograms of the emitted photons at different detectors from PE-conjugated proteins in Figure 4.19 and FITC-conjugated proteins in Figure 4.10 are in good correspond with the wavelength histogram of the emitted photons at different detectors from both FITC and PE conjugated proteins. We observed again no contribution from FITC and PE fluorescences at detector A because the wavelength range of detector A does not include the wavelength ranges PE and FITC emission.

All photons received by the detectors B, C, D and E are routed towards their photomultiplier tubes. We calculated the current output of each photomultiplier tube. The excitation duration does not vary because the cell is identical in size with the cells in the previous sections. Then, we determined the detector responses via bilinear interpolation in terms of the excitation duration and the current outputs from the different photomultiplier tubes.

Figure 4.25 shows detector response of each detector given the reference matrix.

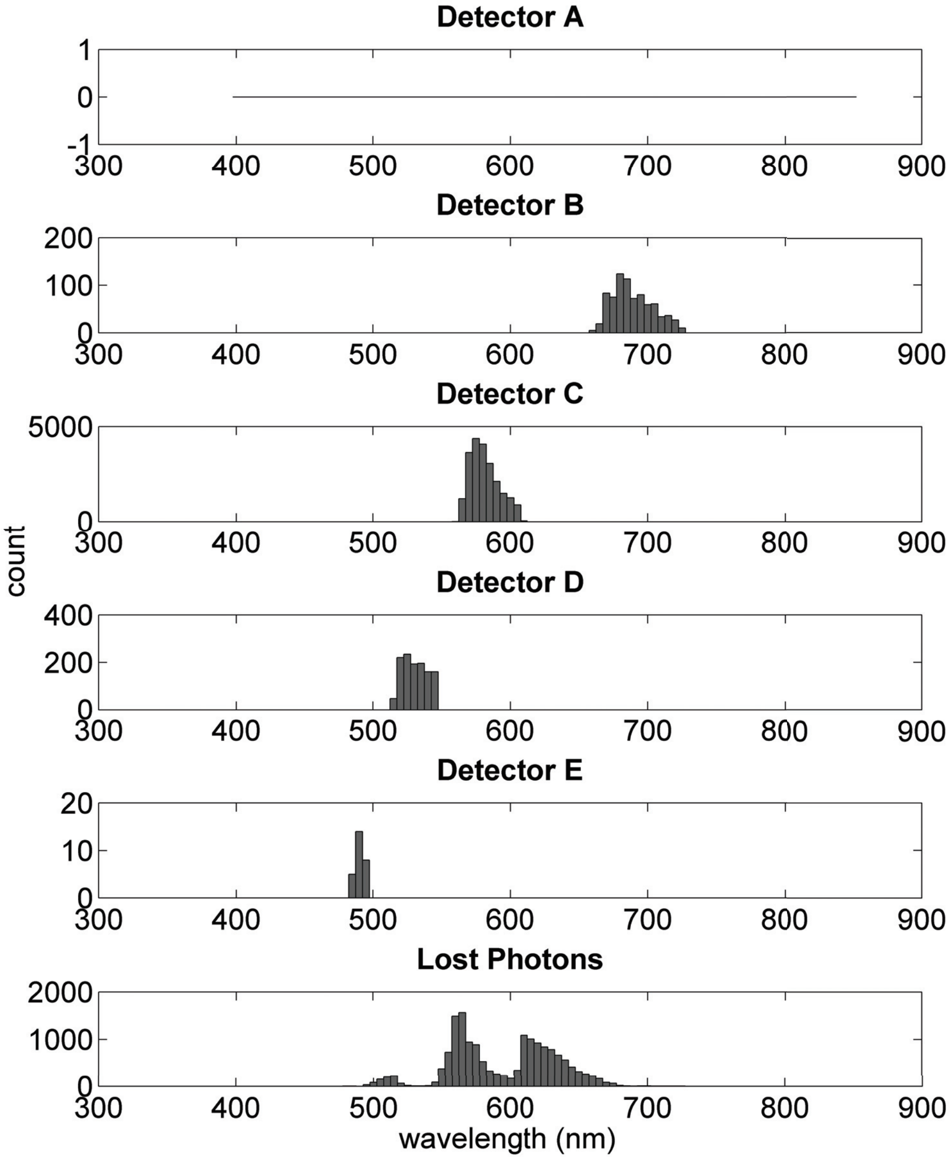

Figure 4.24. Wavelength histogram of the emitted photons by the FITC and PE positive cell at different detectors and lost photons

When we compare the results of the detector responses of the cell that is positive for FITC-conjugated proteins with the same cell is that positive for FITC and PE conjugated proteins, we notice that the unwanted contributions from PE fluorescence is increased at detector D. In the same way, we compare the results of the detector responses of the cell that is positive for PE-conjugated proteins with the FITC and PE conjugated proteins again for the same cell, we also observed that the unwanted contributions from FITC fluorescence increase in detector C.

Table 4.7. Detector responses in terms of voltage height

Detector Responses	
Detector A	0
Detector B	0.0657V
Detector C	0.6045V
Detector D	0.1572V
Detector E	0.0063V

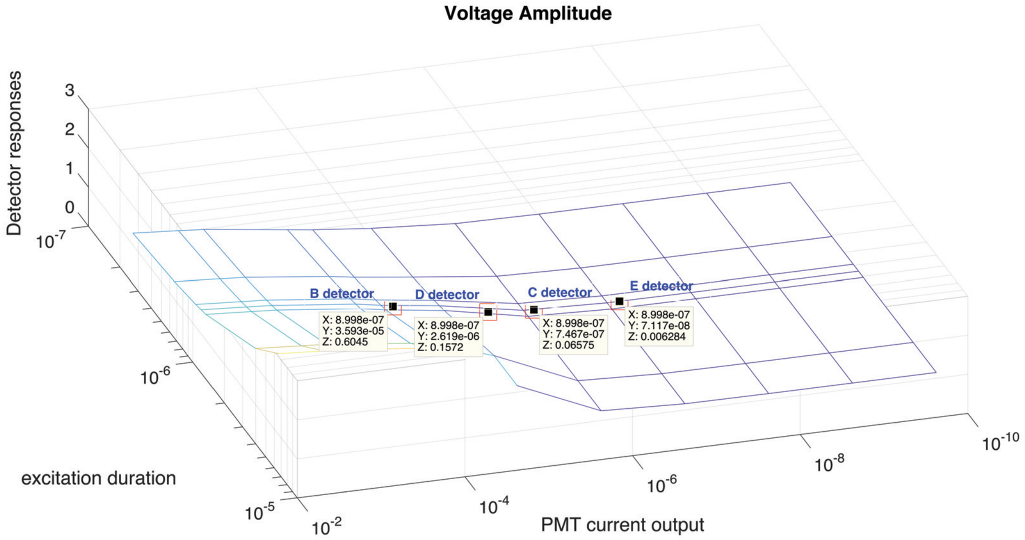

Figure 4.25. Detector responses

4.4. Results for a Group of Cells

In this section, we present the detector reading results from a group of cells including ++, +-, -+, - - cell groups. The double negative cell group produces autofluorescence emissions only. We have explained the details of autofluorescence in Section 2.4. We assumed that the double negative (- -) cells conjugate to a latent fluorochrome to model autofluorescence as a background signal. The ++ cell group contains the cells that are positive for both FITC and PE conjugated proteins. The +- cell group describes the cells that are positive for FITC-conjugated proteins while they are negative for PE-conjugated proteins. Similarly, the - + cell group describes the cells that are positive for PE-conjugated proteins but negative for FITC-conjugated proteins. Note that ++, +-, -+ cell groups also contain the latent fluorochrome-conjugated proteins, accounting for the autofluorescence in the cells. Finally, we created a group of 4000 model cells constructed from 1000 + +, 1000 + -, 1000 - +, and 1000 - - cells shown in Figure 4.26. The following figure shows the scatter plot of the target proteins of interest in the group 4000 model cells.

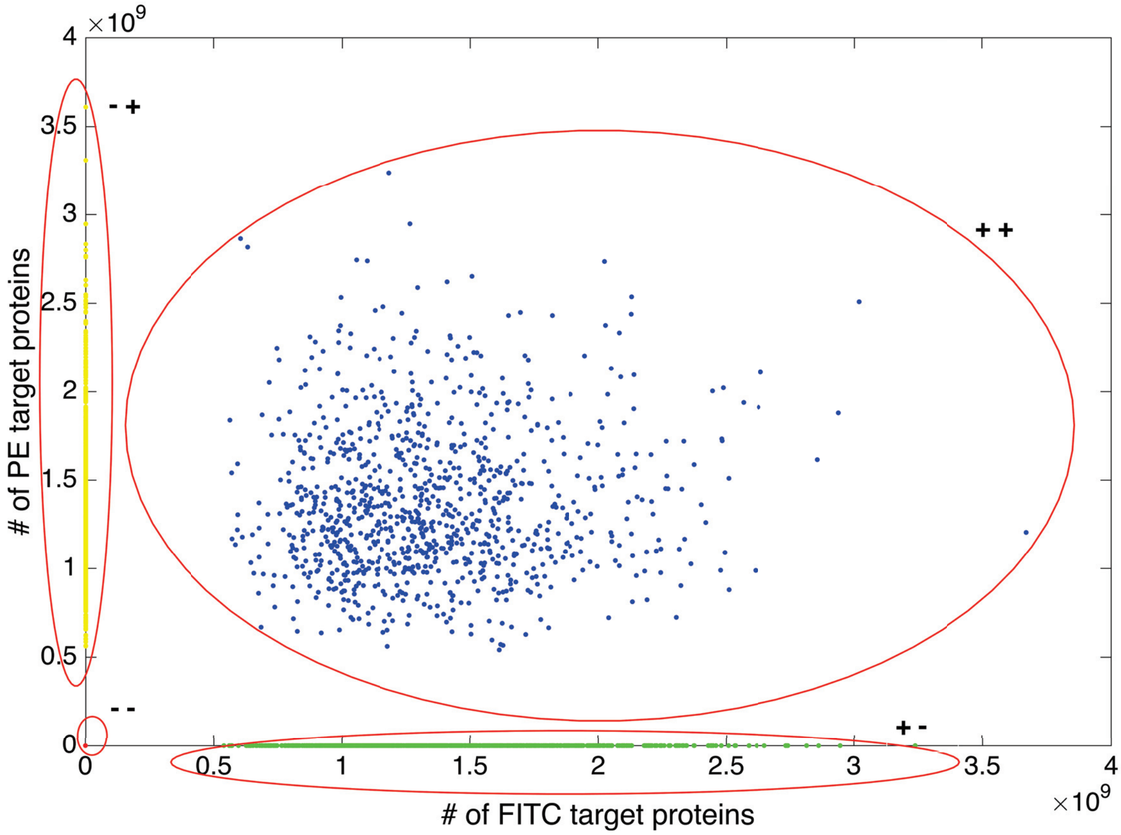

Figure 4.26. The number of target proteins for + +, + -, + - and - - cell groups

The blue group represents the + + cell group, the green group the + - cell group through the horizontal axis, the yellow group - + cell group through the vertical axis, and the red group the - - cell group placed at the origin that is negative for both FITC and PE conjugated target proteins. Note that the objective of flow cytometry is to identify the cells that are positive for a specific fluorochrome from the others. To this end, the positive and negative cell distributions are positioned in different quadrants of the scatter plots showing one fluorochrome intensity against another. In these cell groups, the cells have some latent substances causing to autofluorescence. To calculate autofluorescence intensity, we assumed that these latent substances behave like a latent fluorochrome. We determined the autofluorescence intensity according to FITC fluorescence. We assumed that the number of photons received from autofluorescence are uniformly distributed in the detector wavelength range as [400nm, 850nm]. This ratio is given by;

$$\frac{N_D}{\mu_{af}} = \frac{\int_{400}^{850} P_D(\lambda) d\lambda}{(850 - 450)} \tag{4.1}$$

where N_D is the average number of photons falling in D detector, and μ_{af} denotes the average number of photons expected to be emitted via autofluorescence, and P_D represents the probability curve of D detector. Then, we selected N_{af}, the actual number of photons emitted via autofluorescence for a given cell as $(\mathcal{N}(\mu, \, (\frac{\mu}{5\text{x}1.96})^2$.

To determine the different detector responses for each cell in the cell groups, we carried at all calculations described in the earlier sections. The resulting detector responses at detector C and detector D are given in the following figure. Note that the cells can be positive for FITC-conjugated proteins or for PE-conjugated proteins or for both FITC and PE conjugated proteins. For this reason, we have given the responses of detectors D versus C that are dedicated to the FITC and the PE fluorescence emissions, respectively. In other words, we displayed the FITC intensity against the PE intensity in Figure 4.27 along with the spectral spillover between them. All results show that we observed the + +, + - , - +, and - - cell groups roughly at the corresponding quadrants both in the linear scale (Fig.4.27) and the log-scale (Fig.4.28).

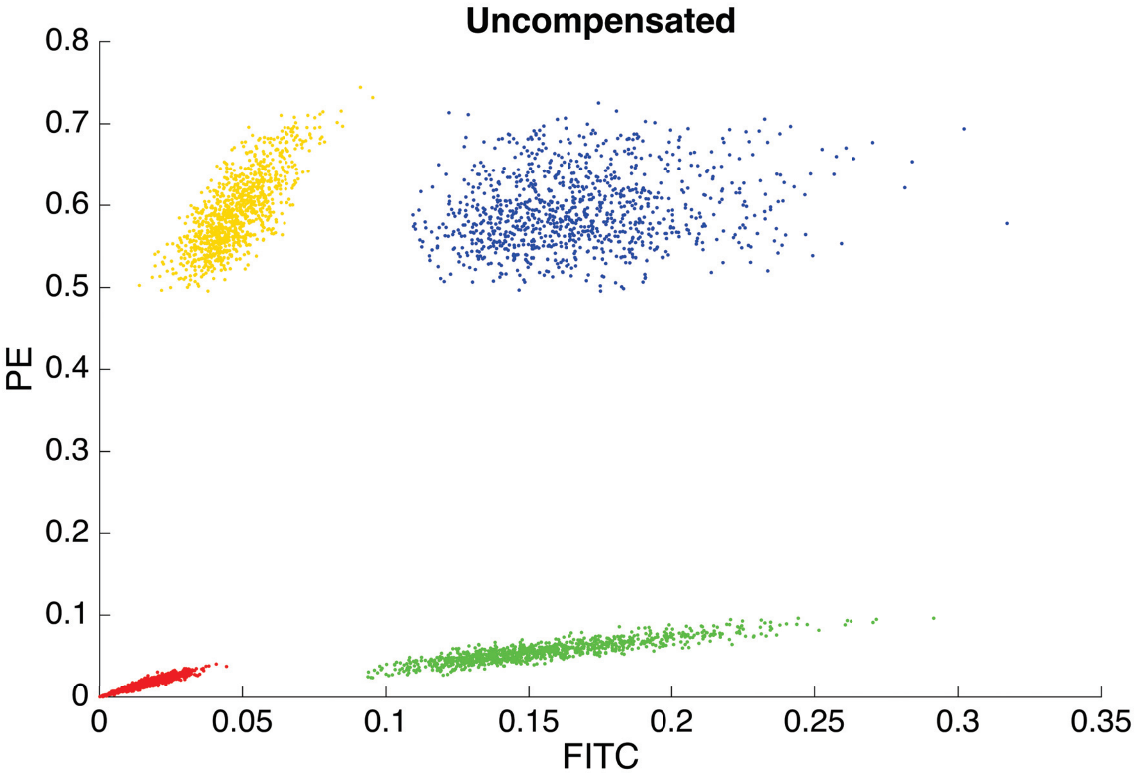

Figure 4.27. The results of the detector responses for each of 4000 cells containing + +, + -, + - and - - cell groups in the linear scale

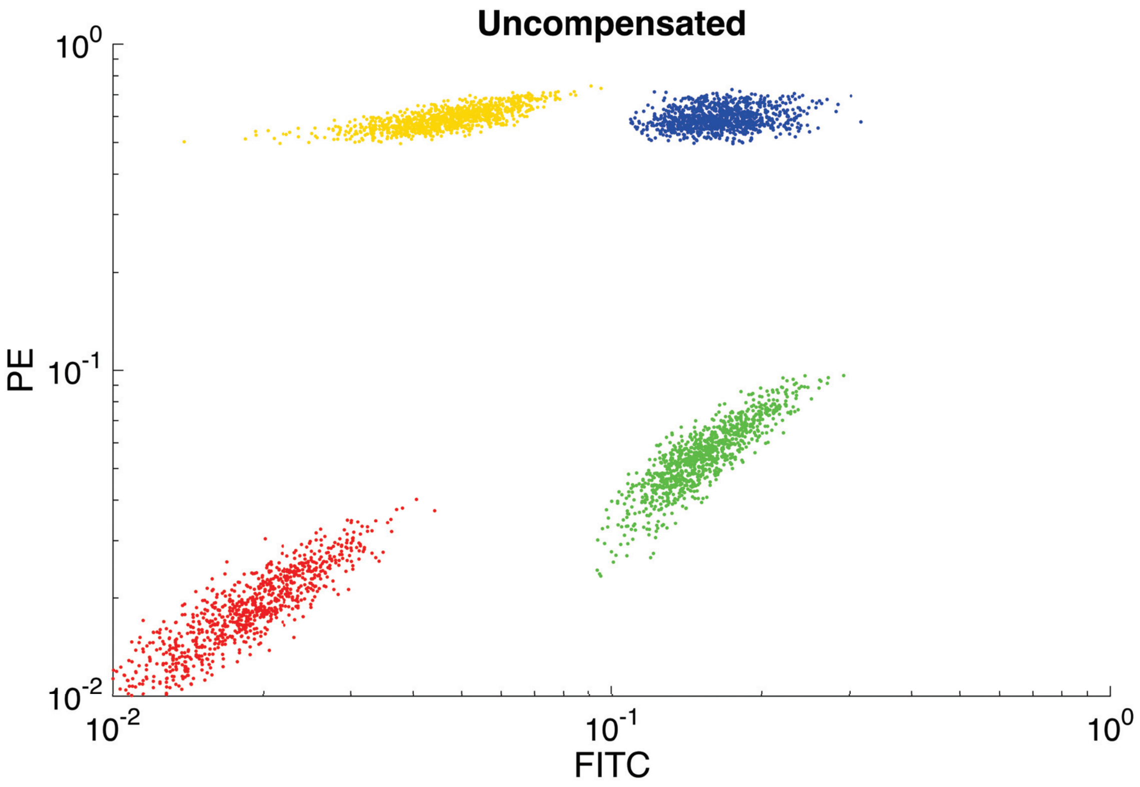

Figure 4.28. The results of the detector responses for 4000 cells in the log-scale

4.5. Compensation

Our ground-truth dataset described in the previous section contains detector responses characterizing fluorescence intensities from a group of model cells that could be positive or negative for FITC-conjugated proteins, PE-conjugated proteins, and both. We applied a formulaic linear compensation method (Bagwell and Adams, 1993) and then a manual linear compensation to the ground-truth dataset to determine the contributions from the unintended fluorochrome at the detectors.

4.5.1. Formulaic Linear Compensation

We firstly applied linear compensation described for two colours (Bagwell and Adams, 1993). This approach was developed based on a binary communication channel shown in the following figure.

In Figure 4.29, s_1 and s_2 denote fluorescence intensities from fluorochromes 1 and 2, while o_1 and o_2 represent the observed signals including spectral overlaps. The

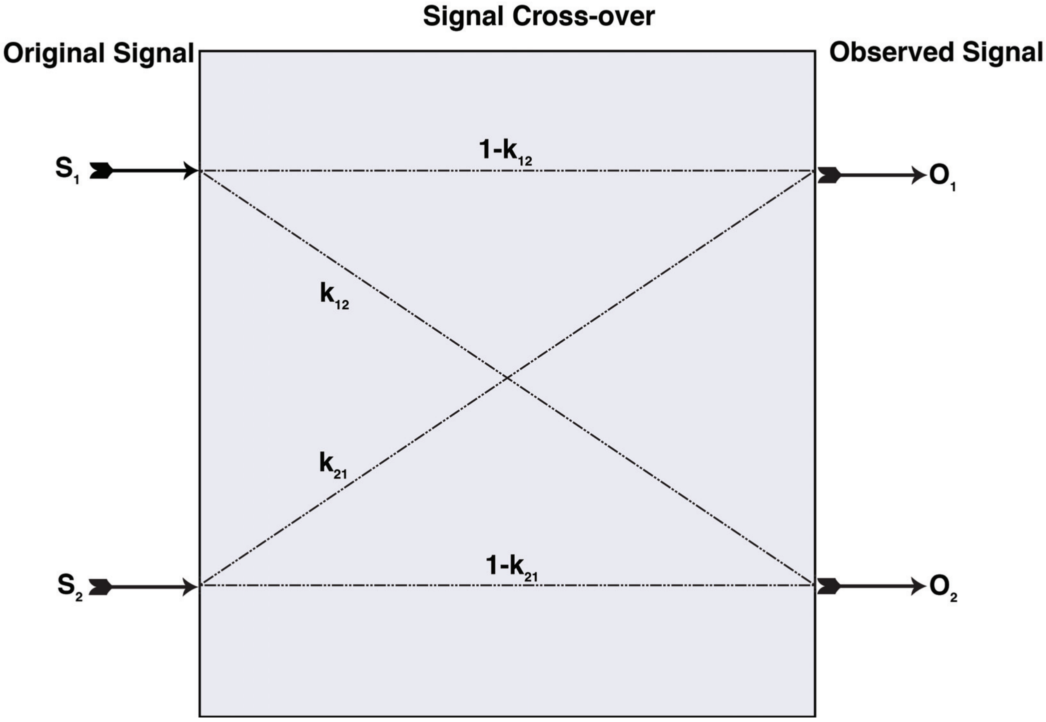

Figure 4.29. Diagram of two-signal spillover system

Adapted From: (Bagwell and Adams, 1993)

relationship between s's and o's is described by

$$o_1 = (1 - k_{12})s_1 + k_{21}s_1 \tag{4.2}$$

$$o_2 = k_{12}s_1 + (1 - k_{21})s_2 \tag{4.3}$$

where k_{12} and k_{21} are called crossover constants: k_{12} is the proportion of s_1 leaking into o_2 and k_{21} is the proportion of s_2 leaking into o_1. s_1 and s_2 are the original signals to be recovered as the compensated signals (Bagwell and Adams, 1993). To solve for s_1 and s_2 algebraically;

$$s_1 = o_1 \left(\frac{1 - k_{21}}{1 - k_{12} - k_{21}} \right) + o_2 \left(\frac{-k_{21}}{1 - k_{12} - k_{21}} \right) \tag{4.4}$$

$$s_2 = o_1 \left(\frac{-k_{12}}{1 - k_{12} - k_{21}} \right) + o_2 \left(\frac{1 - k_{12}}{1 - k_{12} - k_{21}} \right). \tag{4.5}$$

These equations can also be written in a matrix form as;

$$\begin{bmatrix} o_1 \\ o_2 \end{bmatrix} = \begin{bmatrix} 1 - k_{12} & k_{21} \\ k_{12} & 1 - k_{21} \end{bmatrix} \begin{bmatrix} s_1 \\ s_2 \end{bmatrix} \tag{4.6}$$

The crossover constants, k_{12} and k_{21}, are calculated using fluorochrome controls. In the control of fluorochrome 1, there is only fluorochrome 1 present in the experiment. Similarly, the control of fluorochrome 2 contains only fluorochrome 2. k_{12} is calculated for one event under the fluorochrome 1 control via

$$k_{12} = \frac{o_2^1}{o_1^1 + o_2^1} \tag{4.7}$$

where the superscripts represent the control of fluorochrome 1 and subscripts denote the fluorescence signals from each fluorochrome. The complete solution of k_{12} described extending the number of events to n_1 is as follows:

$$k_{12} = \frac{\Sigma^{n_1} o_2^1}{\Sigma^{n_1} o_1^1 + \Sigma^{n_1} o_2^1} \tag{4.8}$$

Again the complete solution of k_{21} with the number of events extended to n_2 under the fluorochrome 2 control is;

$$k_{21} = \frac{\Sigma^{n_2} o_1^2}{\Sigma^{n_2} o_1^2 + \Sigma^{n_2} o_2^2} \tag{4.9}$$

After determining the cross-over constant values, the fluorescence measurements can be compensated by inserting these values into Equations 4.4 and 4.5.

In our implementation, fluorochrome 1 and fluorochrome 2 represent FITC and PE, respectively. The detector D response denotes the observed signal o_1 at FITC channel while the detector C response represents the observed signal o_2 at PE channel. k_{12} is the FITC spillover constant that leaks into PE channel and k_{21} describes the PE spillover constant that leaks into FITC channel. Finally, s_1 and s_2 describe the original FITC signal and the original PE signal, respectively.

We calculated k_{12} to be equal 0.2071 and k_{21} to be equal 0.0491. The FITC spillover into PE channel is bigger than the PE spillover into FITC channel as expected. Using these values for cross-over constants, we removed the contributions from PE into the FITC channel, and from FITC into the PE channel, to obtain the original signals. The results are shown in the following figures.

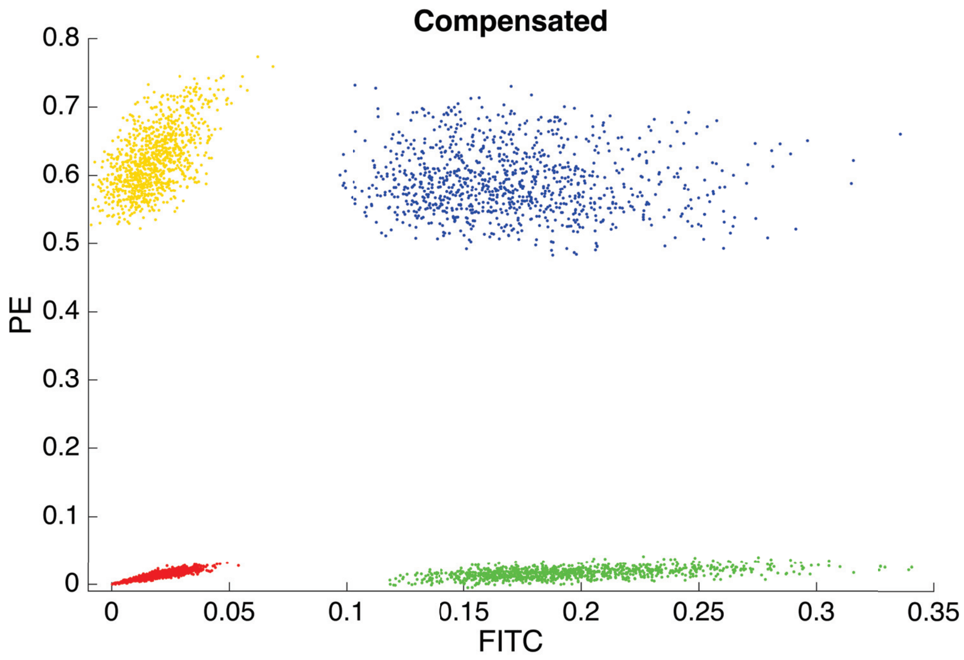

Figure 4.30. The results of the detector responses for each of 4000 cells after formulaic linear compensation in the linear scale

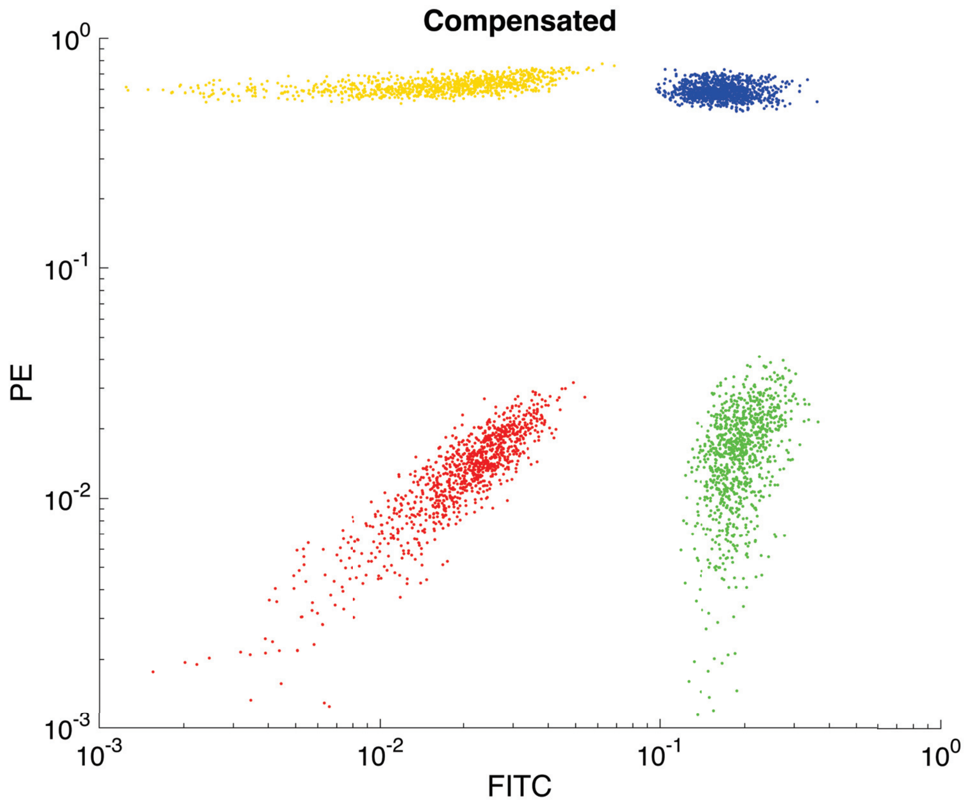

Figure 4.31. The results of the detector responses for each of 4000 cells after formulaic linear compensation in log-scale

In these figures, the compensation results can be seen better in log-scale. All results show that the compensated signals are placed more accurately in their respective quadrants than the observed signals. As expected, the log transformation causes that the - - group looks like correlated.

4.5.2. Manual Linear Compensation

We applied second two-colour linear compensation protocol to our ground-truth dataset to compensate the fluorescence intensities. In this protocol, two-colour compensation is described via the expressions

$$I_{FITC} = (FL1 - AFL2) \tag{4.10}$$

$$I_{PE} = (FL2 - BFL1) \tag{4.11}$$

where $FL1$ and $FL2$ denote FITC channel and PE channel, respectively. B describes the spillover coefficient of FITC fluorescence leaking into PE channel and A is again spillover coefficient of PE fluorescence leaking into FITC channel. In the manual approach, the values for A and B are determined by trial and error.

We started compensation by determining the A parameter because the spillover of PE into FITC channel is smaller than the spillover of FITC into PE channel. We varied A in the interval [0.001, 0.5] for + - cell group and - - cell group until the median of the detector responses of the + - cell group match the median of the detector responses of the - - cell group (Fig. 4.32). We calculated A to be equal 0.05. Next, we varied B from 0.001 to 0.5 with 0.001 increments for the - + cell group and - - cell group and determined the spillover coefficient of FITC fluorescence leaking into PE channel, providing a B of 0.281 (Fig.4.33). Inserting the values of A and B as determined above into Equations 4.10 and 4.11, respectively, we removed the FITC spillover into PE channel and the PE spillover into FITC channel.

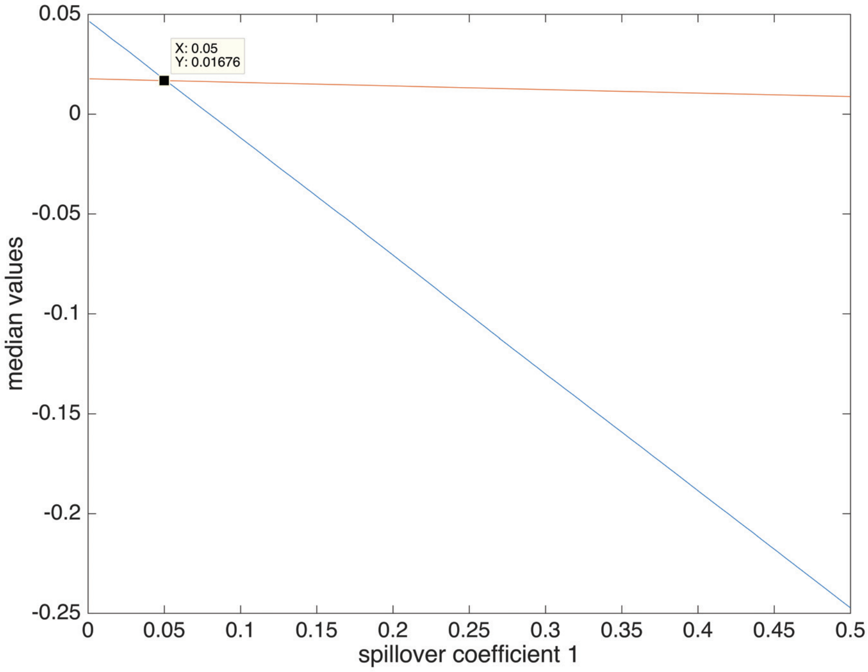

Figure 4.32. The spillover coefficient A matching the medians of the corresponding cell groups for manual linear compensation

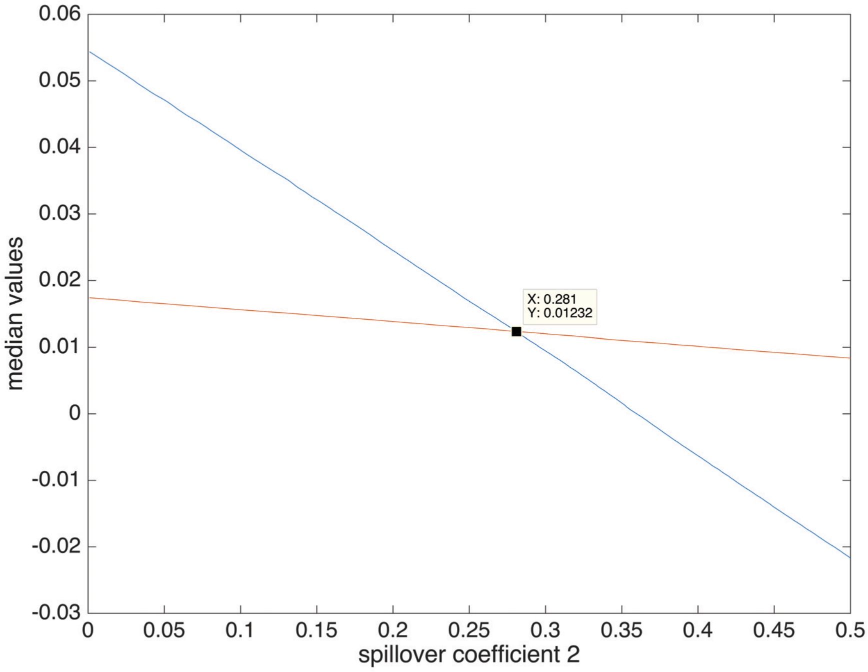

Figure 4.33. The spillover coefficient B matching the medians of the corresponding cell groups for manual linear compensation

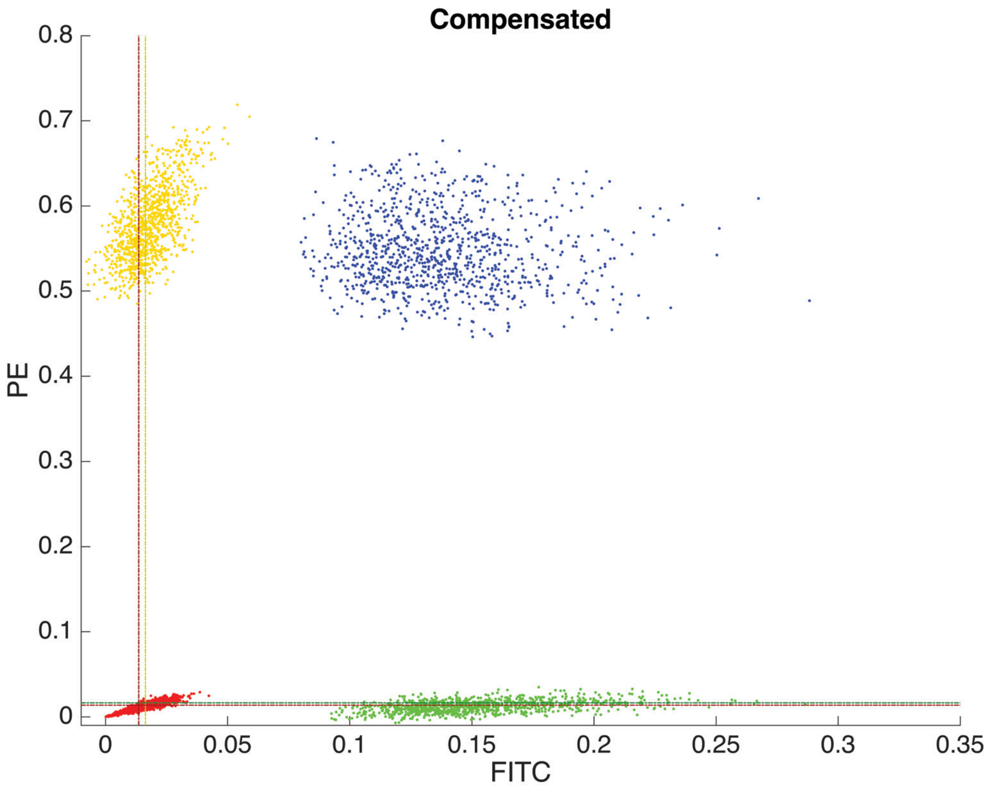

Figure 4.34. The results of the detector responses for each of 4000 cells after manual linear compensation matching the means matching the medians in the linear scale

The yellow vertical line represents the median value of compensated fluorescence intensity of - + cell group while the red vertical line represents - - cell group. The green horizontal line describes the median value of compensated fluorescence intensity of + - cell group and the red horizontal line denotes the median value of - - cell group. Notably, we aligned the median values of the fluorescence intensities of - + and - - cell group after manual compensation. Similarly, we observed the median value of the fluorescence intensity of + - cell group is in alignment with the median value of the fluorescence intensity of - - cell group. The cell groups are seen better in log-scale than linear-scale (Fig.4.35). As follows from the figures shown above, it can be seen that the median of + + cells in alignment with the median of - + cells. In same manner, the median of + - cells is in alignment with - - cells. We observed the results at the proper quadrants with a better placement than the uncompensated data.

In this part, we compared the results of two-colour linear compensation protocol to our ground-truth dataset matching the mean fluorescence intensities of the corresponding

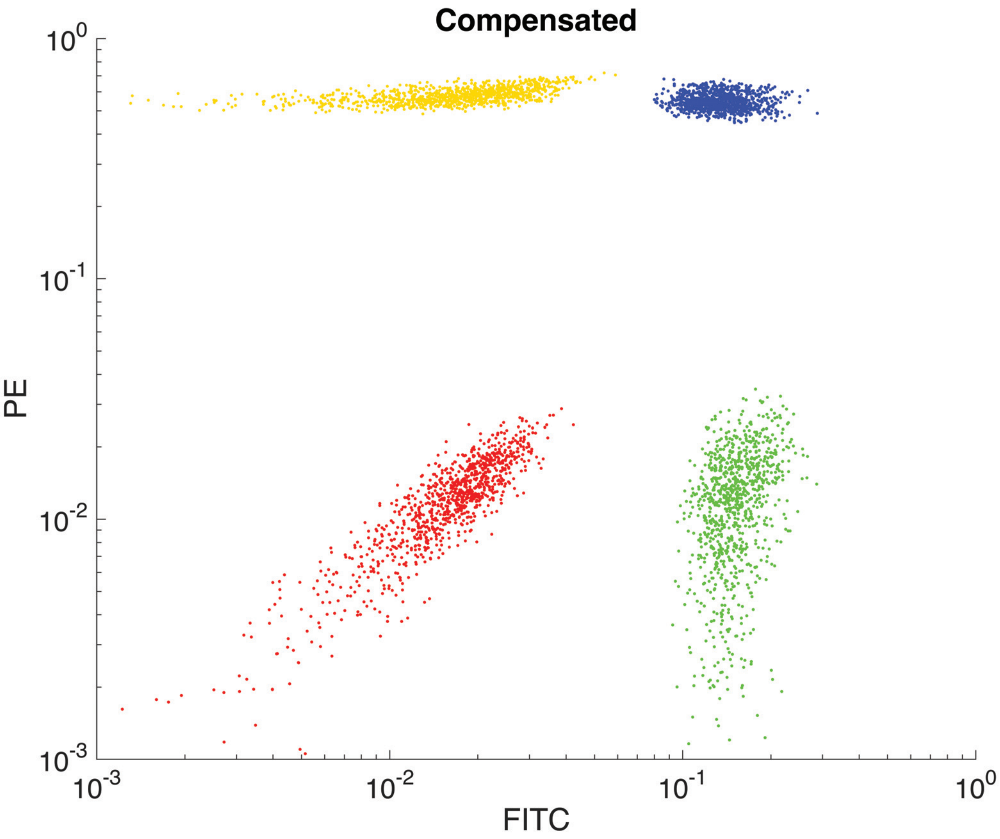

Figure 4.35. The results of the detector responses for each of 4000 cells after manual linear compensation matching the medians in log scale

cell groups. Therefore, we again applied two-colour linear compensation protocol to our ground-truth dataset to match mean fluorescence intensities. We repeated all calculations to determine spillover constants, A and B, in a same manner. We calculated the spillover constant determining firstly mean of fluorescence intensities of +- and – cell groups, and then adjusting A in same, previous interval, we determined the matching mean values of these cell groups. We calculated the spillover coefficient of PE fluorescence overflowing into FITC channel, A, equalling to 0.053 (Fig.4.36). Secondly, we determined the spillover constant, B, determining again mean of the fluorescence intensities of -+ and – cell groups. The spillover constant, B equal to 0.283 (Fig.4.37). The results of compensations are shown in Figures 4.38 and 4.39.

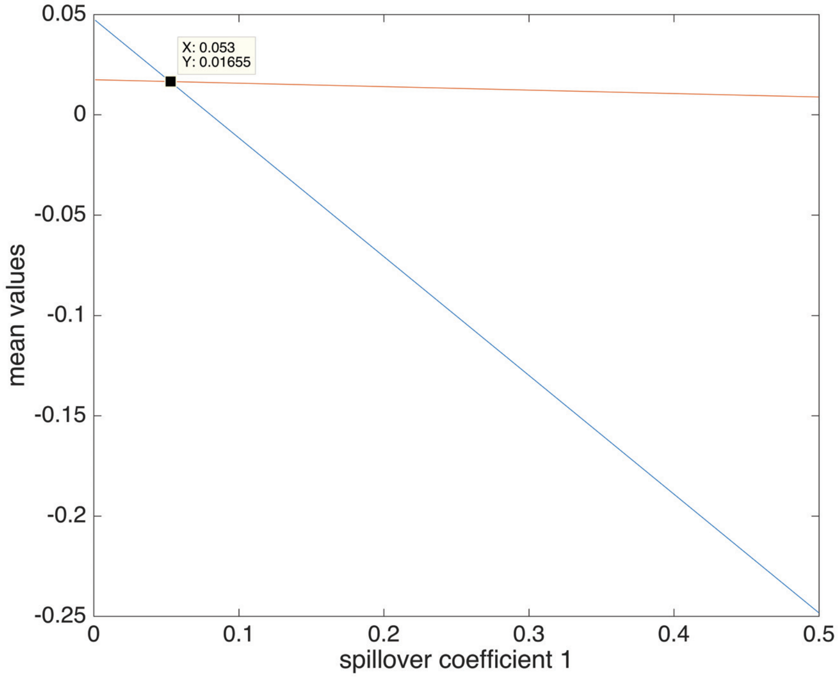

Figure 4.36. The spillover coefficient A matching the means of the corresponding cell groups for manual linear compensation

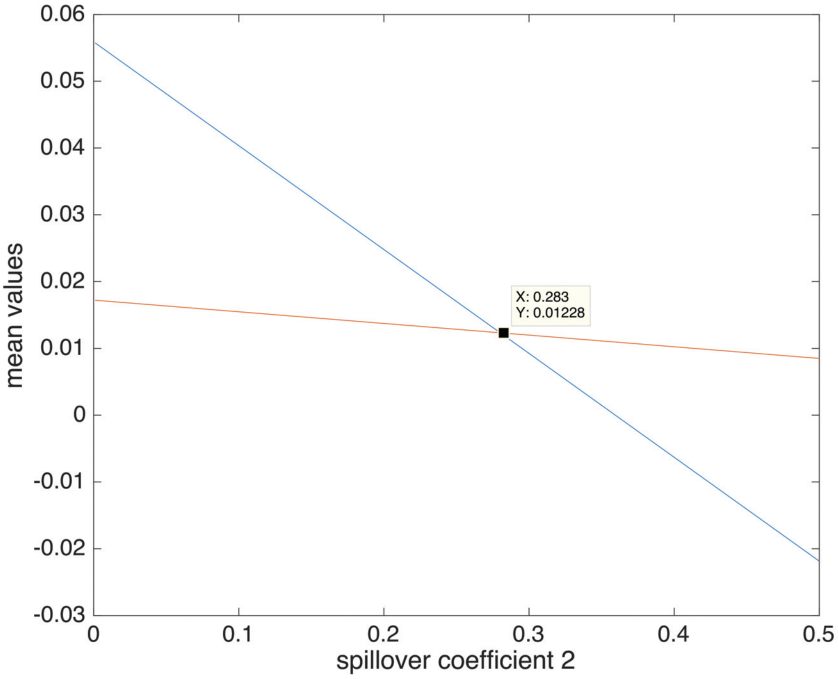

Figure 4.37. The spillover coefficient B matching the means of the corresponding cell groups for manual linear compensation

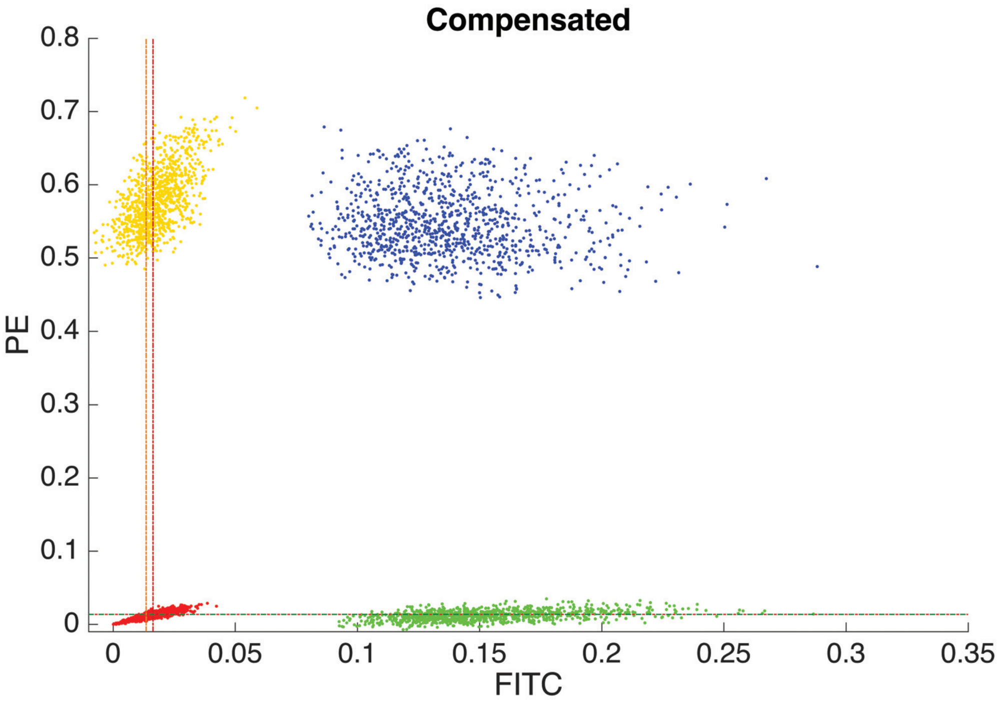

Figure 4.38. The results of the detector responses for each of 4000 cells after manual linear compensation matching the means in linear scale

The results show that we obtained the nearly identical compensation coefficients in accordance with median fluorescence intensities and mean fluorescence intensities. For this reason, the results did not vary noticeably between the compensation using the median fluorescence intensities and the mean fluorescence intensities.

4.5.3. Effects of Latent Fluorochrome Fraction

Earlier, we investigated the differences between the results of the formulaic and manual linear compensation methods applied to our ground-truth synthetic dataset. In this part, we decreased the autofluorescence intensity in three step with 0.1, 0.01, and 0.001 fluorochrome fractions of FITC fluorescence emission. We repeated all calculations to determine the detector responses as in the previous section, and then we obtained the new corresponding ground-truth datasets through the given fluorochrome fractions. Then, we applied the manual linear compensation protocol on each dataset. The results are shown, respectively, in Figures 4.40, 4.41, and 4.42.

We observed some negative values at the compensated data because of the subtrac-

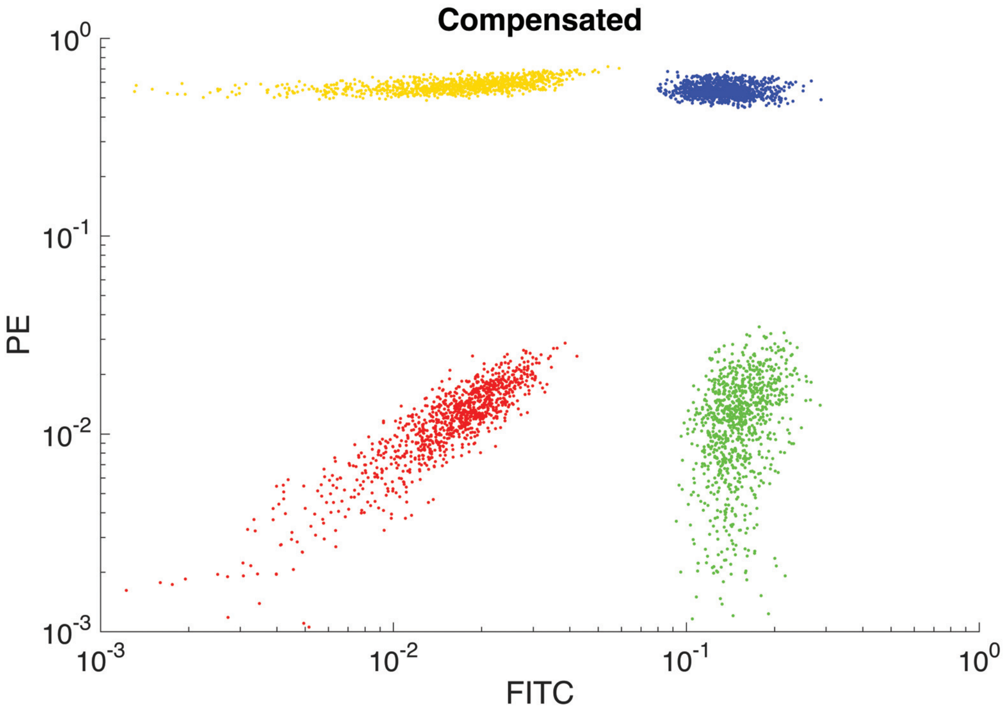

Figure 4.39. The results of the detector responses for each of 4000 cells after manual linear compensation matching the means in log scale

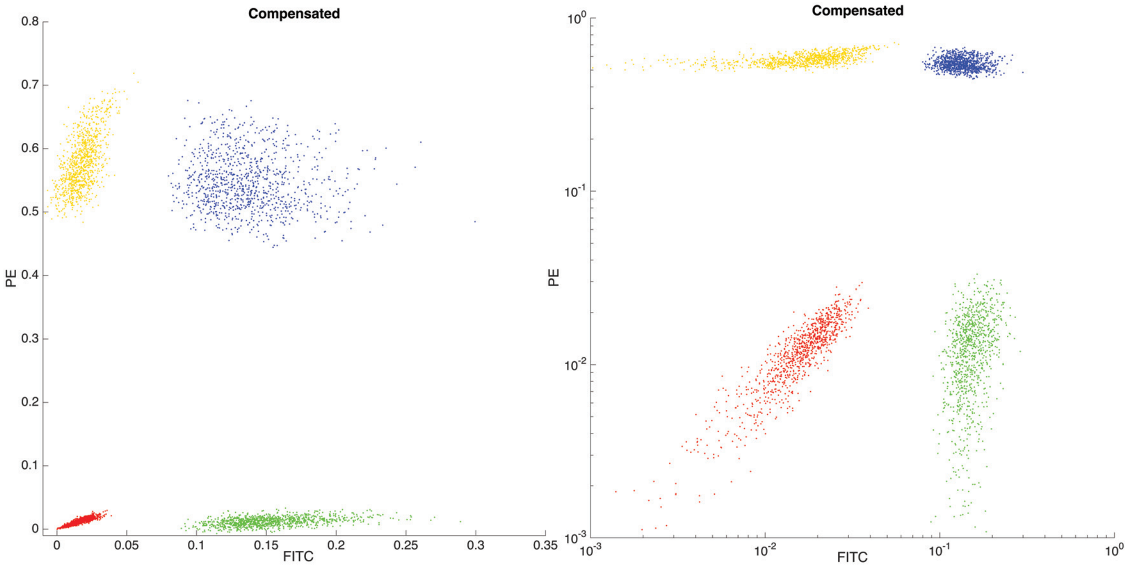

Figure 4.40. The results of compensation in linear and log scale for fluorochrome fraction equalling to 0.1 of FITC fluorescence emission

tion of fluorescence intensities at the manual linear compensation protocol. The results show that the data suffers from distortions in log scale, especially for decreased latent

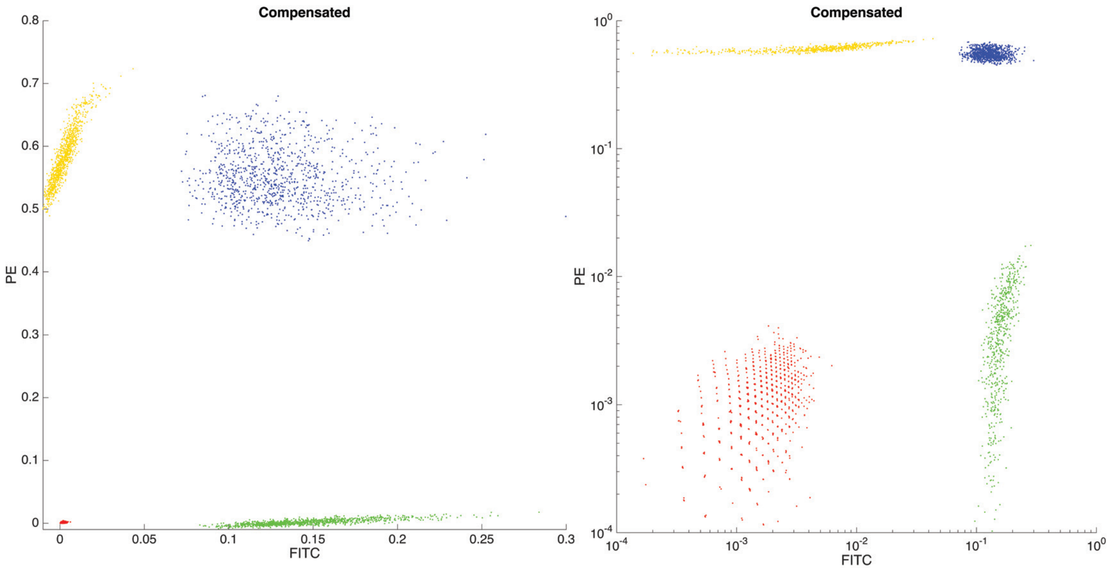

Figure 4.41. The results of compensation in linear and log scale for fluorochrome fraction equalling to 0.01 of FITC fluorescence emission

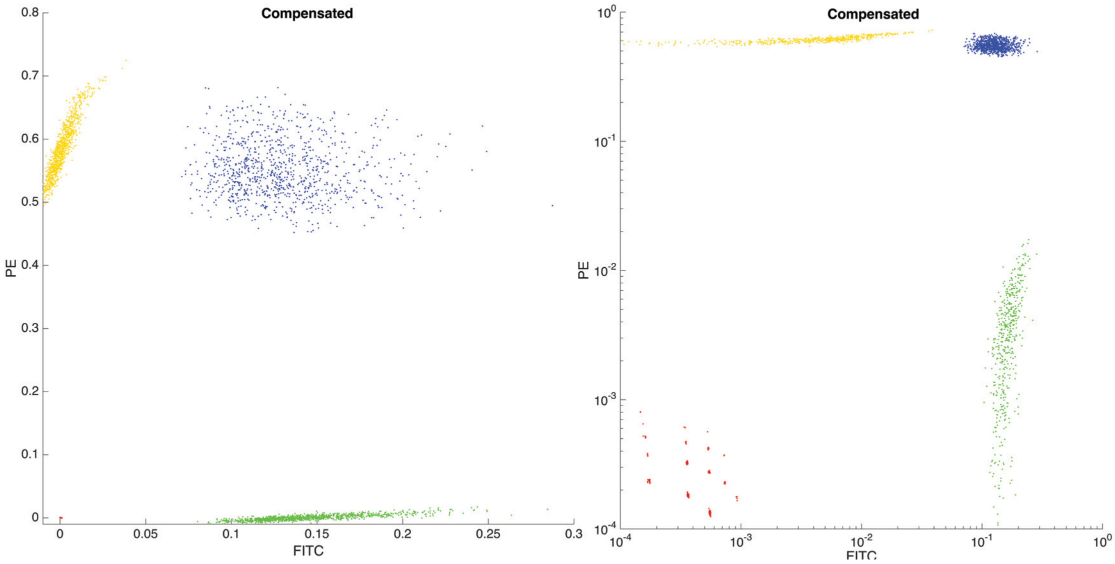

Figure 4.42. The results of compensation in linear and log scale for fluorochrome fraction equalling to 0.001 of FITC fluorescence emission

fluorochrome fluorescence emissions. We also observed a decrease in the means of the different cell groups proportionally.

CHAPTER 5

DISCUSSION

In this thesis, we developed a numeric platform simulating fluorescence intensity measurements on BD FACSCanto flow cytometer for each cell and constructed ground-truth datasets for evaluating automated compensation algorithms. We firstly modelled the cells to obtain the properties of FITC, PE, and both FITC-PE conjugated lymphocytes. The modelling of cells was carried out in terms of the number of target proteins present in the cells and their sizes. Secondly, we modelled the fluorescence emission based on fluorochrome concentration, excitation duration, fluorochrome-specific absorbance and total absorbance, and total absorbed energies, and determined the number of emitted photons from FITC, PE, and FITC and PE conjugated cells. Then, we modelled the optic channel of BD FACSCanto flow cytometer and distributed emitted photons among the different detectors in a stochastic manner. After determining photon distributions across the detectors, we obtained the photomultiplier tubes responses at the detectors, using a model of pre-amplifier circuit, in terms of the voltage output from the detectors.

In our effort to develop the numerical flow cytometer model, we made certain assumptions. These assumptions are discussed in the following paragraphs.

We started with constructing quantitative cell data in Chapter 3 with the aim of characterizing biomarker concentrations present in the cells. The biomarker concentration is related to the volume of each cell, the number of the target proteins in each cell, and the ratio of target protein-bound fluorochromes. To evaluate the volume of cells, we assumed that the model cells based on lymphocytes are spherical cells. In actuality, the lymphocytes have ellipsoidal shapes as they pass through the interrogation point, because the hydrodynamic focusing deforms the shapes of cells into an ellipsoid and cell flow reorientates the cells along the larger axis. An ellipsoid-shaped cell model could easily be incorporated into our simulation instead of a spherical one, except that quantitative measures on the extent of the deformation are lacking in the literature. Furthermore, there is no reason to expect that such a mismatch in shape would cause any significant difference in the ensuing fluorescence emissions.

We also assumed that the biomarker concentration exactly equals the concentration of target protein distributed uniformly within the cell volume. Actually, the target proteins can be in the membrane, cytoplasm, and on the nucleus of the cells. In addition, we could not find any information on the number of typical target proteins in lymphocytes. As an alternative, we used the statistics of U2OS cells (Milo, 2013) to characterize target protein distributions. Therefore, we constructed a specific number of lognormally distributed target proteins located within a 0.95 confidence interval according to these statistics. These assumptions could cause some potential correlations in fluorochrome-conjugated protein distributions. This could affect the measured fluorescence intensities as joint distributions at different detectors. In further analysis of the flow data, the joint distributions are required to detect and then be removed from the measurement channels with a proper compensation method for true interpreting of the data. The biomarker concentration will be calculated again more accurately in the case of inserting the actual number of target proteins in our cell model.

Fluorescent staining of target proteins can be achieved by conjugating fluorochromes to their specific targets. It is critical to know the number of fluorochromes bound to target proteins because this affects the intensity of fluorescence emissions. However, this number depends on many factors including the details of sample preparation. We do not know how the target proteins are distributed in the cells. Additionally, the number of some proteins can be greater than or less than the average number of a desired statistical protein distribution of the target protein in the cell[1]. The sample preparation process can be stochastically modelled to determine the amount of protein-dye conjugation ratio, the numbers of non-specific antibody binding and unlabelled protein. Such a model, however, would require the details of experimental conditions such as temperature, waiting time and so on. Furthermore, modelling the sample preparation process is not the focus of our study. In order to determine the fluorochrome concentrations, we therefore assumed that the specific target protein/fluorochrome pairs are distributed uniformly in the cells and all fluorochromes are individually conjugated to all their target proteins.

Note that, we disregarded the effects of non-specific antibody binding and constructed the fluorescence emission profiles of cells. Flow cytometry experiments are run with the aim of best discrimination between positive and negative cells. Non-specific binding, in fact, can occur in both negative and positive cells (Hulspas, 2010) and disrupt the expected fluorescence emissions. Fluorescence emissions are also affected by the background signal level of autofluorescence. In our model, we assumed that autofluorescence intensity is distributed uniformly across the spectrum of observed wavelengths, as we have no information about the emission spectra of the endogenous substances con-

---

[1] Available on:https://tools.thermofisher.com/content/sfs/brochures/TR0031-Calc-FP-ratios.pdf

tributing to autofluorescence in lymphocytes.

In our implementation, we used only the blue laser as the excitation light source. We can use additional light sources in modelling of fluorescence emission. With additional light sources in the optical system of the flow cytometer, the power that falls per measurement point at the cross-section of the cell would vary, along with the amount of total absorbed energy. For a different choice of flow cytometer, these can be calculated again in terms of the corresponding lasers present in the excitation optics system.

In our model of the optical system, the achromatic focusing lens forms the shape of the laser beam into an ellipsoid with 9μm height and 65μm width to provide uniform spatial profiles or more equal illumination at the interrogation point. In addition, this elliptical shape has a known Gaussian energy profile[1]. Because the laser beam has Gaussian output, the center of the laser beam is most intense and the intensity decreases towards edges of the beam. However, we assumed that the blue laser illuminates each point in the cell cross-section uniformly. While we can update the power calculation for a Gaussian beam profile, there is no reason to expect that it would alter the resulting photon emissions in a significant manner, since the fluorochromes are assumed to be distributed uniformly as well.

We also disregarded the photo-bleaching effects on the fluorescence intensities. Each fluorochrome can accept a certain number of photons from a light source in each excitation-emission cycle (van den Engh and Farmer, 1992). If the number of photons absorbed from the light source is bigger than the accepted number of photons of the fluorochrome, photon saturation can be observed in the fluorochrome which also disregarded. Therefore, photo-bleaching occurs when there is a high intensity laser and a high speed of cell flow in the flow cytometry experiment. Since laser exposure time is small in our calculations, it would not significantly affect the measured fluorescence intensities at the detectors, allowing us to disregarded such affects.

In modelling fluorescence emission, we assumed that a fixed fraction of the emitted photons was entering the optic channel due to interrogation cell geometry. However, we could not obtain the specifications of all components in the optic channel for an exact calculation of this fraction. As a result, we assumed that ten percent of the emitted photons entered the optical channel. The real ratio can potentially be smaller or larger than our assumed value. If it is smaller, it would cause less fluorescence intensities at the detectors. Similarly, if it is larger, it would cause more fluorescence intensities. The

---

[1] Available on:https://expertcytometry.com/what-is-a-flow-cytometry-laser-how-flow-cytomtery-optics-function/

number of photons falling at the photomultiplier tubes would also vary depending on this ratio. Yet, these effects can be alleviated by adjusting the gain of the electron-multiplier of the photomultiplier tubes. Moreover, the actual fraction of received photons at the optical channel can be inserted to our simulation when this constant is provided by another experiment or producing company of the flow cytometer. Note that, we also ignored dark current effects on the photomultiplier tubes, though it can affect the output current of each PMT, assuming it to be negligible.

To determine the photon distributions across detectors, we assumed that the all photons from each fluorochrome as well as both multi-fluorochromes are independent events. We have any knowledge about the photon-electron interactions in fluorochrome molecules during the fluorescence process. These interactions are the topic of the quantum electrodynamics and they are outside of the scope of our study. We assumed that the average behaviour of photons does not vary the photon distributions at the different detectors in actuality because the number of photons falling on detectors are large.

Finally, we used a model pre-amplifier circuit from the literature to calculate the voltage output of each detector at the octagon detector array. However, we could not obtain the specifications of the actual pre-amplifier circuit installed in BD FACSCanto flow cytometer. However, the circuit elements can be adjusted or changed to match a different choice of flow cytometer electronics system, and the voltage output would vary depending on these modifications.

CHAPTER 6

CONCLUSION

This thesis presents a numerical platform to simulate flow cytometry readings from FITC, PE and both FITC and PE conjugated model cells in order to provide reference datasets to evaluate automated compensation algorithms in multicolor flow cytometry. We constructed different model cell profiles to represent lymphocytes stained with FITC, PE or both FITC and PE for their target proteins and cell sizes. Using these cell profiles and the specifications of excitation light source and parameters of the fluidics system of BD FACSCanto flow cytometer, we modelled the fluorescence emission process to provide the number of photons emitted from each fluorochrome-conjugated proteins. We modelled the collection optic system of BD FACSCanto flow cytometer, and implemented a stochastic photon counting process to obtain the fluorescence intensities at different detectors in the collection optic system. Then, we simulated a model pre-amplifier circuit to determine the voltage readings of each detector. Finally, we obtained the realistic flow cytometry datasets using all these models, and applied to two different linear compensation methods.

For future work, different cytometers can be simulated by modifying the optical parameters and cell profiles. Our numerical platform can be used to design new flow cytometer models with more lasers and/or more detectors. In addition, new optical systems of flow cytometers with alternative filters can be developed to tune detector responses as desired. The automated compensation algorithms can be developed for more accurate interpretation of flow data in multicolor flow cytometry experiments.

REFERENCES

Bagwell, C. B. and E. G. Adams (1993). Fluorescence spectral overlap compensation for any number of flow cytometry parameters. *Annals of the New York Academy of Sciences 677*(1), 167–184.

BD FACSCanto, B. (2006). *BD FACSCanto Flow Cytometer Reference Manual*.

Case, T. W. (1920). Thalofide cell a new photo-electric substance. *Physical Review 15*(4), 289.

Chattopadhyay, P. K., T. M. Gierahn, M. Roederer, and J. C. Love (2014). Single-cell technologies for monitoring immune systems. *Nature immunology 15*(2), 128–135.

Coons, A. H., H. J. Creech, and R. N. Jones (1941). Immunological properties of an antibody containing a fluorescent group. *Proceedings of the Society for Experimental Biology and Medicine 47*(2), 200–202.

Coulter, W. (1953). Means for counting particles suspended in a fluid. us patent, 2656508. *United States Patent Office. Patentiert am 20*, 1953.

Coulter, W. H. (1956). High speed automatic blood cell counter and cell size analyzer. In *Proc Natl Electron Conf*, Volume 12, pp. 1034–1040.

Crosland-Taylor, P. (1953). A device for counting small particles suspended in a fluid through a tube. *Nature 171*(4340), 37–38.

Dittrich, W. and W. Göhde (1969). Notizen: Impulsfluorometrie bei einzelzellen in suspensionen. *Zeitschrift für Naturforschung B 24*(3), 360–361.

Einstein, A. (1917). On the quantum mechanics of radiation. *Physical Journal 18*, 121–128.

Einstein, A. and T. into English (1965). Concerning an heuristic point of view toward the emission and transformation of light. *American Journal of Physics 33*(5), 367.

Evanko, D., A. Heinrichs, and C. Rosenthal (2011). Milestones in light microscopy. *Nature*.

Fulwyler, M. J. (1965). Electronic separation of biological cells by volume. *Science 150*(3698), 910–911.

Givan, A. L. (2013). *Flow cytometry: first principles*. John Wiley & Sons.

Gucker Jr, F. T., C. T. O'Konski, H. B. Pickard, and J. N. Pitts Jr (1947). A photoelectronic counter for colloidal particles1. *Journal of the American Chemical Society 69*(10), 2422–2431.

Hamamatsu, P. (2006a). Photomultiplier tubes: Basics and applications. *Edition 3a*.

Hamamatsu, P. (2006b, 6). Photomultiplier tubes r928, r955. (TPMS1001E07).

Henriquez, R. R., T. Ito, L. Sun, and R. M. Crooks (2004). The resurgence of coulter counting for analyzing nanoscale objects. *Analyst 129*(6), 478–482.

Hulspas, R. (2010). Titration of fluorochrome-conjugated antibodies for labeling cell surface markers on live cells. *Current protocols in cytometry*, 6–29.

Jabłoński, A. (1935). Über den mechanismus der photolumineszenz von farbstoffphosphoren. *Zeitschrift für Physik 94*(1-2), 38–46.

Kamentsky, L. A., H. Derman, and M. R. Melamed (1963). Ultraviolet absorption in epidermoid cancer cells. *Science 142*(3599), 1580–1583.

Kamentsky, L. A., M. R. Melamed, and H. Derman (1965). Spectrophotometer: new instrument for ultrarapid cell analysis. *Science 150*(3696), 630–631.

Kuse, R., S. Schuster, H. Schübbe, S. Dix, and K. Hausmann (1985). Blood lymphocyte volumes and diameters in patients with chronic lymphocytic leukemia and normal controls. *Blut 50*(4), 243–248.

Loken, M. R., D. R. Parks, and L. A. Herzenberg (1977). Two-color immunofluorescence using a fluorescence-activated cell sorter. *Journal of Histochemistry &*

Cytochemistry 25(7), 899–907.

Macey, M. G. (2007). *Flow Cytometry*. Springer.

Maiman, T. H. (1960). Stimulated optical radiation in ruby.

Milo, R. (2013). What is the total number of protein molecules per cell volume? a call to rethink some published values. *Bioessays 35*(12), 1050–1055.

Moldavan, A. (1934). Photo-electric technique for the counting of microscopical cells. *Science 80*, 188–189.

Mullaney, P., M. Van Dilla, J. Coulter, and P. Dean (1969). Cell sizing: a light scattering photometer for rapid volume determination. *Review of Scientific Instruments 40*(8), 1029–1032.

Peeters, J., G. Dubelaar, J. Ringelberg, and J. Visser (1989). Optical plankton analyser: A flow cytometer for plankton analysis, i: Design considerations. *Cytometry Part A 10*(5), 522–528.

Production, M. A. (1999). A report of the committee on methods of producing monoclonal antibodies institute for laboratory animal research, national research council.

Provan, D. (2005). *Oxford handbook of clinical and laboratory investigation*. Oxford University Press, USA.

Reynolds, O. (1883). An experimental investigation of the circumstances which determine whether the motion of water shall be direct or sinuous, and of the law of resistance in parallel channels. *Proceedings of the royal society of London 35*(224-226), 84–99.

Roederer, M. (2001). Spectral compensation for flow cytometry: visualization artifacts, limitations, and caveats. *Cytometry 45*(3), 194–205.

Rosenthal, C. et al. (2009). Nature milestones in light microscopy. *Nat. Cell Biol 11*, 1165.

Sack, U., A. Tárnok, and G. Rothe (2009). *Cellular diagnostics: basic principles, methods and clinical applications of flow cytometry*. Karger Medical and Scientific Publishers.

Scherer, J. M., W. Stillwell, and L. J. Jenski (1999). Anomalous changes in forward scatter of lymphocytes with loosely packed membranes. *Cytometry 37*(3), 184–190.

Schmid, I. (2012). *Flow Cytometry-Recent Perspective*. InTech,.

Shapiro, H. M. (2005). *Practical flow cytometry*. John Wiley & Sons.

Sklar, L. A. (2005). *Flow cytometry for biotechnology*. Oxford University Press.

Stokes, G. G. (1852). On the change of refrangibility of light. *Philosophical Transactions of the Royal Society of London 142*, 463–562.

Tuchin, V. V. (2011). *Advanced optical flow cytometry: methods and disease diagnoses*. John Wiley & Sons.

van den Engh, G. and C. Farmer (1992). Photo-bleaching and photon saturation in flow cytometry. *Cytometry Part A 13*(7), 669–677.

Van Dilla, M. A., T. Truiullo, P. F. Mullaney, and J. Coultex (1969). Cell microfluorometry: a method for rapid fluorescence measurement. *Science 163*(3872), 1213–1214.

Verschoor, C. P., A. Lelic, J. L. Bramson, and D. M. Bowdish (2015). An introduction to automated flow cytometry gating tools and their implementation. *Frontiers in immunology 6*, 380.

APPENDIX A

SPECIFICATIONS OF FILTERS IN THE OPTICAL CHANNEL

In this part, we presented specifications of bandpass and longpass filters at the optical systems of BD FACSCanto Flow Cytometer. We shared only open source data.

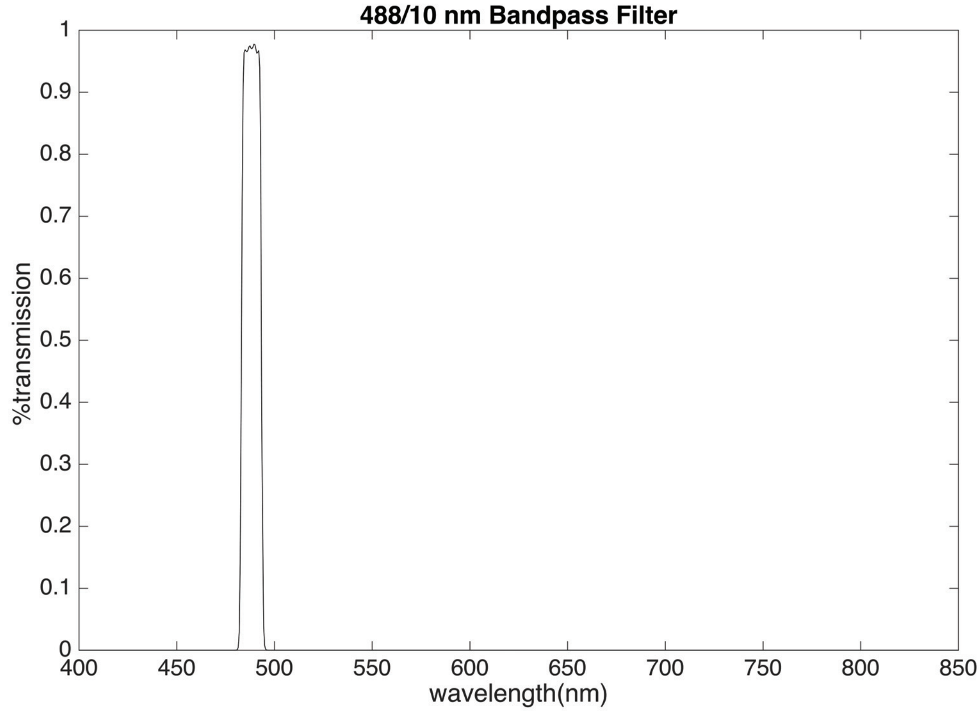

Figure A.1. BP 488/10 nm

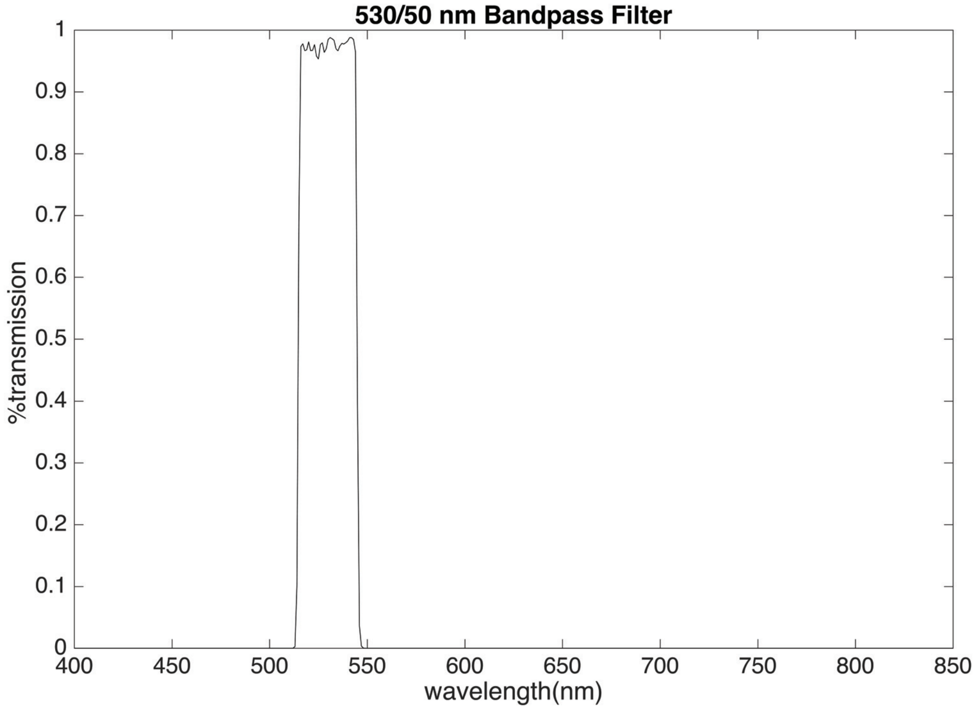

Figure A.2. BP 530/10 nm

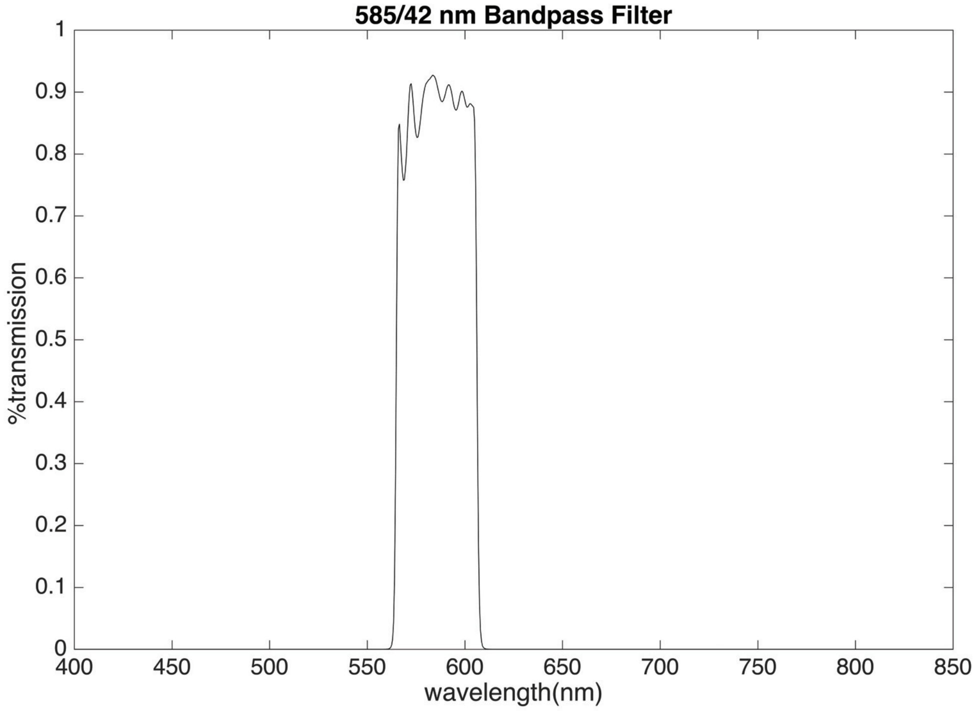

Figure A.3. BP 585/42 nm

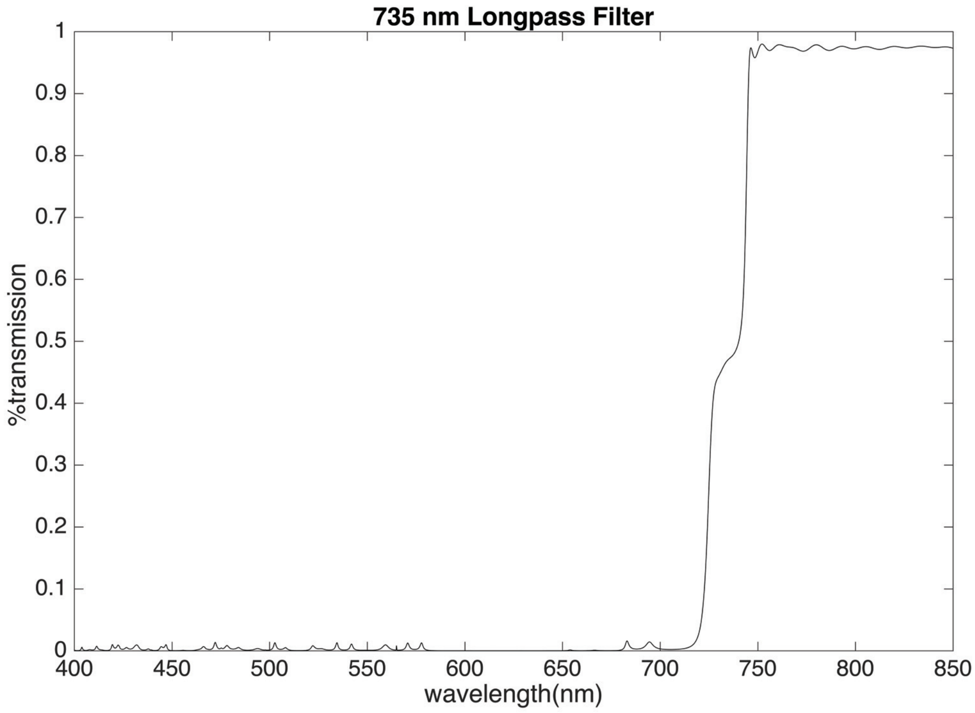

Figure A.4. LP 735 nm

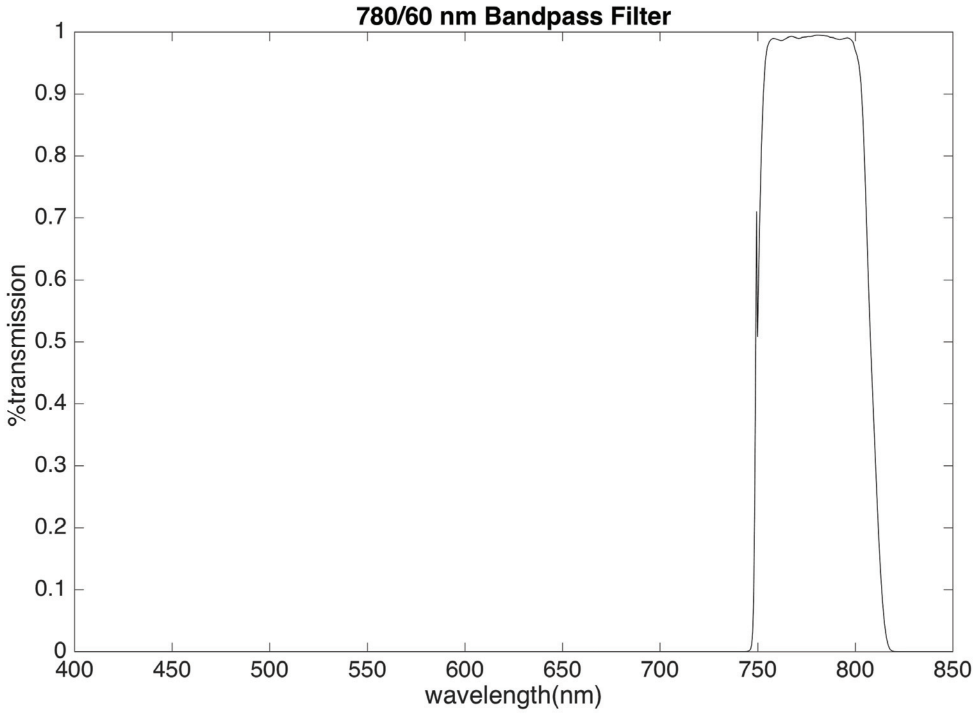

Figure A.5. BP 780/60 nm

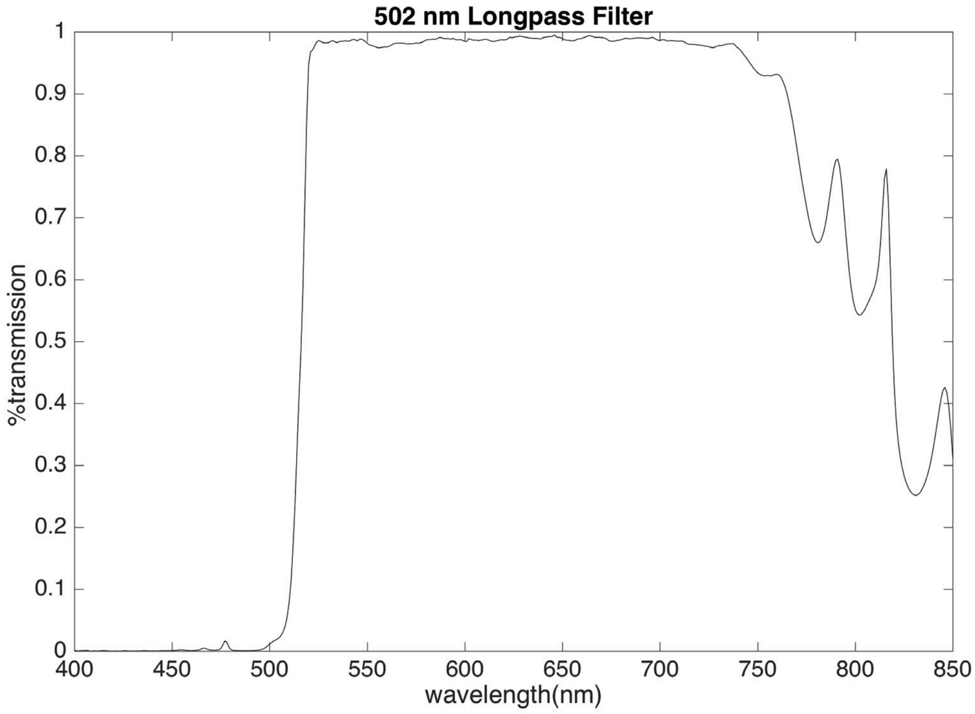

Figure A.6. LP 502 nm

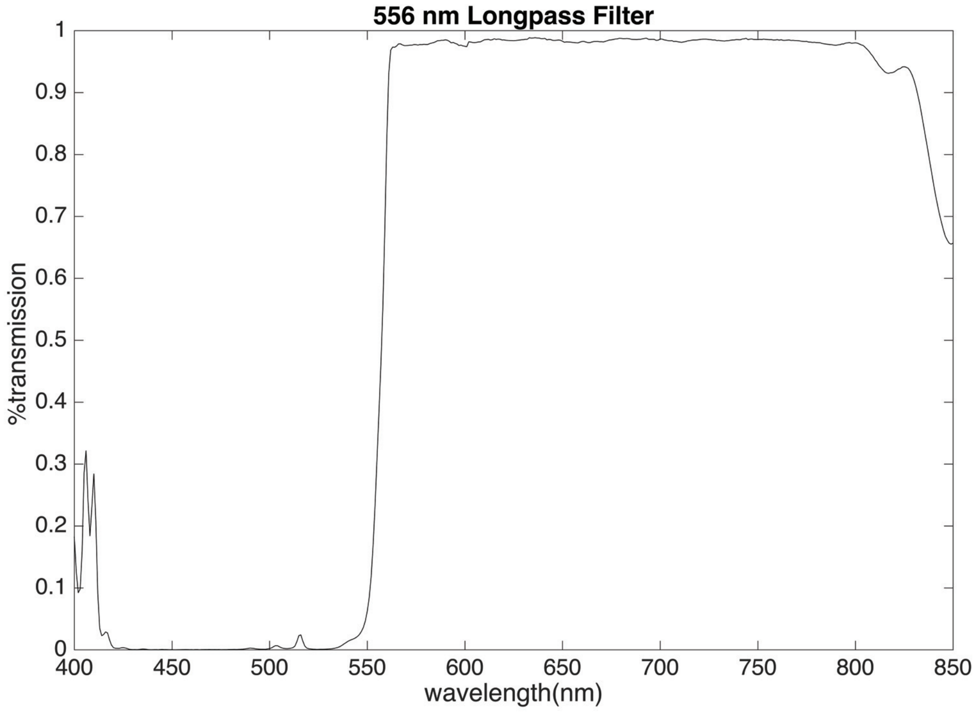

Figure A.7. LP 556 nm

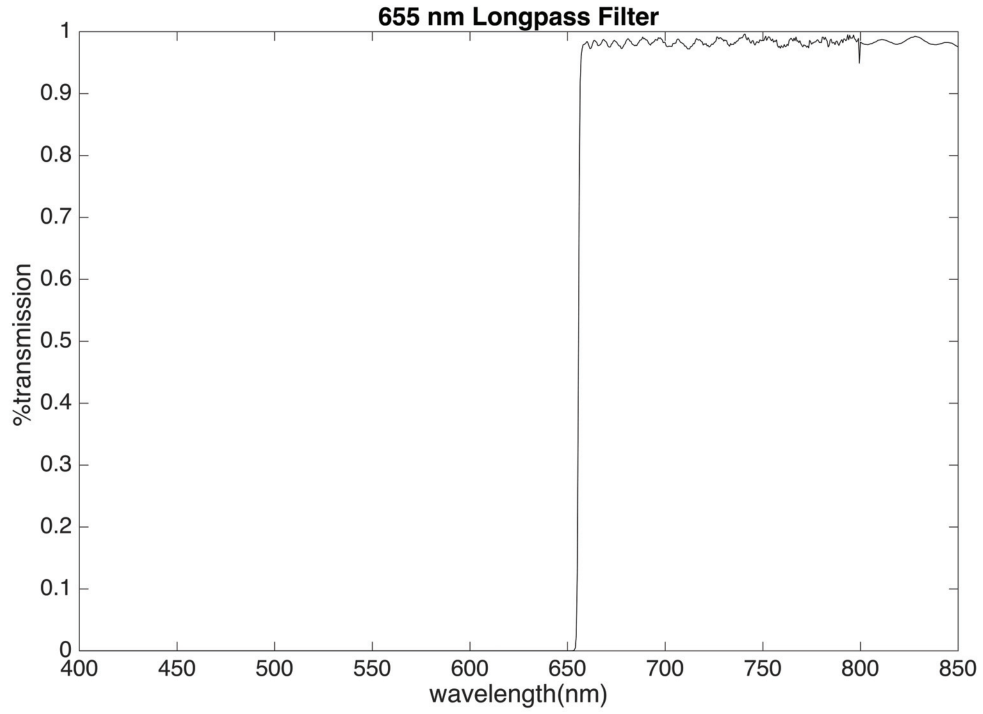

Figure A.8. LP 655 nm

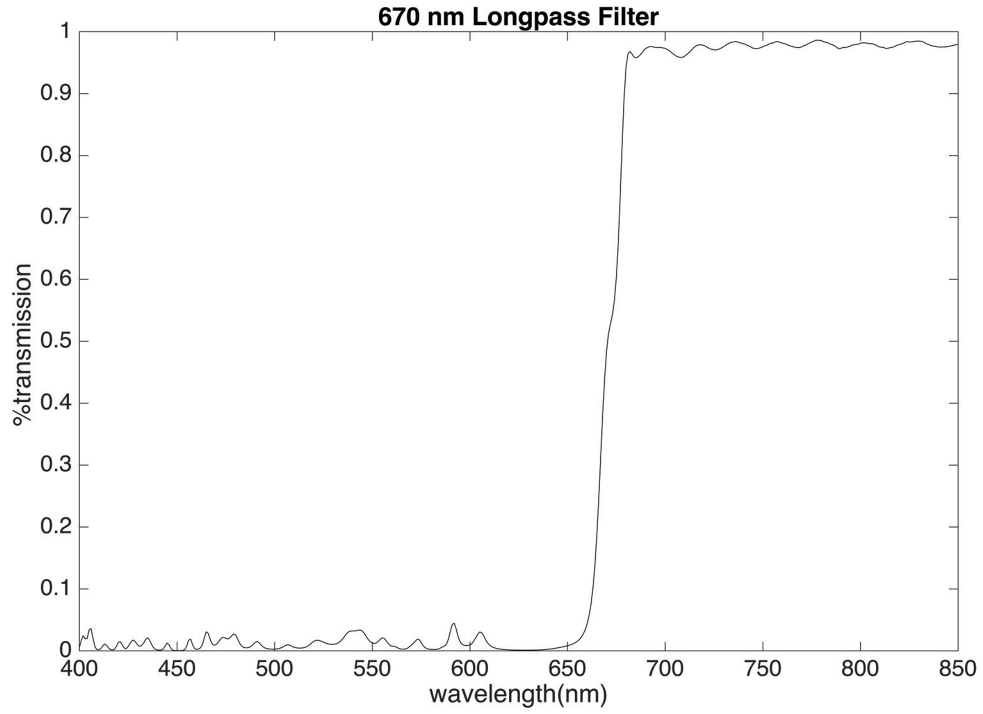

Figure A.9. LP 670 nm

APPENDIX B

SPECIFICATIONS OF PHOTOMULTIPLIER TUBES IN THE OPTICAL CHANNEL

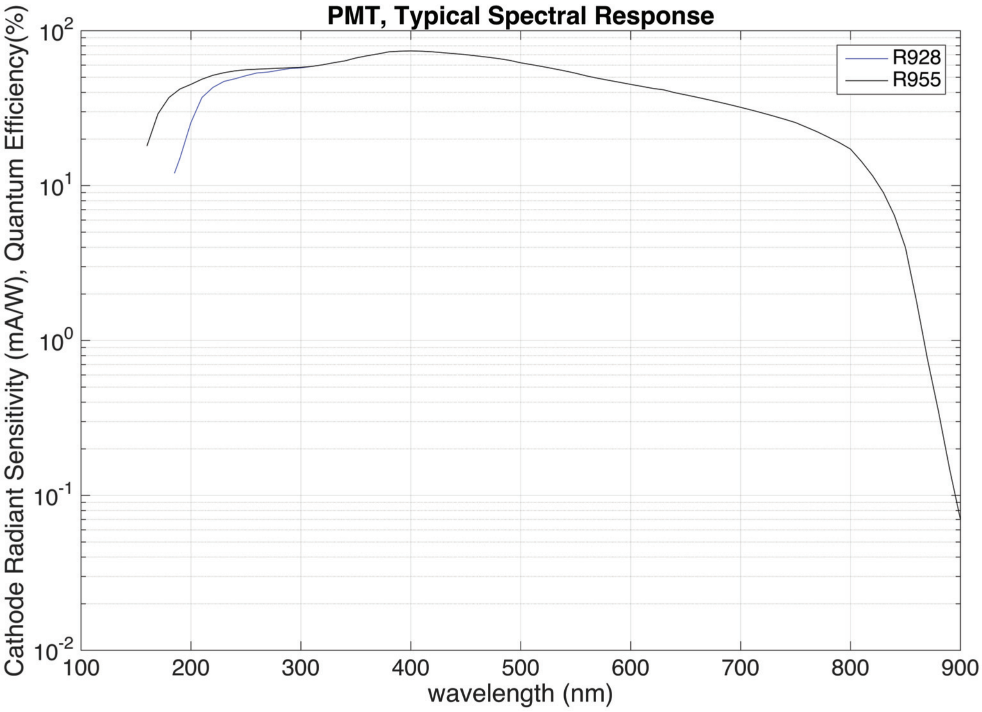

Figure B.1. R928, R955